Dissertation
submitted to the
Combined Faculties for the Natural Sciences and for Mathematics
of the Ruperto-Carola University of Heidelberg, Germany
for the degree of
Doctor of Natural Sciences

Put forward by

Diplom-Physicist:	Tobias Junginger
Born in:	Tübingen, Germany

Oral examination: 25.07.2012

Investigations of the surface resistance of superconducting materials

Referees:	**Prof. Dr.**	**Klaus Blaum**
	Prof. Dr.	**Carsten P. Welsch**

Zusammenfassung

In vielen Teilchenbeschleunigern werden supraleitende Hohlraumresonatoren verwendet, um hohe Beschleunigungsgradienten bei niedrigem Enegieverbrauch zu erzielen. Die Energieaufnahme eines Hohlraumresonators ist proportional zu seinem Oberflächenwiderstand R_S, welcher von den äusseren Parametern: Frequenz, Temperatur, magnetischem und elektrischem Feld abhängt. Insbesondere existiert kein allgemein akzeptiertes Model, welches die Erhöhung von R_S mit der Feldstärke beschreibt.

Im Rahmen dieser Arbeit wurde der 400 MHz Quadrupole Resonator für Oberflächenwiderstands und kritische HF-Feldmesssungen bei 800 und 1200 MHz erweitert, was ihn zu einer weltweit einzigartigen Messapparatur für supraleitende Materialien macht.

Verschiedene Proben wurden untersucht und dabei zeigte sich, dass R_S im Falle starker Oxidation hauptsächlich durch das elektrische HF-Feld verursacht wird. Dies kann durch Austausch von Elektronen zwischen dem Supraleiter und lokalisierten Zuständen in angrenzenden Oxiden erklärt werden. Falls die Oberfläche jedoch gut präpariert ist, wird R_S hauptsächlich durch das HF-Magnetfeld verursacht und faktorisiert in temperatur- und feldabhängige Anteile.

Mithilfe von Ultraschall-Kraftmikroskopie und Röntgenphotoelektronenspektroskopie konnten die unterschiedlichen Verlustmechanismen mit der Topographie und der Verteilung der Oxide auf den Oberflächen in Zusammenhang gebracht werden.

Abstract

In particle accelerators superconducting RF cavities are widely used to achieve high accelerating gradients and low losses. Power consumption is proportional to the surface resistance R_S which depends on a number of external parameters, including frequency, temperature, magnetic and electric field. Presently, there is no widely accepted model describing the increase of Rs with applied field.

In the frame of this project the 400 MHz Quadrupole Resonator has been extended to 800 and 1200 MHz to study surface resistance and intrinsic critical RF magnetic field of superconducting samples over a wide parameter range, establishing it as a world-wide unique test facility for superconducting materials.

Different samples were studied and it was shown that R_S is mainly caused by the RF electric field in the case of strongly oxidized surfaces. This can be explained by interface tunnel exchange of electrons between the superconductor and localized states in adjacent oxides. For well prepared surfaces, however, the majority of the dissipation is caused by the magnetic field and R_S factorizes into field and temperature dependent parts.

These different loss mechanisms were correlated to surface topography of the samples and distribution of oxides by using ultrasonic force microscopy and X-ray photon spectroscopy.

TO MY PARENTS

Acknowledgements

I would like to thank my supervisors Wolfgang Weingarten and Carsten Welsch (in alphabetical order) for giving me the opportunity to carry out this thesis and the excellent supervision during the whole time. I am indebted to Klaus Blaum for agreeing to be referee for this thesis and for the interest he showed in the subject. During the whole time I had the full support of the SRF team of the BE-RF group at CERN. In particular I want to express my gratitude to Nikolai Schwerg, who helped me with his RF engineering skills to perform the 3dB bandwidth measurements, for carefully reading this thesis and all the suggestions and discussions during the last years. Olivier Brunner in charge of the superconducting cavity activities always ensured that it was possible to perform tests with the Quadrupole Resonator and even though there were other conflicting projects, all in need of manpower and helium, he always tried to find a solution, which made everybody happy. The person in charge of the RF test area was Pierre Maesen, who was always helpful. Thanks to the operators of the CERN cryogenics groups, who always gave their best to cool down the Quadrupole Resonator. I like to thank Gabriel Pechaud, Max Gourragne and Janic Chambrillion for the excellent help they provided in mounting and preparing the resonator and the samples. Thanks for the electrical works done by David Glenat and Luca Arnaudon. My gratitude goes to Wolfgang Höfle and Daniel Valuch for modifying the PLL for use at multiple frequencies. I always had the feeling that the work was supported in the RF group led by Edmond Ciapala and later by Erk Jensen. Edmond Ciapala I also like to thank for carefully reading this thesis. Ernst Haebel did a great job designing the Quadrupole Resonator and even though he was already retired when I started this thesis, he made several times the effort to visit CERN to explain how the Quadrupole Resonator works. Information about the previous work on the Quadrupole Resonator was also given by Edgar Mahner and Didier Caligary. I like to thank Serge Forel for the chemical preparation of the bulk niobium sample. Sergio Calatroni did the sputter deposition of the niobium film sample and provided me the relevant information about the process. When we had the problem of a burnt connector Fritz Caspers immediately came to the lab to show me how to find this position inside the cryostat using a network analyzer in the time domain. I like to thank Rebecca Seviour and Oleg Kolosov for the possibility to carry out the surface analytic measurements at Lancaster University. It was a fruitful and pleasant time in England. Ilya Grishin made a big effort performing the ultrasonic

force microscopy measurements. The SEM measurements were done by Ignacio Aviles Santillana, while XPS was carried out by Paul Unsworth. Helen Cammack and Phillip Foster showed me how to use AFM and white light interferometry. Thank you for this. Mathieu Therasse and Irene Mondino did the measurement of the HIE-Isolde Quarter wave cavity and provided me the data. For the analyses Alessandro D'Elia computed the electrical geometry factor. I like to thank Jürgen Halbritter for the reading of this thesis and the many fruitful discussions in Karlsruhe, on the telephone and per email. I like to thank Sarah Aull for the corrections and suggestions she gave on this thesis. The readability certainly improved thanks to her orthographic skills. My gratitude goes to Gianluigi Ciovati for providing me the WinSuper Fit program and the informations about it. I also like thank Bingping Xiao who provided me the latest version of the program and with whom I had many interesting discussions at the SRF conferences and during my visit at JLAB. Furthermore I like to thank Ralf Eichhorn and Jens Knobloch for the opportunity to present this work at their institutes in Darmstadt and Berlin. The initiative for the talk given in Darmstadt came from Sven Sievers, whom I would like to thank for this. The thesis was carried out in the framework of the Gentner Program of the german federal ministry for education and research (BMBF), excellently managed by Michael Hauschild. I like to thank my girlfriend Nadine for the support during the whole time and moving with me to France. Finally, I like to thank my parents for bringing me in this world. Otherwise, writing this thesis would have been sightly more difficult. I always had their full support during my extended studies. Sincere apologies go to anyone whom I may have forgotten.

Contents

1. Introduction

1.1. Applications of Superconducting Cavities

The superconducting technology for radio frequency cavities (SRF) will play a key role for many future high current and/or high energy accelerator projects. It was opted for and successfully exploited in different large scale accelerator projects, such as CERN[1]-LEP[2], JLAB[3]-CEBAF[4] or ONL[5]-SNS[6]. An overview of these projects with a focus on the SRF challenges can be found in [1]. In addition, the SRF technology was selected for future projects such as the European XFEL[7], ESS[8], HIE-ISOLDE[9] and studies, such as the ILC[10] or the CERN-SPL[11], which will push its limits even further. The references given in the footnotes summarize the recent SRF progress for each project or study.

The main advantage of superconducting cavities compared to normal conducting ones is the 5-6 orders of magnitude lower surface resistance R_S, which is proportional to the power dissipated in the cavity walls. Even though superconducting cavities need to be operated at cryogenic temperatures, requiring additional refrigeration power, their application can reduce the required grid power by several orders of magnitude. The highest incentive for using them is therefore for accelerators operated in continuous wave or at high duty cycle.

All accelerators mentioned above rely on cavities made of niobium, the element with the highest critical temperature and critical field [7]. Superconducting cavities of other materials are rarely used. Examples are the PbSn plated accelerators at

[1] European Organization for Nuclear Research

[2] Large Electron-Positron Collider

[3] Thomas Jefferson National Accelerator Facility

[4] Continuous Electron Beam Accelerator Facility

[5] Oak Ridge National Laboratory

[6] Spallation Neutron Source

[7] X-ray Free Electron Laser [2]

[8] European Spallation Source [3]

[9] High Intensity and Energy Isotope On-line Detector [4]

[10] International Linear Collider [5]

[11] Superconducting Proton Linac [6]

the Stoney Brook University [8] (decommissioned in 2007) and the Australian National University (ANU) [9]. The application of new materials, with better superconducting properties than niobium such as Nb_3Sn or Mg_2B is currently under investigation [10]. Another approach to increase the quality factor and accelerating gradient is to use multilayers of superconducting and insulating layers [11]. These new materials and multilayers are investigated by several laboratories for possible future projects, but have not been exploited for particle accelerators yet.

In this thesis focus is set on the widely used niobium technology. Two different methods for manufacturing niobium RF cavities are exploited. They are either built of bulk material or a micrometer thin film[12] is deposited on the inner surface of a copper cavity. The latter approach has been successfully used at CERN for LEP and LHC[13]. It has several advantages compared to the bulk niobium technology. Copper is widely available and can be procured at lower cost, while about 85 % of the world production of niobium comes from only one country, Brazil [12]. Copper has a high thermal conductivity. This helps to avoid one of the possible failures of superconducting cavities, transition to the normal conducting state due to heating of a local defect, called quench. Usually niobium films are of lower purity than bulk niobium. This implies less dissipation from thermally activated normal conducting electrons, because the surface resistance of niobium is not at minimum for highest, but rather for intermediate, purity material. Finally, thin film cavities are less sensitive to trapped flux from the earth's magnetic field. Experiments have shown that the additional dissipation from trapped magnetic flux of thin film cavities is usually negligible compared to the overall losses [13]. For a well prepared cavity of high purity bulk niobium, operated at 2 K, the surface resistance can be several times higher if no shielding against the earth's magnetic field is applied. Therefore, for accelerator projects, based on bulk niobium technology, such as the SPL, magnetic shielding needs to be integrated in the mechanical layout [6], while machines based on the niobium film on copper technology such as LHC or LEP do not require magnetic shielding.

Despite all these advantages of niobium film cavities, bulk niobium technology was chosen for all future superconducting linear accelerator applications relying on a high accelerating gradient, such as CEBAF upgrade, European XFEL and ILC. The reason for this is the lower increase of the surface resistance with accelerating gradient for bulk niobium cavities. The different underlying loss mechanisms are not fully understood yet. An experimental approach to reveal them is the inves-

[12] The thickness of niobium films used for superconducting cavities is large compared to the penetration depth of the RF magnetic field applied. Effects relevant for films of a thickness comparable to this penetration depth are therefore not considered in this thesis.

[13] Large Hadron Collider

tigation of small superconducting samples by RF and surface analytic techniques, as carried out in this thesis.

1.2. RF Characterization of Superconducting Samples

For particle acceleration superconducting cavities are usually operated in their fundamental transversal magnetic mode. This mode is denoted by TM_{010}, where the indices stand for the number of roots the longitudinal electrical field E_z, parallel to the beam axis, has in azimuthal, radial and longitudinal direction [14]. The unloaded quality factor Q_0 of the cavity can be directly measured. It depends on the surface resistance of the material and the cavity geometry:

$$Q_0 = \frac{G}{R_S}, \tag{1.1}$$

where G is the material and size independent geometry factor, relating the surface and the volume magnetic fields to each other

$$G = \frac{\omega_0 \mu_0 \int_V |\vec{B}|^2 \mathrm{d}V}{\int_S |\vec{B}|^2 \mathrm{d}S}, \tag{1.2}$$

with the angular frequency $\omega_0 = 2\pi f_0$, the vacuum permeability μ_0 and the magnetic field $\vec{B}$[14]. Since G is dependent on cavity shape and excited mode, Q-values of different cavities cannot directly compared to each other, if the underlying loss mechanism shall be revealed. The physical value is the surface resistance, inversely proportional to Q. Throughout the whole thesis the surface resistance will be stated. In addition, the frequently used terms Q-Slope and Q-Drop, describing a decreasing (increasing) Q-value (surface resistance) with applied field will also be used. The surface resistance may vary strongly over the cavity surface and the value obtained from Eq. (1.1) is the average R_S over the whole surface [16].

A more convenient way to investigate the surface resistance of superconducting materials is to examine small samples, because they can be manufactured at low cost, duplicated easily and used for further surface analyses. Pillbox cavities excited in the TE_{011}-mode[15] with a sample attached as cover plate are often used

[14] In this thesis the convention of [15] is followed. For simplicity there is no distinction between the magnetic field $\vec{B}$ and the magnetization field $\vec{H}$ unless explicitly stated. This is not necessary, since the magnetic fields of interest are all created by macroscopic currents.

[15] In transversal electric (TE) modes, the indices denote the number of roots the longitudinal magnetic field has in azimuthal, radial and longitudinal direction [14].

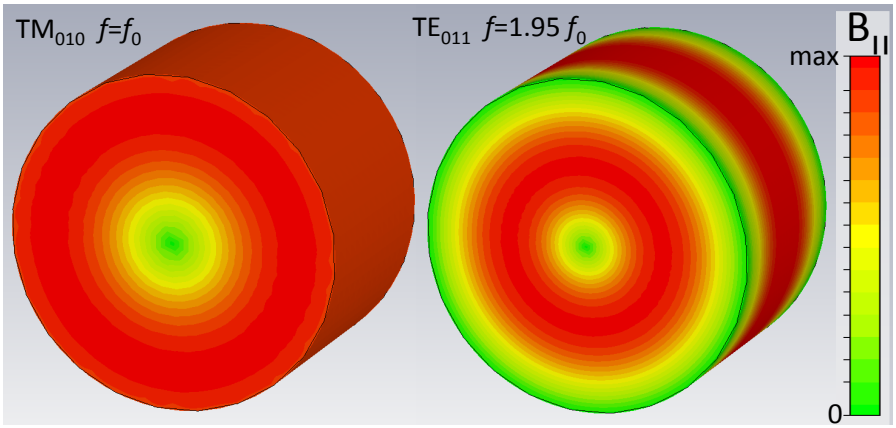

Figure 1.1.: False color plot of the magnetic field $\vec{B}$ parallel to the surface in a cylindrical pillbox cavity excited in the TM_{010} and the TE_{011} mode. The geometry of the cavity is optimized to lowest volume for a given resonance frequency in the TE_{011}-mode. For this geometry the resonance frequency in this TE_{011}-mode is 1.95 times higher than f_0 the resonance frequency of the fundamental TM_{011} mode.

for material characterization. The TE_{011}-mode is chosen, due to its convenient field configuration; It has no magnetic field and therefore no RF currents across the joint, where the demountable end plate sample is attached to the cavity, see Fig. 1.1. The electrical field is vanishing over the whole cavity surface. This helps to avoid multipacting and field emission and enables the separate measurement of losses caused by the magnetic field. The biggest drawback of TE_{011}-cavities is their large size for frequencies of interest concerning accelerator applications. The resonant frequency f_0 of a pillbox cavity with radius r excited in the fundamental TM_{011}-mode is [16]

$$f_0 = \frac{2.405c}{2\pi r}, \tag{1.3}$$

where c is the vacuum velocity of light. When the geometry of the cavity is optimized to lowest volume for a given resonance frequency in the TE_{011}-mode the resonance frequency in this mode is 1.95 times higher than f_0. For example if one wants to investigate samples with a radius of 2.5 cm using such a pillbox cavity, the resonant frequency in the TE_{011}-mode would be 8.96 GHz. This value is large compared to resonant frequencies of superconducting cavities used for particle acceleration, which are between about 70 MHz for heavy ion accelerators [1] and 3.9 GHz for the third harmonics cavities of the Free-Electron LASer in Hamburg (FLASH) [17].

There are three measurement techniques to derive the surface resistance of superconducting samples. In the following, these approaches are briefly introduced and an overview of systems currently in use for superconducting cavity material

characterization is given.

The end-plate replacement technique is used since more than 40 years [18]. It requires a reference sample of known surface resistance R_S. Once the quality factor of the cavity with the reference sample attached has been measured it can be exchanged by another sample of unknown surface resistance. From the change in Q-value the surface resistance of the sample can be derived.

Despite of its lower resolution compared to the other techniques introduced below, this approach is still used, since it allows for designing simple systems and performing quick tests. Recent measurements on Mg_2B samples performed with a mushroom shaped TE_{013}-cavity at Stanford Linear Accelerator Center (SLAC) can be found in [19]. Unlike all other systems which will be mentioned in this section this cavity is not built of a superconducting material, but of copper. This has the advantage that the cavity cannot quench and its surface resistance is independent of electromagnetic field strength. The drawback is an even lower sensitivity compared to a system of identical shape and measurement technique made of a superconducting material. The copper cavity gives an accuracy of 0.1-0.2 mΩ at 11.4 GHz, which corresponds to approx. 1-2 $\mu\Omega$ at 1.3 GHz. Niobium cavities operated at this frequencies typically have surface resistances of a few nanoohms [20]. Therefore, two cavities of identical shape, but different material are currently being developed. One will be made of bulk niobium while the other one will be made of a thin niobium film sputter coated onto a copper cavity [19].

The thermometric technique allows to derive R_S independently of a reference sample. Placing several temperature sensors on the back side of the sample enables to obtain R_S from the temperature increase caused by RF exposure. This technique requires knowledge of the heat capacity and thermal conductivity of the sample material for an accurate absolute measurement of the sample surface resistance.

At Cornell University a sensitivity of about 10 nΩ has been achieved with a 5.9 GHz niobium pillbox cavity excited in the TE_{011}-mode. They will also apply the thermometric technique to a mushroom shaped cavity which can be exited at 4.8 GHz (TE_{012}-mode) and 6.2 GHz (TE_{013}-mode) [21]. The two cavities will be used to test Nb_3Sn samples produced by vapor diffusion coating process [22].

The RF-DC compensation technique allows to derive the surface resistance from a DC measurement. In a calorimetric system the sample and the host cavity are thermally decoupled. A DC heater (resistor) and at least one temperature sensor are attached to the back side of the sample. This allows for independent control of the sample temperature. For details on this technique, see Sec. 3.3. Currently,

there are three calorimetric systems for the RF characterization of superconducting samples in use.

A cylindrical TE_{011}/TE_{012}-cavity enabling measurements at 4 and 5.6 GHz has been developed in collaboration between CEA Saclay and IPN Orsay [23, 24]. The cavity has been used for systematic studies of the surface resistance of sputtered niobium on copper samples. Substrates of different roughness have been investigated. A correlation between substrate roughness and surface resistance was found [23]. Recently, a modified version of this cavity has been constructed and commissioned for investigations of thin film samples of different materials [25].

At JLAB a sapphire loaded TE_{011}-cavity for measurements at 7.5 GHz has recently been commissioned [26]. It was designed to measure the surface impedance of samples sufficiently small to be accommodated in commercial surface characterization instruments, surface treatment facilities and laboratory-based thin film deposition equipment. Placing a sapphire rod in the middle of a cylindrical cavity lowers the resonant frequency, allowing to install samples of 50 mm diameter as end plate in a 7.5 GHz cavity. The cavity has been commissioned with a bulk niobium sample brazed on to a copper substrate and recently been used for tests of a MgB_2 sample [27].

The Quadrupole Resonator at CERN is the only system running at frequencies of interest concerning accelerator applications. It can be excited at 400 MHz and multiple integers of this frequency. Its design, based on a four wire transmission line resonator, yields a geometry, where the sample size is independent of the resonance frequency. While the samples of all other systems introduced above are only exposed to magnetic field, the Quadrupole Resonator samples are exposed to electric and magnetic RF fields simultaneously, as are superconducting cavities operated in the accelerating TM_{010}-mode. The Quadrupole Resonator has been used since 1999 for measurements at 400 MHz [28–30]. It has been refurbished in the framework of this thesis for measurements at 400, 800 and 1200 MHz and also to probe the critical RF magnetic field of different samples [31–33]. A detailed description of the device will be given in Chap. 3.

1.3. Objectives and Structure of this Thesis

Identifying the loss mechanisms of superconducting niobium enables an accurate determination of design parameters for future accelerators and points to research topics required to mitigate present limitations. The power consumption of a cavity is proportional to its surface resistance R_S. The two fluid model, introduced in Chap. 2, describes how R_S depends on temperature, frequency and to some extent on the purity of the material. A better agreement with experimental results, especially for materials of low purity, is achieved by using the microscopic BCS theory. According to BCS theory and the two fluid model R_S is independent of applied field strength and vanishes at zero Kelvin. Since this is in contradiction to cavity measurements, several models accounting for these additional field dependent and residual losses have been proposed. They are reviewed in Chap. 2. None of them can explain all experimental results and there is strong evidence that some loss mechanisms are only relevant if certain surface preparations are applied. Ultimately performance of superconducting cavities is limited by the critical RF magnetic field $B_{\mathrm{crit,RF}}$, which in the case of niobium can exceed the thermodynamic critical field, at least for temperatures close to the critical temperature. Whether $B_{\mathrm{crit,RF}}$ is limited by a metastable superheating field or by a field related to a thermodynamic energy balance (vortex line nucleation model) is an open issue and is especially relevant for the application of materials other than niobium for possible future accelerator projects.

In order to measure R_S and $B_{\mathrm{crit,RF}}$ over a wide parameter range on superconducting samples representing cavity surfaces, the 400 MHz Quadrupole Resonator has been refurbished. Its mechanical and electromagnetic layout are studied in detail in order to extend the measurement range to 800 and 1200 MHz, see Chap. 3. The magnetic field distribution on the sample surface is almost identical at 400, 800 and 1200 MHz, while the ratio between the electric and magnetic field is highly dependent on frequency. This allows for unique material test, especially for investigations of the field dependent surface resistance.

Measurement results on R_S and $B_{\mathrm{crit,RF}}$ obtained with the Quadrupole Resonator are presented in Chap. 4 and compared with the predictions given from the models, introduced in Chap. 2. Investigated are bulk niobium and niobium thin film on copper substrate samples. The field dependent surface resistance of well-prepared bulk niobium is found to be caused by the magnetic field and factorizes in field and temperature dependent parts. For a strongly oxidized niobium thin film sample it has been measured that the increase of R_S is mainly caused by the surface electric field. This increase depends only slightly on temperature. An explanation for these observations is given by a novel interpretation of the interface tunnel exchange model. For samples of low purity the vortex line nucleation model gives a lower predictions for $B_{\mathrm{crit,RF}}$ than the superheating field model. For niobium

of high purity it is the other way round. It is measured that the lower estimate always defines $B_{\mathrm{crit,RF}}$. Therefore both models can set limitations to $B_{\mathrm{crit,RF}}$.

In order to correlate the different loss mechanisms to the surface properties, the samples have been tested by various surface analytic measurements, see Chap. 5. The roughness has been measured with white light interferometry and atomic force microscopy. A light microscope and a scanning electron microscope have been used to determine the grain size of the different samples. Their material composition and distribution of oxides on the sample surfaces have been examined by ultrasonic force microscopy and X-ray photon spectroscopy. From the combined results it is found that the small grain size and high Nb_2O_5 content of niobium thin film samples can give rise to crack corrosion along grain boundaries. This causes the additional losses from interface tunnel exchange.

2. Performance of Superconducting Cavities

Superconductivity was discovered 1911 by Kammerlingh Onnes. He measured a vanishing resistance of mercury, when cooled in a liquid helium bath to 4.2 K [34]. The charge carriers in the superconducting state are called Cooper pairs. A Cooper pair is a bound state of two electrons with opposite spin. It can move through the lattice without being scattered, resulting in zero resistance. Vanishing losses are only observed for direct currents (DC). A superconductor carrying an alternating current (AC) has a non-vanishing surface resistance for temperatures above 0 K [35]. An explanation for this effect is given in Sec. 2.2. While the increase of the surface resistance with temperature at low magnetic field is well understood, there is no widely accepted model, which can explain how the RF losses are correlated to the applied electromagnetic field strength [36, 37]. Several models accounting for this field dependent surface resistance are introduced in Sec. 2.3.

Since the first exploration of superconducting cavities in 1965 at Stanford University [38] their performance has been steadily increased. The first cavities were limited by multi impact electron amplification (multipacting) to accelerating gradients of about 2 MV/m. This limitation has been overcome by rounding the edges, which resulted in an elliptical cavity shape. Afterwards superconducting cavities were either limited by thermal breakdown (quench) or field emission [16]. Multipacting and field emission are described in the Appendix, while thermal breakdown is subject of Sec. 2.4.5. High pressure rinsing and clean room assembly can suppress field emission, while thermal breakdown can be shifted to higher fields by using high purity niobium with a good thermal conductivity [39].

A few single cell cavities have recently reported to be performing at or close to the theoretical limit set by the critical RF field [40]. The exact value of this field and its correlation to the surface properties have been under investigation for more than 30 years [41], but are not fully understood yet, see Sec. 2.4. The majority of superconducting cavities produced, however, are not reaching such high accelerating gradients at an economical quality factor. They are limited by an exponential increase of the surface resistance at high fields [39]. This effect is referred to as Q-Drop and can occur without field emission.

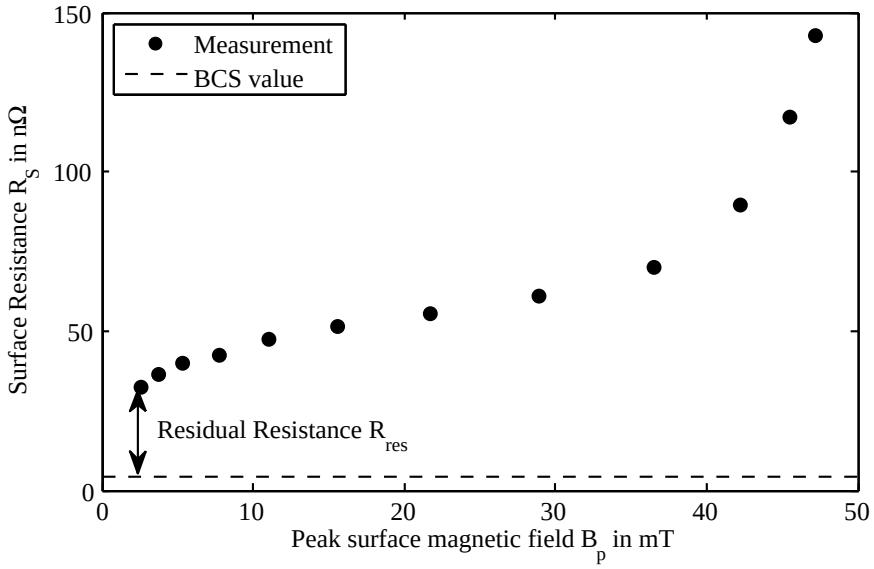

Figure 2.1.: Surface resistance of a 400 MHz LHC cavity measured at 2.5 K for acceptance test in 1999 [42–44]. The uncertainty is about 10 % for each data point. The BCS value has been calculated using [45].

2.1. Performance of LHC Cavities

The LHC cavities are built of a micrometer thin niobium film DC magnetron sputtered onto a copper cavity. The same technology was already applied for the upgrade of LEP [46]. Figure 2.1 shows the surface resistance as a function of peak magnetic field B_p of a 400 MHz LHC cavity measured at 2.5 K[1]. The curve displayed was measured in a vertical cryostat in February 1999 in the framework of the acceptance tests for the LHC. The performance of the cavity fulfilled the requirements to be installed in the accelerator [42–44]. The uncertainty of the measured surface resistance is approximately 10 % for each data point [47]. An exact error calculation is not available, since this was not of interest for the acceptance tests.

The surface resistance for lowest field value is about 30 nΩ higher than predicted for losses from thermally activated normal conducting electrons (BCS value) [45]. This residual resistance R_res is a general property of superconductors and therefore also observed for bulk niobium cavities. Recent tests of such cavities used for CEBAF, XFEL and SNS show that a residual resistance of approximately 10 nΩ can be obtained on a regular basis for this technology [48]. Similar values have been achieved on 1.5 GHz single cell niobium film on electropolished copper substrate

[1] In the LHC the cavities are operated at 4.5 K, but in the framework of the acceptance tests, measurements at 2.5 K have also been included.

cavities [49].

For fields below 5 mT a strong increase $R_S(B_p)$ is observed in Fig. 2.1. This effect is usually not seen for bulk niobium cavities. Here, the opposite behavior is often measured. The surface resistance is decreasing up to fields of a few mT, where R_S is at minimum [16]. In the field region between 5 and 30 mT the surface resistance of the LHC cavity, Fig. 2.1, increases less strongly with B_p as for lowest fields, indicating a saturating loss mechanism.

Above 40 mT the surface resistance of the LHC cavity (Fig. 2.1) increases exponentially. This value is low compared to bulk niobium cavities. Here the onset of the exponentially increasing surface resistance (Q-Drop) is usually measured at 100-130 mT [1]. In case of the data displayed in Fig.2.1 the exponential increase coincided with the observation of X-rays. The cause can therefore be identified with field emission. Technically it is incorrect to calculate a surface resistance from a Q_0 measurement when the losses are caused by field emission. The direct measure was Q_0 and R_S was derived using Eq. (1.1). Nevertheless, it was chosen to display the surface resistance as a function of field here, so that the curve can later be compared with measurements carried out with the Quadrupole Resonator in the framework of this thesis.

2.2. Low Field Surface Impedance

2.2.1. The Two Fluid Model of Superconductivity

The surface resistance of superconductors can be understood in the framework of the two fluid model [50]. It assumes that the current in the superconductor is carried by two components (fluids). One component, moving without friction, but carrying inertia is represented by the Cooper pairs. The other component is identified by thermally activated, normal conducting electrons.

Consider an alternating magnetic field $B_x(t) = B_0 e^{i\omega t}$ parallel to the surface of a superconductor. The superconductor shields its interior from the magnetic field by a current on its surface. The magnetic field is only able to penetrate in a depth λ (typically a few tens of nanometers for niobium). This is defined as the z-direction here, while x and y are perpendicular to z and parallel to the superconductor's surface.

From Faraday's law of induction the induced electric field $\vec{E}$ created from the time varying magnetic field $\vec{B}$ in the surface layer is

$$\oint_S \vec{E} \mathrm{d}l = -\frac{\mathrm{d}}{\mathrm{d}t} \int \int \vec{B} \mathrm{d}x \mathrm{d}z. \tag{2.1}$$

Assuming the magnetic field to be exponentially decaying over the penetration

depth λ, as predicted by London theory [51]

$$\vec{B} = \vec{B}_0 e^{-z/\lambda}, \tag{2.2}$$

for a sufficiently large integration area ($z \gg \lambda$) Eq. (2.1) can be written as

$$\int \vec{E} \mathrm{d}x = -i\omega\lambda \int \vec{B} \mathrm{d}x. \tag{2.3}$$

Since Eq. 2.3 is also locally valid [52], one can obtain

$$\vec{E} = -i\omega\lambda\vec{B}. \tag{2.4}$$

The power dissipated in the material is

$$P = \int \sigma |\vec{E}|^2 \mathrm{d}V = -\lambda\sigma \int |\vec{E}|^2 \mathrm{d}x\mathrm{d}y, \tag{2.5}$$

where $\vec{E}$ is averaged over time. The normal state conductivity at the transition temperature σ is related to the purity of the material, via the residual resistance ratio RRR

$$\sigma = RRR \cdot \sigma_0,$$

with the conductivity at room temperature σ_0. Combining Eqs. (2.4) and (2.5) yields

$$P = \omega^2\lambda^3\sigma \int |\vec{B}|^2 dxdy. \tag{2.6}$$

The surface resistance R_S describes the power dissipated over an area $A = \mathrm{d}x\mathrm{d}y$

$$P = \frac{R_\mathrm{S}}{\mu_0^2} \int |\vec{B}|^2 \mathrm{d}x\mathrm{d}y. \tag{2.7}$$

Equating the right sides of Eqs. (2.6) and (2.7) and resolving with respect to R_S yields the surface resistance of a superconductor in the two fluid model

$$R_\mathrm{S} = \sigma\mu_0^2\omega^2\lambda^3. \tag{2.8}$$

A surprising result from this derivation is that the surface resistance in the superconducting state is proportional to the normal state conductivity σ. This becomes clear when the correlation of σ to the density of thermally activated normal conducting electrons n is considered. This number is zero for T=0 K and increases exponentially with temperature up to T_c, where all Cooper pairs have

been thermally activated to normal conducting quasiparticles:

$$R_{\mathrm{S}} \propto \sigma_0 \propto n \propto \exp\left(-\frac{\Delta}{k_{\mathrm{B}}T}\right), \quad T < \frac{T_{\mathrm{c}}}{2}, \tag{2.9}$$

where Δ is the superconducting energy gap and k_B the Boltzmann constant.

Equation (2.8) is the real part of the magnetic surface impedance Z_H. The imaginary part is correlated to the magnetic field penetration depth λ

$$\mathrm{Im}Z_H = X_H = \omega\mu_0\lambda. \tag{2.10}$$

The two fluid model can qualitatively describe the temperature dependence of superconducting cavities, except for a residual resistance R_{Res} typically of a few nanoohms. The quadratic increase with frequency is well observed for frequencies below approx. 10 GHz [53]. Corrections to the two fluid model, considering the microscopic BCS theory are introduced in the following section. These corrections enable to give quantitative predictions for the surface resistance for fields below approx. 15 mT [53].

2.2.2. BCS Treatment of Linear Surface Resistance

In 1957 Bardeen, Cooper and Schrieffer introduced the first microscopic theory of superconductivity [54]. Based on this BCS theory expressions for the surface impedance have been worked out by Mattis and Bardeen [55]. The expressions have been derived using zero field perturbation theory. Therefore it is not surprising that they are only valid for low electromagnetic fields. It is impossible to give a simple analytical formula for the surface resistance as a function of temperature, frequency and possible other parameters, as has been done using the two-fluid model, Eq. (2.8). Usually the computer code written by Halbritter is used for the calculation of R_{S} for given input parameters [45].

The Mattis-Bardeen expressions involve material parameters, like the BCS coherence length ξ_0, the London penetration depth λ_L and the electron mean free path l. While the two fluid model not considering these parameters can only give a qualitative description of measurement results, the BCS theory agrees quantitatively with measurements for cavities of high and low purity. For example the two fluid model predicts the surface resistance to be at minimum for cavities of lowest purity (lowest RRR). In reality the minimal surface resistance is neither obtained for cavities of very low purity as predicted from the two fluid model, nor for cavities of highest purity. In fact it is obtained for intermediate purity, where $l \approx \xi_0$, which corresponds to a RRR of approx. 10 in case of niobium. This is the regime of sputter coated niobium cavities as used for LEP and LHC. The low BCS

resistance, which also stems from their low resonant frequency, allows for economic operation at 4.5 K. For $l < \xi_0$, the surface resistance is decaying with l. In this regime R_S is dominated by impurity scattering. A useful approximation to the Mattis-Bardeen expressions in the "dirty limit" ($l \ll \xi_0$) is [1]:

$$R_{\mathrm{BCS}} = \mu_0^2 \omega^2 \sigma_0 RRR \cdot \lambda(T,l)^3 \frac{\Delta}{k_B T} \ln\left(\frac{\Delta}{\hbar\omega}\right) \frac{e^{-\Delta/k_B T}}{T}. \tag{2.11}$$

In the "clean limit" ($l \gg \xi_0$) the surface resistance becomes independent of the material purity. In this regime a useful approximation is [1]

$$R_{\mathrm{BCS}} \simeq \frac{3\Delta}{2k_B T} \mu_0^2 \omega^2 \sigma_0 RRR \cdot \frac{\lambda(T,l)^4}{l} \ln\left(\frac{1.2 T \Delta \xi_0^2}{\hbar^2 \omega^2 \lambda(T,l)^2}\right) e^{-\Delta/k_B T}. \tag{2.12}$$

The formula is altered compared to [1] to replace the effective conductivity σ_{eff} by the conductivity at room temperature σ_0, since for this parameter literature values are available [7].

The Mattis-Bardeen expressions as well as the approximations (Eqs. 2.11 and 2.12) enable to give qualitative predictions for the surface resistance for fields well below the critical RF field $B_{\mathrm{max,RF}}$. This theory predicts R_S to be independent of $\vec{B}$. In the following this contribution is referred to as the linear resistance. Linear resistance means that the magnetic field is a linear function of the electric field and Ohm's law applies. If R_S itself depends on the magnetic field it is referred to as non-linear.

The total surface resistance can be written as a sum of the BCS, the residual and non-linear contributions, denoted by R_{nl}:

$$R_S = R_{\mathrm{BCS}} + R_{\mathrm{res}} + R_{\mathrm{nl}}, \tag{2.13}$$

where the residual resistance R_{res} is not explained by BCS theory either. While the linear BCS surface resistance R_{BCS} is well understood, there is no widely accepted theory for the non-linear surface resistance R_{nl} and the residual losses. In the following section several models accounting for these will be introduced.

2.3. Non-Linear Surface Resistance and Residual Losses

In this section different models, which go beyond just qualitatively explaining the non-linear surface resistance are briefly summarized. All these models comprise quantitative formulas for R_{nl} as a function of RF field in the medium field region

(below about 100 mT), which can be tested by RF measurements. Arguments are given as to whether or not these models can account for differences observed between bulk niobium and niobium film cavities.

2.3.1. Pair Breaking, Thermal Feedback, Impurity Scattering and Localized Heating

Pair breaking In BCS theory the energy gap Δ depends on temperature only. It is considered to be independent of the applied magnetic field. For the clean limit Gurevich worked out a theory considering breaking of Cooper Pairs in a current carrying state. *Pair breaking* yields an increased density of normal conducting electrons, corresponding to a decreased energy gap

$$\Delta(v_\mathrm{s}) = \Delta - p_\mathrm{F}|v_\mathrm{s}|, \tag{2.14}$$

vanishing at the critical velocity $v_\mathrm{c} = \Delta/p_\mathrm{F}$, with the Fermi momentum p_F and the superfluid velocity $|v_\mathrm{s}|$. Equation 2.14 allows to derive a quantitative expression for the non-linear surface resistance, including a quadratic increase for intermediate fields (Medium Field Q-Slope) and an exponential increase for a peak magnetic field $B_\mathrm{p} > TB_\mathrm{c}/T_\mathrm{c}$ (Q-Drop), where B_c is the critical thermodynamic field. For intermediate fields R_nl reads [56]:

$$R_\mathrm{nl} \simeq \left[\frac{\pi^2}{384}\left(\frac{\Delta}{k_\mathrm{B}T}\right)^2\left(\frac{B_\mathrm{p}}{B_\mathrm{c}}\right)^2\right] R_\mathrm{BCS}. \tag{2.15}$$

In general R_nl is a local property. If measurements on a surface exposed to an inhomogeneous RF field are analyzed this has to be taken into account. Note that Eq. 2.15 predicts the Q-slope to be more pronounced at lower temperatures. This assumption can be conveniently tested on a single cavity or sample. In general, experiments showed steeper Q-slopes than predicted by Eq. (2.15). An explanation can be given by the thermal feedback model [57, 58] or additional heating at hot spots.

Thermal Feedback The underlying idea of the thermal feedback model is that the inner side of the cavity has a higher temperature than the outer side in direct contact to the liquid helium bath. RF heating increases the inner wall temperature of the cavity, yielding a higher surface resistance and therefore additional losses. A temperature gradient between the RF side and the helium bath is created. For a higher field this gradient is larger and therefore the additional losses increase. The stronger medium field Q-slope of niobium film cavities can only be explained by this model, if there is a high temperature gradient at the interface between the

superconducting film and the copper substrate. Otherwise it can be excluded as the major contribution due to the generally better thermal conductivity of copper compared to niobium.

Impurity Scattering Equation 2.15 is valid only for the clean limit ($l \gg \xi$) and is therefore not applicable to niobium film cavities. So far in literature *impurity scattering* has only been taken into account by a first order quadratic correction to the BCS resistance R_{BCS} [59]

$$R_{\mathrm{nl}} \simeq \left[\gamma(l,\omega,T)\left(\frac{B_{\mathrm{p}}}{B_{\mathrm{c}}}\right)^2\right] R_{\mathrm{BCS}}, \tag{2.16}$$

where $\gamma(l,\omega,T)$ is a function of the mean free path l, temperature T and frequency f. The authors of [59] claim that in the clean limit γ is of the order of unity in Nb at T=2 K and increases as the temperature decreases, similar to Eq. (2.15). Note that the larger γ becomes, the smaller the field range in which the first order expansion in Eq. (2.16) is valid. According to [59], γ decreases with l. The BCS non-linearity is less pronounced if the surface layer is more contaminated with impurities [59]. This is in contradiction to the stronger Q-slope observed for niobium film cavities and the considerations of Palmieri [60].

Weak Layer Palmieri finds that the medium Q-slope is more pronounced for cavities with a low mean free path l. In [60] he proposes a model which gives a quantitative expression for the low field Q-increase, the medium field Q-slope and the Q-drop based on a weak superconducting layer on top of the bulk material with standard superconducting properties. To account for the medium field Q-slope the model comprises Eq. (2.14). This implies

$$R_{\mathrm{BCS}} \propto \exp\left(-\frac{\Delta(v_{\mathrm{s}})}{k_{\mathrm{B}}T}\right) = \exp\left(-\frac{\Delta}{k_{\mathrm{B}}T} + \frac{p_{\mathrm{F}}v_{\mathrm{s}}}{k_{\mathrm{B}}T}\right), \tag{2.17}$$

Palmieri introduces

$$\frac{p_{\mathrm{F}}v_{\mathrm{s}}}{k_{\mathrm{B}}T} = \frac{B_{\mathrm{p}}\lambda_0 e v_{\mathrm{F}}}{k_{\mathrm{B}}T}\left(\frac{1}{\rho_{\mathrm{s}}}\right)^{1/2} \tag{2.18}$$

and

$$\frac{1}{\rho_{\mathrm{s}}} = \coth\left(\frac{l}{\xi_0}\right), \tag{2.19}$$

where ρ_{s} is the superfluid density, which is one at zero Kelvin and vanishes at the critical temperature. The coth-dependence on mean free path could well account for the stronger Q-slopes observed for niobium film cavities, because for small

values of l the superfluid density is reduced, resulting in a higher surface resistance. Like all other models based on pair breaking in the current carrying state, this model does not predict a clear factorization of the non-linear surface resistance in a temperature and a field dependent part, as found for bulk niobium [61] and as well for niobium film cavities [62].

Localized heating Localized heating at *hot spots* can account for differences observed between niobium film and bulk niobium cavities. By transmission electron microscope (TEM) measurements the defect density in a bulk niobium sample was found to be about three orders of magnitude lower than in several niobium film samples [63]. In [56] Gurevich considers localized heating at defects and derives

$$R_{\mathrm{nl}} = (R_{\mathrm{BCS}} + R_{\mathrm{res}}) \left[\frac{g}{1 - (B_{\mathrm{p}}/B_{\mathrm{b0}})^2} \right], \tag{2.20}$$

where B_{b0} is the quench field in absence of defects and g is a parameter which is related to the number and intensity of the hot spots.

2.3.2. Percolation Model

A recent explanation for the non-linear surface resistance is based upon the two fluid model [61, 64, 65]. The main idea of this *percolation model* is that non-linear surface resistance is caused by gradual entry of magnetic flux increasing with the RF amplitude up to the formation of complete flux tubes. The gradual entry describes the medium field Q-slope, while the creation flux tubes triggers the Q-Drop.

For a clean type II superconductor it is energetically favorable to allow flux to enter at its lower critical field B_{c1}. The percolation model suggests a mechanism allowing flux to enter locally already at a field level below B_{c1}. In the vicinity of a small normal conducting defect with a radius $r \ll \xi, \lambda$ magnetic flux entry becomes energetically favorable already at [61]

$$B^* = \frac{1}{\kappa^{3/2}} B_{\mathrm{c}}. \tag{2.21}$$

In a dirty superconductor, where ξ is locally suppressed and therefore $\kappa = \lambda/\xi$ locally enhanced, flux entry may become energetically favorable already at very low fields. Note that the coherence length ξ is related to the electron mean free

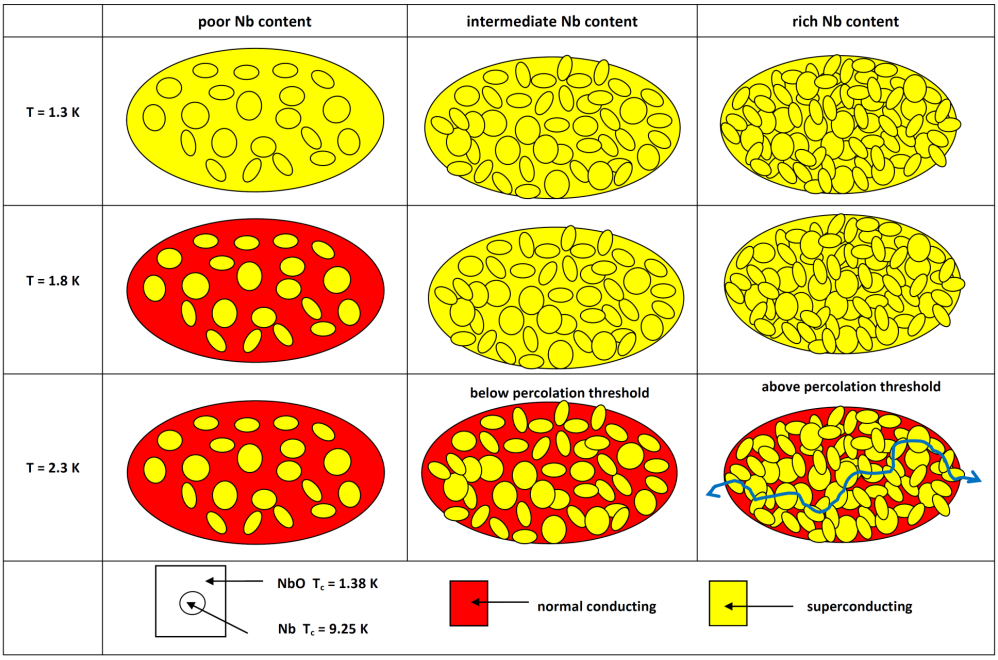

Figure 2.2.: NbO in close contact to niobium. Left: In case of poor niobium content the NbO becomes normal conducting above its transition temperature. Middle: For intermediate niobium content the whole composite remains superconducting up to a higher temperature by proximity effect. Right: For sufficiently large niobium content, the niobium is able to form superconducting paths of its own through the composite. The NbO is now found in the form of small separated normal conducting islands. These islands can serve as condensation nuclei for magnetic flux entry. Courtesy of W. Weingarten.

path via [2] [66]

$$\frac{1}{\xi} = \frac{1}{\xi_0} + \frac{1}{l}, \tag{2.22}$$

with the BCS coherence length ξ_0. The percolation model identifies these small nuclei by isolated NbO islands surrounded by niobium, forming a superconducting path through the composite above the percolation temperature T'=2.015 K if the niobium content is sufficiently large, see Fig. 2.2. For the qualitative derivation of the surface resistance it is assumed that starting at T' the amount of condensation

[2] For this consideration it is not distinguished between the BCS and the Ginsburg-Landau coherence length.

nuclei is increasing linearly with temperature, yielding

$$R_{\mathrm{nl}} = \left[R_{\mathrm{Resl}} + \mu_0^2 \omega^2 \sigma_0 RRR \cdot \Delta x^3 \Theta(T' - T) \left(\frac{(T - T')}{(T_{\mathrm{c}} - T')} \right) \right] \cdot (-1) \left[\frac{1}{\kappa^2} + \frac{\ln \left[1 - \kappa^2 \left(\frac{B_{\mathrm{p}}}{B_{\mathrm{c}}(T)} \right)^2 \right]}{\kappa^4 \left(\frac{B_{\mathrm{p}}}{B_{\mathrm{c}}(T)} \right)^2} \right], \tag{2.23}$$

where the parameter Δx must be interpreted as an effective penetration depth of the non-linear surface resistance R_{nl}. Equation (2.23) predicts R_{nl} to increase with a leading quadratic term up to a threshold field $B_{\mathrm{th}} = B_{\mathrm{c}}/\kappa$. At B_{th} the Q-drop starts, explained by the singularity of Eq. (2.23).

The quadratic increase of R_{nl} with peak magnetic field B_{p} becomes apparent after expanding the logarithm of Eq. (2.23) into an infinite but slowly converging series

$$R_{\mathrm{nl}} = \left[R_{\mathrm{Resl}} + \mu_0^2 \omega^2 \sigma_0 RRR \cdot \Delta x^3 \Theta(T' - T) \left(\frac{(T - T')}{(T_{\mathrm{c}} - T')} \right) \right] \cdot \frac{1}{\kappa^2} \left[\frac{\left(\frac{\kappa^2 B_{\mathrm{p}}}{B_{\mathrm{c}}(T)} \right)^2}{2} + \frac{\left(\frac{\kappa^2 B_{\mathrm{p}}}{B_{\mathrm{c}}(T)} \right)^4}{3} \ldots \right]. \tag{2.24}$$

Currently, there is no experimental evidence opposing the predictions from the percolation model. Being only recently published, little effort has yet been made to test this model by experiments.

2.3.3. Interface Tunnel Exchange

So far only the magnetic surface impedance Z_H has been considered. It only accounts for losses from the transverse wave and neglects any losses from the longitudinal field component $E_\perp$. Analogous to (2.7) one can define the electric surface resistance $R_{\mathrm{S}}^{\mathrm{E}}$ [52]:

$$P = \frac{1}{2} \frac{\varepsilon_0}{\mu_0} R_{\mathrm{S}}^{\mathrm{E}} \int E_\perp^2 \mathrm{d}A. \tag{2.25}$$

Usually this contribution is negligible in the GHz regime, even for normal conducting metals [52]. However, the fact that niobium oxidizes suggests to investigate the influence of the metal-oxide-adsorbate system on the surface resistance [68]. This system is sketched in Fig. 2.3 in stoichiometry (left) and in energy (right)

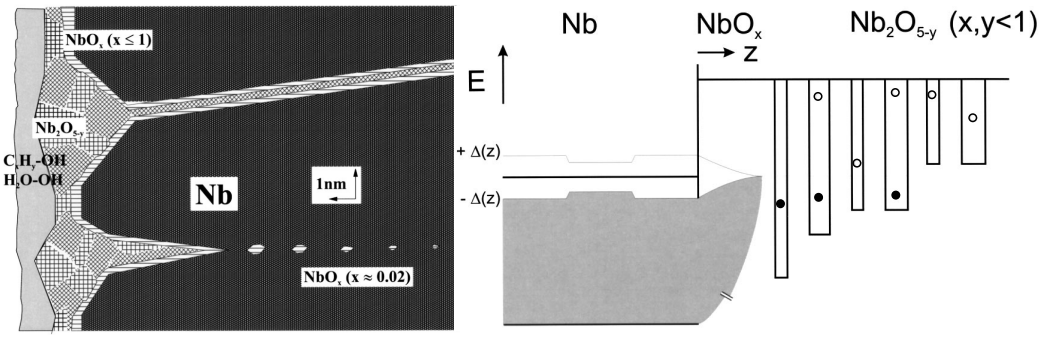

Figure 2.3.: Right: Stoichiometry of an oxidized niobium surface with crack corrosion. For sputtered Nb the oxidation proceeds preferentially along the grain boundaries. Left: Corresponding band structure at a Nb-NbO$_x$-Nb$_2$O$_{5-y}$-interface. The superconducting energy gap Δ is being reduced in NbO clusters or interfaces. At the Nb-NbO interface the energy gap is enhanced due to strain from diffusing and participating oxygen [67]. Courtesy of J. Halbritter.

[67]. NbO is a superconductor with a transition temperature T_c=1.38 K [7]. By proximity effect it remains superconducting at higher temperature at the interface to the niobium with an energy gap decreasing with distance to the niobium, see Fig. 2.3. Nb_2O_5 is an insulator with a relative dielectric constant $\epsilon_r \cong$ 10-15. When the RF field is raised the longitudinal electric field only penetrates the insulator. It becomes now energetically favorable for electrons to tunnel to the superconductor and when the field is lowered to return. This process occurs within a single RF cycle, yielding linear frequency dependence for this loss mechanism. The barrier height for tunneling between the localized states in the insulator at crystallographic shear planes is approx. 0.1-1 eV [68].

The exchange is quantitatively governed by the tunnel rate between the localized states in the oxides and the states in the metal. In a superconductor this exchange only occurs if the energy gained is larger than the energy gap Δ. Therefore, losses only occur above a threshold field E^0. An exponential increase of the surface resistance above E^0 saturating at higher field, when all localized states participate in the exchange is predicted from this model. The electrical surface resistance R_S^E due to this loss mechanism is called interface tunnel exchange (ITE) and can be written as [57]

$$R_S^E = R_{S,400}^E \frac{f}{400\,\mathrm{MHz}} \left[e^{-b/E_p} - e^{-b/E^0} \right], \quad E_p \geq E^0, \tag{2.26}$$

with b=$2\alpha\Delta\epsilon_r/e\beta_{FE}$. Where $\alpha \cong$ (1.6-5.3) nm^{-1} is the decay constant of the wave function into Nb_2O_5, $\epsilon_r \cong$ 10-15 the relative dielectric constant of Nb_2O_5 and β_{FE} the static field enhancement factor [57, 67, 69]. Here, the electric surface resistance at saturation, where all available states participate in the exchange, $R_{S,400}^E$

is normalized to the lowest used resonant frequency of the Quadrupole Resonator.

Crack corrosion at grain boundaries can yield spots for tunneling, see Fig. 2.3 (left). Losses due to interface tunnel exchange might therefore be more pronounced in sputtered cavities, since they have usually smaller grain sizes than bulk niobium cavities. An exponential increase saturating at about 5 mT is well observed for the LHC cavity, see Fig. 2.1. The interface tunnel exchange model can therefore describe the differences observed between bulk niobium and niobium film cavities in this low field region.

Equation (2.26) does not account for a possible role of ITE for the Q-drop, which is explained in [70]. Since ITE losses are more pronounced in niobium film cavities, the model can well describe their earlier onset of the Q-drop. There are mainly two observations opposing ITE to be responsible for the Q-drop at least for bulk niobium cavities. Temperature mapping generally shows localized heating in the high magnetic field region when the Q-Drop occurs and one cavity exited in a TE mode with no electric surface fields also exhibited Q-Drop [71, 72].

2.3.4. Residual Losses

The two fluid model and the BCS theory predict the surface resistance to vanish at T=0 K. This is not observed in measurements. A residual resistance of usually several nanoohms is measured for niobium cavities. The lowest value ever achieved is 0.5 nΩ [73]. Measured with a multimode cavity R_{Res} was found to scale with $f^{1.8}$ [74] for bulk niobium. This is close to the quadratic prediction for the losses caused by thermally activated normal conducting electrons from the BCS theory and the two fluid model. In [61] an explanation for this contribution is given in the framework of the two fluid model. Assuming normal conducting electrons in a surface layer Δy of a few nanometers, seeing the same field as the thermally activated electrons, yields a temperature independent expression for the residual resistance analogous to the two fluid model [61]

$$R_{\mathrm{Res}} = \mu_0^2 \omega^2 \sigma_0 RRR \cdot \lambda_0^2 \Delta y. \tag{2.27}$$

The same expression has already been found independently in 1984 [75]. It is known from thermometry studies that the residual losses are localized and not evenly distributed over the whole cavity surface [76], therefore Δy can only be understood as an effective penetration depth correlated to the mean defect density of the material.

Recent analyses of the surface resistance of almost 200 bulk niobium cavities with frequencies of 805, 1300 and 1497 MHz suggest that the residual resistance

comprises of a frequency independent part additive to Eq. (2.27)

$$R_{\mathrm{Res}} = R_{\mathrm{Res2}} + \mu_0^2 \omega^2 \sigma_0 \cdot RRR \cdot \lambda_0^2 \Delta y. \tag{2.28}$$

This is also considered in [61].

A residual resistance scaling linearly with frequency was found for niobium films, using a sample cavity, excited in two TE-modes [24]. Since these losses were measured in TE-modes, where the sample was only exposed to a surface magnetic field, allows concluding that these losses originate from the surface magnetic and not from the surface electric field.

One well known contribution to the residual resistance is caused by trapped magnetic flux. A perfect superconductor expels all the flux out of its bulk in the very moment of the phase transition from the normal to the superconducting state. However, impurities can impede the complete expulsion of the magnetic flux. Experimental studies [77] showed that for the case of a DC magnetic fields of several microteslas, comparable to the earth's magnetic field, the flux is completely trapped. Recent studies [78] support this observation and show that at least the majority of the external flux is trapped in niobium prepared for superconducting cavities. A simplified model gives a quantitative relation for the fluxon induced residual resistance $R_{\mathrm{res,fl}}$ [16]

$$R_{\mathrm{res,fl}} = \frac{B_{\mathrm{ext}}}{2B_{\mathrm{c2}}} R_{\mathrm{N}}, \tag{2.29}$$

where R_{N} is the normal conducting surface resistance, while B_{ext} and B_{c2} are the external and the upper critical field, respectively. According to this equation the contribution of trapped flux to the residual resistance scales with $\sqrt{f}$, normal skin effect is assumed. Equation 2.29 was derived under the assumption that the RF currents pass through the fluxoids. There is also the possibility that the RF currents pass around them. In [13] the two-fluid model is used to derive an expression for $R_{\mathrm{res,fl}}$ considering RF currents passing also around the normal conducting fluxoid, which is usually energetically favorable. Furthermore, it has been shown that the contribution of trapped flux to the surface resistance can also depend on the RF field strength [62].

Another residual loss mechanism originates from hydrogen dissolved in the material [79]. This so called "Q-disease" is usually only observed for cavities of high purity material. It can be suppressed by sufficiently fast cool down (no formation of harmful Nb-H phases) or by hydrogen outgasing at a temperature of about 800 °C [80].

2.4. Maximum RF Field

In the presence of a magnetic field the phase transition between the superconducting and the normal conducting state is of first order. Characteristic for such abrupt phase transitions is the existence of a metastable equilibrium region in the vicinity between the two phases [81].

2.4.1. Bean Livingston Barrier

A metastable state of a type II superconductor has first been investigated by Bean and Livingston in 1965 [82] within the London theory [51]. They considered a flux thread within a semi-infinite type-II superconductor, lying parallel to its surface. Two forces act on this flux thread near the interface between the superconductor and the adjacent vacuum. The magnetic field needs to be parallel to the surface of the superconductor. To obey this boundary condition an image flux is introduced. The interaction between this image flux and the flux thread inside the material yields a force attracting to the surface [83] and the energy U of the flux thread increases with x by:

$$U(x) = \left(\frac{\Phi_0}{4\pi\lambda}\right)^2 K_0(2x/\lambda), \tag{2.30}$$

where K_0 is the modified Bessel function of second kind and $\Phi_0{=}h/2e$ is the flux quantum. For large values of x, far away from the surface the image force vanishes since $K_0(2x/\lambda)$ decays with $\mathrm{e}^{-2x/\lambda}$. An external field of magnitude H penetrating the superconductor gives rise to a surface current which creates a repulsive force perpendicular to the flux thread and the surface current. The interaction energy between H and the flux thread is derived by an integration of the total energy of the superposed fields and currents [82]

$$U(x) = \frac{\Phi_0 H e^{-x/\lambda}}{4\pi}. \tag{2.31}$$

The total energy thus reads:

$$U(x) = \epsilon - \left(\frac{\Phi_0}{4\pi\lambda}\right)^2 K_0(2x/\lambda) + \frac{\Phi_0 H e^{-x/\lambda}}{4\pi}, \tag{2.32}$$

where ϵ is the energy of a single flux thread far away from the surface:

$$\epsilon = \left(\frac{\Phi_0}{4\pi\lambda}\right)^2 \ln(\frac{\lambda}{\xi}) = \frac{\Phi_0 H_{c1}}{4\pi}. \tag{2.33}$$

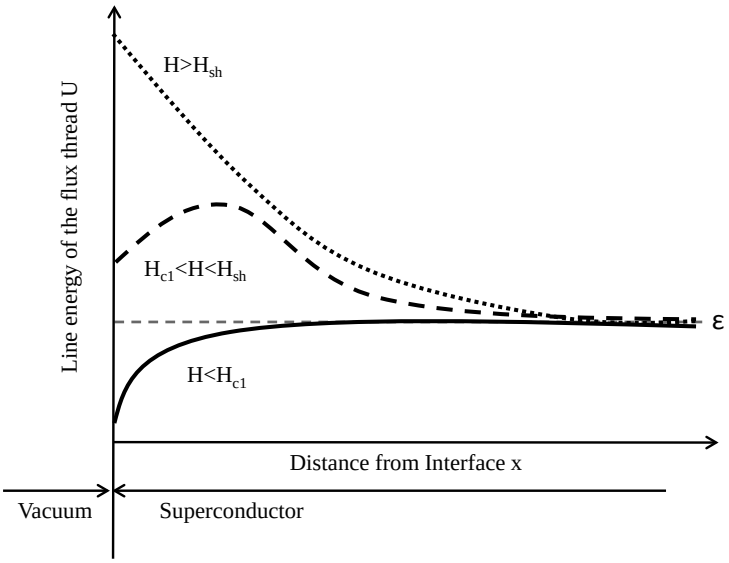

Figure 2.4.: Dependence of the line energy U on distance to the surface x of a flux thread located at the interface between a superconductor and vacuum . When $H < H_{c1}$ the force on the flux thread always points towards the surface. It cannot enter the superconductor (solid line). When $H_{c1} < H < H_{sh}$ it is energetically favorable for the flux thread to be located inside the superconductor. But there is a surface barrier, preventing the entry of the flux thread if the surface is clean (dashed line). When $H > H_{sh}$, the barrier disappears (dotted line) and the force on the flux thread is directed to the inside.

Using 2.33 on 2.32 gives

$$\frac{U(x)}{\epsilon} = 1 - \frac{K_0(2x/\lambda)}{\ln(\lambda/\xi)} + \frac{H}{H_{c1}} e^{-x/\lambda} \tag{2.34}$$

The second term of (2.34) accounts for the force attracting towards the surface. Below H_{c1} this contribution is larger than the third term representing the repulsive part. In this case no flux can enter. If the external field H is larger than H_{c1} it becomes energetically favorable for a flux thread to be located inside the superconductor. If however H is lower than the superheating field H_{sh} the flux thread is unable to enter the superconductor. This is due to a surface barrier, preventing the built up of the thermodynamic equilibrium. When H becomes larger than the superheating field H_{sh} the surface barrier disappears, see Fig. 2.4 [84].

Equation (2.34) is valid only for $\lambda \gg \xi$ and $x \gg \xi$. For $x \approx \xi$ it has to be modified, such that the force attracting to the surface goes smoothly to zero, instead of going to $-\infty$ with K_0 [82]. For this reason Eq. (2.34) cannot be used for a calculation of the onset field for flux entry in niobium. More precise estimates of this barrier field are introduced in the following section.

2.4.2. The Superheating Field Within Ginsburg-Landau Theory

Equation (2.34) gives an intuitive understanding of the phenomenon of superheating. Numerically it is however unsatisfactory for two reasons [85]:

- In the vicinity of the core radius of the flux thread Eq. (2.34) becomes invalid. Especially, when $\lambda \approx \xi$ the results of H_{sh} become dependent on ξ. Therefore the equation is only valid for $\lambda \gg \xi$.
- The density of Cooper Pairs can be reduced near the surface between the superconductor and the vacuum. This is not considered within London theory. Therefore Eq. (2.34) is only valid for $x \gg \xi$.

The problem discussed in the previous section can also be treated within the phenomenological Ginsburg-Landau (GL) theory [86]. For the geometry depicted in Fig. 2.4 the GL-equations can only be solved analytically for the approximations $\kappa \ll 1$ or $\kappa \gg 1$ and give

$$\begin{aligned} H_{\mathrm{sh}} &\approx \frac{0.89}{\kappa} H_{\mathrm{c}}, \quad \kappa \ll 1 \\ H_{\mathrm{sh}} &\approx 0.75 H_{\mathrm{c}}, \quad \kappa \gg 1, \end{aligned} \tag{2.35}$$

where $\kappa = \epsilon_{GL}/\lambda$ is the Ginsburg-Landau parameter. Note that these expressions relate H_{sh} to the thermodynamic critical field H_{c} and not to H_{c1} like Eq. 2.34. For the values of interest concerning accelerator applications, in particular niobium where $\kappa \approx 1$ numerical calculations need to be carried out. Matricon and St. James derived the superheating field as a function of κ in the range between 0 and 2.5 [87]. For $\kappa \approx 1$ they found $H_{sh} \approx 1.2 H_c$. A refined treatment of the superheating field within GL theory can be found in [88]. In this paper approximate formulas for H_{sh}, agreeing within 1.5% with the numerical results are given

$$H_{\mathrm{sh}} \approx H_{\mathrm{c}} \cdot 2^{-1/4} \kappa^{-1/2} \frac{1 + 4.68\kappa + 3.35\kappa^2}{1 + 4.02\kappa + 1.00\kappa^2}, \quad \kappa < 1 \tag{2.36}$$

and

$$H_{\mathrm{sh}} \approx H_{\mathrm{c}} \frac{\sqrt{20}}{6} + \frac{0.3852}{\sqrt{\kappa}}, \quad \kappa > 1. \tag{2.37}$$

The GL theory is valid only near T_{c}, but superconducting cavities are usually not operated at such high temperatures. To derive the correct value of H_{sh} in the low temperature regime one needs to solve the Eilenberger equations [89] instead of the GL-equations. So far this has only been done for large values of κ [90]. The results agree near T_{c} with the Ginsburg-Landau treatment and yield close to 0 K

H_{sh}=0.84H_{c}, a value 10% higher than the Ginsburg-Landau prediction. This result is of great interest, when other superconductors than niobium are considered for accelerating cavities, since materials currently under investigation, such as Nb_3Sn or Mg_2B have larger κ values than niobium.

2.4.3. Critical RF Field From an Energy Balance

The treatment within Ginsburg-Landau or Eilenberger theory assumes that the superconductor can remain in a metastable Meissner state. According to a common misconception in literature there is a strong tendency for a superconductor to remain in a metastable superheated state instead of undergoing a phase transition to the normal state, since the penetration time of fluxoids ($\approx 10^{-6}$ s) was measured to be long compared to the RF period ($\approx 10^{-9}$ s) in the GHz regime [16, 73, 91]. In [92] the time was measured to be between 18 and 28 µs for 0.85 mm of penetration. The penetration speed is therefore between 31 and 47 nm/ns. This means that the time it takes for flux to enter in a depth comparable to the penetration depth is of the same order of magnitude as the RF period[3].

Therefore, one might argue that there is no metastable state and a simple thermodynamic energy balance might give the correct estimation of the maximum RF field. This has first been proposed by Yogi [41] and recently been reconsidered for more recent experimental results by Saito [94, 95]. The argument is simply that a superconductor gains energy by allowing flux to enter within the penetration depth λ. However, if the flux enters, superconductivity will be suppressed within the coherence length ξ. When the energy gained $\propto \lambda H^2$ exceeds the energy lost $\propto \xi H_{\mathrm{c}}^2$ flux will enter and superconductivity vanishes at

$$H_{\mathrm{sh}} = \frac{H_c}{\sqrt{\kappa}}. \tag{2.38}$$

This argument can be extended to different geometries, such as a line. In this case the superheating[4] field reads

$$H_{\mathrm{sh}} = \frac{H_c}{\kappa}. \tag{2.39}$$

Equations 2.38 and 2.39 are the values for the DC case. For the RF case Saito simply states that $H_{\mathrm{sh,RF}} = \sqrt{2} H_{\mathrm{sh,DC}}$ [95].

So far the vortex line nucleation model (VLNM), Eq. (2.39), has given the best

[3] This has been also pointed out by Romanenko in the framework of his investigations of the Q-Drop [93].

[4] This field is denoted here H_{sh}, because in literature it is widely named superheating field. Technically, this term is incorrect for the consideration of a thermodynamic energy balance, since the concept of metastability is not considered here.

agreement to experimental results [95] . The success of this model may be correlated to flux entry at inhomogeneities of a size comparable to ξ and not be the ultimate limit for the critical RF field. In this case advanced surface treatments could enable to overcome this limitation. Equation 2.39 predicts the same value for H_{sh}, where the percolation model (Sec. 2.3.2) predicts the surface resistance to increase exponentially. This might be the reason for the success of the VLNM in explaining experimental results. The cavities become thermally instable, when the surface resistance starts to increase exponentially. In this case the VLNM would not set the ultimate limit for the critical RF field, but the practical limitation (Q-Drop).

The question as to whether a thermodynamic energy balance, like the vortex line nucleation model gives the correct value for H_{sh} becomes especially important, when one thinks of cavities produced of materials other than niobium, since these models give a strong dependence of H_{sh} on κ. At 0 K κ is twice as high as it is close to the transition temperature T_{c} [35], yielding low values for H_{sh} at low temperature, if a thermodynamic energy balance model sets the ultimate limit for the superheating field.

2.4.4. Probing the Maximum RF Field

All theories for the maximum field under RF correlate its value to the Ginsburg-Landau parameter κ. Therefore, when H_{sh} is measured κ should also be derived. This can be done by determining the upper critical field

$$H_{\mathrm{c2}} = \sqrt{2}\kappa H_{\mathrm{c}} \tag{2.40}$$

from magnetization measurements. However, the value derived is the value of the bulk material and not the surface layer penetrated by the RF field. Furthermore, if one wants to obtain κ for the cavity material one either needs to have a reference sample or cut it out of the cavity. Therefore, a method to derive κ by an RF method using the same equipment as for the critical field measurement would be more convenient.

A quantity which can be directly measured in a superconducting cavity and also for the Quadrupole Resonator samples is the penetration depth λ. If one can deduce $\kappa = \lambda/\xi_{\mathrm{GL}}$ directly from λ the obtained value of κ is its value for the layer penetrated by the RF field and not for the bulk material. However, ξ_{GL} cannot be directly determined by an RF method. For accurate calculations it is impossible to use ξ_0 instead of ξ_{GL}. Near 0 K this would only give an error of about 10%, but close to T_{c} ξ_{GL} goes to infinity, while ξ_0 remains finite. The two parameters are derived from different theories. The BCS coherence length can be interpreted as the size of a Cooper Pair, while ξ_{GL} is related to the distance over which the

density of Cooper pairs may vary; $\xi_{\mathrm{GL}}>\xi_0$ always holds [15].

To derive the Ginsburg-Landau parameter from the penetration depth the fact that the BCS and the Ginsburg-Landau coherence lengths, ξ_0 and ξ_{GL} are both correlated to the flux quantum Φ_0 can be used [35]. This enables to derive

$$\kappa = \frac{\pi}{2\sqrt{3}} \frac{H_{\mathrm{c}}(0)}{H_{\mathrm{c}}(T)} \frac{\lambda_L}{\lambda(T,l)}. \tag{2.41}$$

Using the empiric temperature dependence of H_{c} [15]

$$H_{\mathrm{c}}(T) = H_{\mathrm{c}}(0)\left(1 - \left(\frac{T}{T_{\mathrm{c}}}\right)^2\right) \tag{2.42}$$

allows to obtain an expression for the Ginsburg-Landau parameter κ

$$\kappa = \frac{\lambda(T,l)}{\xi_{\mathrm{GL}}} = \frac{2\sqrt{3}}{\pi} \frac{\lambda(T,l)^2 \cdot (1 - (\frac{T}{T_{\mathrm{c}}})^2)}{\xi_0 \lambda_{\mathrm{L}}}. \tag{2.43}$$

To show how κ depends on temperature T the the Gorter-Casimir expression [50]

$$\lambda(T) = \frac{\lambda(0)}{\sqrt{1 - \left(\frac{T}{T_{\mathrm{c}}}\right)^4}} \tag{2.44}$$

is applied to Eq. (2.43) to yield

$$\kappa = \frac{2\sqrt{3}}{\pi} \frac{\lambda(0,l)^2}{\xi_0 \lambda_{\mathrm{L}} \left(1 + \left(\frac{T}{T_c}\right)^2\right)}. \tag{2.45}$$

The same temperature dependence of κ can also be found in [35]. The Ginsburg-Landau parameter is correlated to the purity of the material. To show this a relation found by Pippard [66]

$$\lambda(l) = \lambda(l \to \infty)\sqrt{1 + \frac{\pi\xi_0}{2l}} \tag{2.46}$$

is applied to Eq. (2.45) to yield

$$\kappa = \frac{2\sqrt{3}}{\pi} \frac{\lambda_{\mathrm{L}} \cdot \sqrt{1 + \frac{\pi\xi_0}{2l}}}{\xi_0 \cdot \left(1 + \left(\frac{T}{T_c}\right)^2\right)}, \tag{2.47}$$

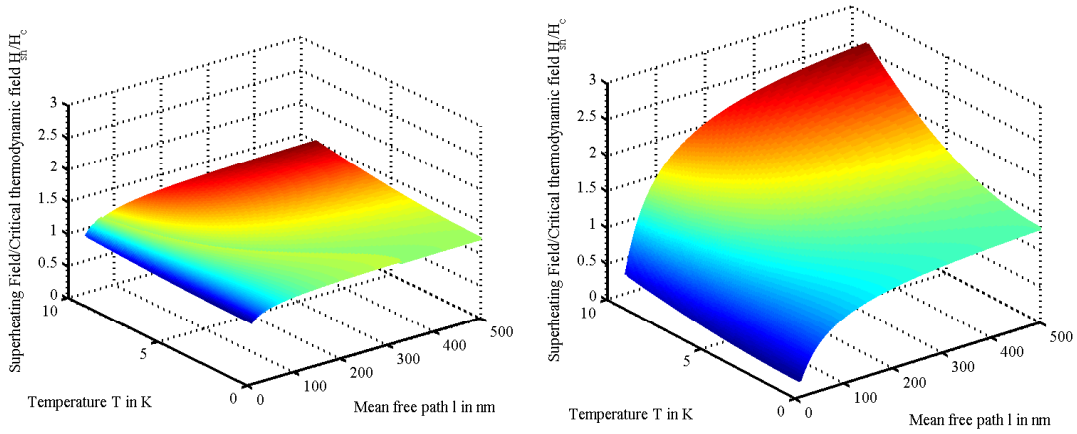

Figure 2.5.: The superheating field of niobium calculated for its prediction from Ginsburg-Landau theory (left) and the vortex line nucleation model (right).

where $\lambda_L = \lambda(0, l \to \infty)$ is the London penetration depth. Equation (2.47) in combination with Eqs. (2.36) and (2.37) allows to calculate the superheating field as predicted from Ginsburg-Landau theory, see Fig. 2.5 (left). If applied to Eq. (2.39) it gives the prediction of the superheating field from the vortex line nucleation model, see Fig. 2.5 (right). For the calculations the values of the material parameters of niobium ξ_0=39 nm, λ_L=32 nm and T_c=9.2 K are taken from the literature [53].

In case of clean surfaces (long mean free path) and low temperatures the Ginsburg-Landau predictions and the VLNM yield similar values for H_{sh}. This is the usual regime of superconducting cavities. Different predictions are found either for high values of κ (short mean free path) or temperatures close to T_c. Both regimes can be conveniently investigated with the Quadrupole Resonator. Samples of low mean free path can be easily manufactured. Since the sample is thermally decoupled from the host cavity the calorimetric technique enables measurements in a helium bath at temperatures above the critical point of helium T=5.19 K [96], where standard cavities need to be operated in gaseous helium.

2.4.5. Thermal Breakdown

Thermal breakdown (quenching) can limit a cavity's performance to a magnetic surface field $H_{max,RF}$ below the intrinsic superheating field. Thermal breakdown occurs at sub-millimeter size areas, having much higher RF losses than the vast part of the superconducting surface. These regions are called defects. In a simple model thermal breakdown is explained by a hemispherical normal conducting heat source of radius a and surface resistance R_N on a superconducting surface cooled

to the bath temperature T_b [97]

$$H_{\mathrm{max,RF}} = \sqrt{\frac{4k(T_\mathrm{c} - T_\mathrm{b})}{aR_\mathrm{N}}}. \tag{2.48}$$

From Eq. (2.48) it is apparent that thermal breakdown can be suppressed by using material with a high thermal conductivity k. For niobium k scales approximately linearly with the residual resistance ratio RRR. Therefore, using high quality niobium can suppress thermal breakdown. Niobium film on copper substrate cavities have the advantage of better thermal conductivity even compared to high purity niobium. These cavities are usually not limited by thermal breakdown but rather by field emission. Equation (2.48) assumes that the breakdown is a complete thermal effect. This has been validated in the past [98]. Recent studies show a more complex picture, where the quench is triggered by an interplay of thermal and magnetic effects [99].

2.5. Summary

In this section the two fluid model has been deduced from Maxwell's equations and London theory. It can predict the dependence of surface resistance of a superconductor on temperature and frequency. Corrections from the microscopic BCS were introduced and analytical formulas allowing for convenient comparison with experimental results were presented. The two fluid model and the BCS theory, however, cannot explain a field dependent nor a residual resistance. The origin of these losses and their relation to the external parameters frequency, temperature, magnetic and electric field are open questions. Several models proposed in the literature have been reviewed. A final assessment of their correctness and applicability can only come from experimental studies. There, one would ideally like to alter the external parameters independently, while investigating the same surface.

Ultimately, the performance of superconducting cavities is limited by the critical RF magnetic field $B_{\mathrm{crti,RF}}$. In order to test whether $B_{\mathrm{crti,RF}}$ is defined by a thermodynamic energy balance or a metastable superheating field requires to determine the Ginsburg-Landau parameter κ for the same surface and temperature. For this purpose an expression correlating κ to the conveniently measurable penetration depth and other material parameters for which literature values are available has been worked out.

3. The Quadrupole Resonator

In this chapter the Quadrupole Resonator at CERN is described. It is a four-wire transmission line half-wave resonator using a TE_{21}-like mode. It was constructed in 1997 to measure the surface resistance of niobium film samples at 400 MHz, the technology and RF frequency chosen for the LHC. The design considerations, which resulted in tits mechanical layout and the applied RF-DC compensation technique, are reviewed here.

The models for the field dependent surface resistance R_S introduced in Chap. 2 predict different correlations of R_S to frequency, temperature and applied field strength. Therefore, possibilities and constraints for extending the Quadrupole Resonator's measurement range to 800 and 1200 MHz are examined. Finally, the interface tunnel exchange model correlates the field dependent surface resistance not to the magnetic but to the electric field. It is shown how the frequency dependent ratio between peak magnetic and electric field on the sample surface of the Quadrupole Resonator can be used to determine which of these fields is responsible for a measured RF dissipation.

3.1. From Basic Design Ideas to the Mechanical Layout

Basic Design Ideas In order to investigate cylindrical superconducting samples a first design idea was to expose the sample surface to the magnetic field of a resonant ring, see Fig. 3.1 (left). The biggest drawback of this approach is the fact that the circumference d of such a ring needs to equal one wavelength λ_w:

$$\lambda_w = d = \frac{c}{f}, \tag{3.1}$$

where f is the frequency of interest and c the speed of light in vacuum. For f=400 MHz the radius of the resonant ring needs to be an impractically large value of 239 mm.

A second idea was to use the magnetic field of two wires, short circuited at two parallel perfect conducting planes at a distance of $\lambda_w/2$, see Fig. 3.1 (middle). In this setup the sample size is independent of resonance frequency. The problem

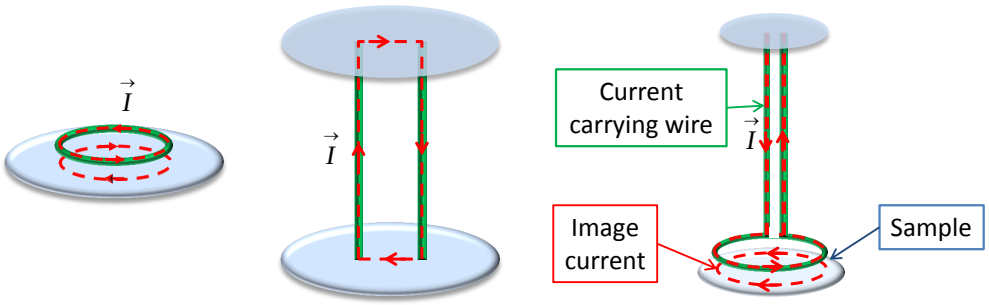

Figure 3.1.: Basic design ideas, which resulted in the construction of the Quadrupole Resonator. A superconducting sample exposed to the magnetic field of a resonant ring (left). Using two wires, short circuited at two parallel perfect conducting planes would overcome the need for impractical large samples (middle). The problem of fixing the wires to the sample surface can be overcome by bending them above the sample surface (right).

of such a device is how to integrate a sample into one of the perfect electrical conducting planes, where the magnetic field is at maximum. The solution found was instead of directly short circuiting one of the resonator ends, to bend it to a ring illuminating the sample surface, see Fig 3.1 (right).

The remaining task then was how to attach the sample. This can be done by connecting a flat sample disk to a cylinder. This cylinder is then attached to the resonator in a coaxial structure, whose inner and outer conductor are the sample cylinder and the wall of the resonator respectively, see Fig. 3.2. The dimensions of this coaxial structure need to ensure that the fields in the gap between sample cylinder and resonator are exponentially decaying (cut-off). This is very important for accurate measurements since losses inside this structure would mean a perturbation to the obtained results. A further improvement was made by adding a second two-wire transmission line in the cavity, see Fig. 3.2 (right). Now the resonator can be excited in a quadrupole mode. The advantage is that this mode has a cut-off frequency twice as high as the dipole mode [100].

Mechanical Design From these basic design ideas the Quadrupole Resonator was developed and constructed. Figure 3.3 shows a photograph and a technical drawing of the device. Its 2 mm thick niobium screening cylinder (⌀=210 mm height=361 mm) is composed of two separate niobium cans, which are electron beam welded alongside and vacuum brazed to stainless steel flanges. This design enables convenient handling of the resonator (efficient cleaning, optical inspection). The two flanges of the screening cylinder are positioned at about $\lambda_w/4$ where the screening current of the Quadrupole Resonator vanishes, if excited at the design frequency of 400 MHz.

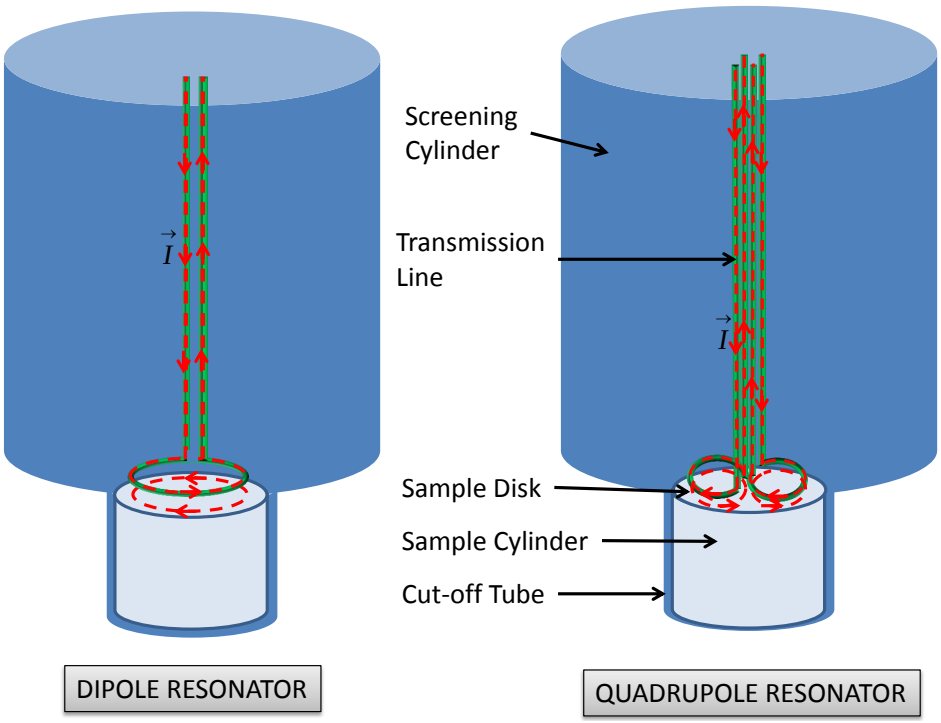

Figure 3.2.: Left: Dipole Resonator. Right: Quadrupole Resonator.

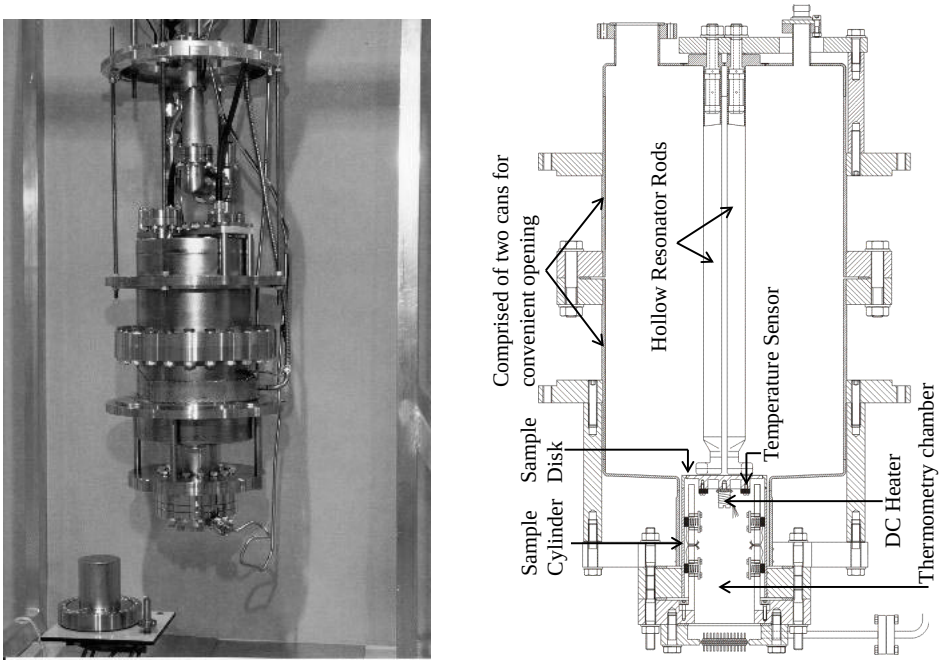

Figure 3.3.: Left: Photograph of the Quadrupole Resonator, an additional sample and an antenna. Right: Technical drawing of the device [30]

The four-wire transmission line is built from niobium rods (⌀ 16 mm) welded to the upper cover plate of the resonator. For cooling purposes the rods are hollow to allow liquid helium (LHe) to flow inside. At the bottom end these rods are bent to form half rings of 25 mm radius. The RF current of the resulting loop creates an image current on the front disk of the sample (⌀ 75 mm) positioned 1 mm below the niobium half rings. This distance can be derived by measuring different resonant modes of the Quadrupole Resonator at room temperature. The sample cylinder is fixed to a 6 inch Conflat flange and mounted into a tubular port of 2 mm bigger radius and equal length to ensure that the sample surface is flush with the lower cover plate of the niobium cylinder to which the port is welded [30]. Regarding the niobium rods as conductors of a screened four-wire transmission line excited in its quadrupole mode, the apparatus was named Quadrupole Resonator [30].

A resistor for DC heating and six calibrated silicon diodes are placed inside the thermometry chamber. Four of the diodes are directly placed below the position of maximum magnetic field on the sample disk, while two of them are pressed by a piston to the inner wall of the sample cylinder. These two diodes are therefore at a position of lower temperature. This allows to derive the thermal conductivity if disk and cylinder are made of the same material.

Magnetic Shielding For the studies carried out in the framework of this thesis the cryostat of the Quadrupole Resonator has been equipped with coils to cancel out the earth's magnetic field. This is necessary to avoid losses from trapped flux, see Sec. 2.3.4. The current applied to the compensation coils has been adjusted to minimize the residual magnetic field at the position of the sample. The field was measured with a fluxgate magnetometer and could be suppressed to a value below 1 μT.

3.2. Resonant Modes

Simulations performed with CST Microwave Studio® show that multiple integers of the Quadrupole Resonator's fundamental mode frequency of 400 MHz are also resonant in the device, as expected for a half-wave resonator, see Fig. 3.4. This was validated by measuring the resonant frequencies using a network analyzer. Besides the quadrupole modes at 400, 800 and 1200 MHz, there are also monopole and dipole modes found. All the Q-values have been calculated using Eq. (1.1) and the definition of the normal conducting surface resistance in the normal skin effect:

$$R_{\mathrm{N}} = \sqrt{\frac{\pi f \mu_0}{\sigma_0}}, \tag{3.2}$$

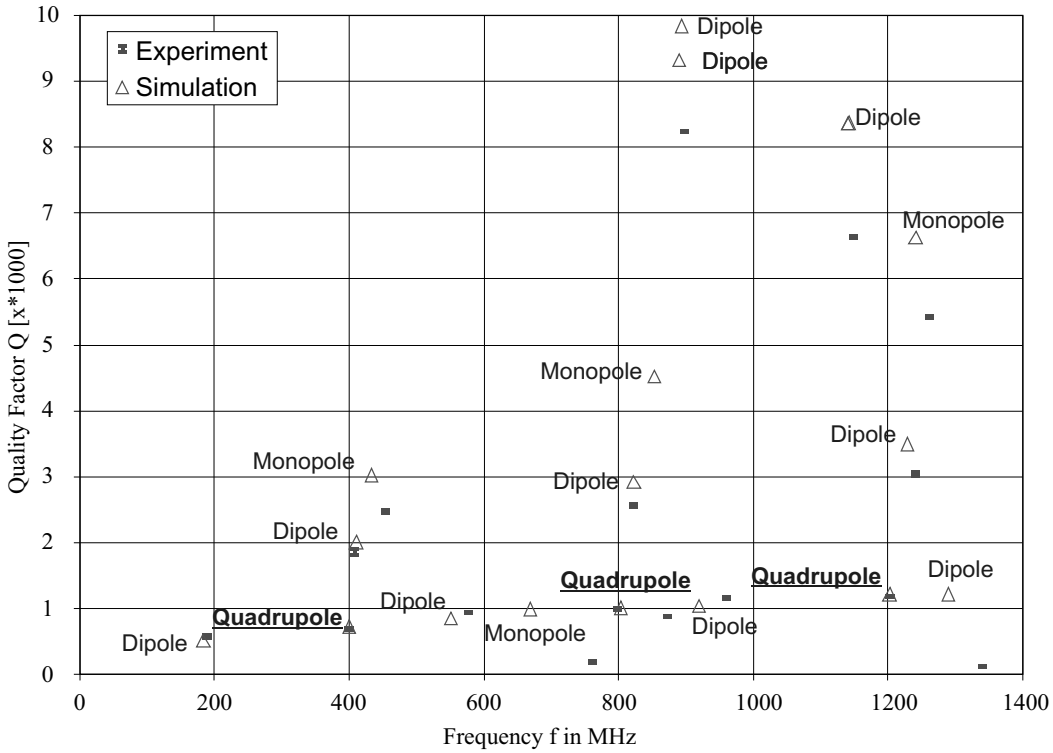

Figure 3.4.: Q-values of resonant modes at room temperature found in the Quadrupole Resonator.

where the value of the conductivity at room temperature for niobium σ_0=6.58 · $10^6\,(\Omega\mathrm{m})^{-1}$ is taken from literature [7]. For all quadrupole modes and the two dipole modes of lowest resonant frequencies simulation and measurement results agree within 5 % regarding Q-value and frequency. All the other dipole modes are in agreement within 5 % regarding the resonant frequency f. The maximum difference between simulation and measurement is 50 MHz for the dipole mode of highest frequency. In the Quadrupole Resonator the cover plate of a cylinder attached to the cavity in a coaxial structure serves as sample, see Fig. 3.3. For the Quadrupole mode at 400 MHz this design yields exponentially decaying RF fields between the outer wall of the sample cylinder and the host cavity. Therefore, the power dissipated inside this 1 mm gap and especially at the end flange and joint of the sample cylinder is negligible. Additionally to the 400 MHz design mode the fields are also exponentially decaying for all other excitable quadrupole (TE_{21}-like) modes up to 2.0 GHz and for all dipole (TE_{11}-like) modes below 1 GHz. This can also be shown by analytical calculations [101].

The Q-value of all other modes is systematically higher for the simulated values, due to the fact that all these modes have high field values in this gap. Therefore,

possible losses due to leakage of RF fields at the flange where the sample cylinder is attached to the cavity could not be accurately calculated due to the limited spatial resolution of the simulation model. The simulation predicts two dipole modes at 890 and 894 MHz with different field configurations and Q-values. At room temperature these two modes cannot be separately resolved; only one resonance at 897 MHz was measured. The monopole modes show the highest disagreement between measured and simulated values for resonant frequency and Q-value. These modes are not in cut-off inside the coaxial structure between cavity and sample cylinder and have the highest field values in this gap and on the cover where the niobium rods are mounted to the cavity. No further investigations on the monopole and dipole modes have been performed, since they are not usable for investigations of the samples. It is only important to know resonant frequency and field configuration of these modes in order to avoid their simultaneous excitation with a Quadrupole mode used for sample characterization.

In principal five Quadrupole modes could be excited and used for RF measurements. At CERN equipment for 400, 800 and 1200 MHz is available for the Quadrupole Resonator test stand. Note that RF equipment such as amplifiers or circulators is usually narrow band. To perform tests at the three frequencies two different pre-amplifiers (each 5 W, one covering the range up to 500 MHz, the other one the range between 700 and 2200 MHz) and three different main amplifiers (500 W for 400 MHz and 200 W for 800 MHz and 1200 MHz) are used. For each frequency a dedicated circulator is needed. The rest of the used RF equipment covers the whole frequency range.

Operation at 800 MHz The Quadrupole Resonator consists of two 2 mm thick niobium cans for convenient handling and cleaning of the device, see Fig. 3.3 (right). These cans are flanged to each other in the middle of the resonator, where the screening current on the cavity surface vanishes for the modes at 400 and 1200 MHz. For the 800 MHz mode the screening current has a maximum at this position. Since the field is strongly concentrated around the rods in the middle of the resonator, excitation and measurements at 800 MHz are not perturbed by losses at this flange. They are so low that the system remains strongly overcoupled at fields up to the highest level reached, which is 40 mT at 800 MHz. The magnetic field at the flange between the upper and the lower can is only 0.5 % of the maximum field on the sample as has been calculated by Microwave Studio.

3.3. The RF-DC Compensation Technique

The Quadrupole Resonator allows to measure the surface resistance of the samples attached by an *RF-DC compensation technique*. Compared to the *end-plate replacement* or the *thermometric technique*, this approach has the advantage of high sensitivity and independence of a reference sample, see Sec. 1.2. The drawbacks are a usually more complicated design and the fact that the measurement temperature always needs to be higher than the bath temperature.

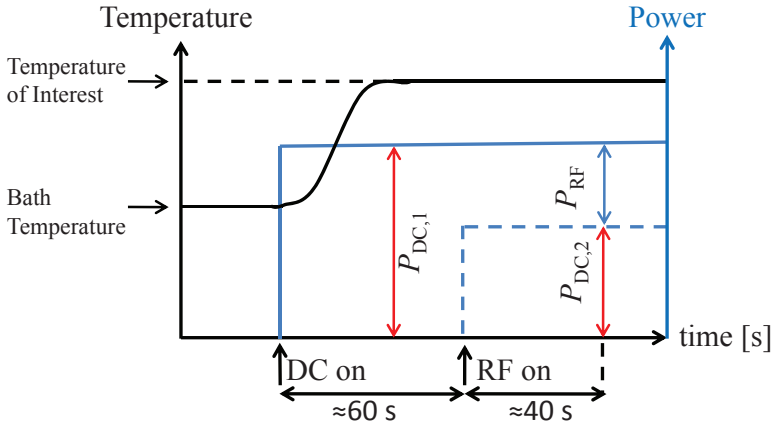

Figure 3.5.: In a calorimetric system the surface resistance of a superconducting sample is derived from a DC measurement.

A calorimetric measurement consists of two steps, see Fig. 3.5:

1. The temperature of interest is set by applying a current to the resistor on the back side of the sample. The power dissipated $P_{\mathrm{DC},1}$ is derived from measuring the voltage across the resistor.

2. The RF is switched on and the current applied to the resistor is lowered to keep the sample temperature and the total power dissipated constant.

The power dissipated by RF, P_{RF} is the difference between the DC power applied without RF, P_{DC1} and the DC power applied with RF, P_{DC2}. P_{RF} is directly related to the surface resistance of the sample R_{S} and the magnetic field on the sample surface $\vec{B}$,

$$P_{\mathrm{RF}} = P_{\mathrm{DC1}} - P_{\mathrm{DC2}} = \frac{1}{2\mu_0^2} \int_{\mathrm{Sample}} R_{\mathrm{S}} |\vec{B}|^2 \mathrm{d}S. \tag{3.3}$$

Assuming R_{S} to be constant over the sample surface area and independent of $\vec{B}$,

Eq. (3.3) simplifies to

$$P_{\mathrm{RF}} = P_{\mathrm{DC1}} - P_{\mathrm{DC2}} \approx \frac{1}{2\mu_0^2} R_{\mathrm{S}} \int\limits_{\mathrm{Sample}} |\vec{B}|^2 \mathrm{d}S, \tag{3.4}$$

which can be rearranged to yield an expression for the surface resistance:

$$R_{\mathrm{S}} = \frac{2\mu_0^2 (P_{\mathrm{DC1}} - P_{\mathrm{DC2}})}{\int\limits_{\mathrm{Sample}} |\vec{B}|^2 \mathrm{d}S}. \tag{3.5}$$

A constant c_1 relating the peak magnetic field on the sample surface B_{p} to its integrated value over the sample surface can be introduced and calculated numerically for a given mode

$$c_1 = \frac{B_{\mathrm{p}}^2}{\int\limits_{\mathrm{Sample}} |\vec{B}|^2 \mathrm{d}S}. \tag{3.6}$$

To derive B_{p} from an RF measurement a second constant c_2, relating B_{p}^2 to the stored energy in the cavity U is introduced. Its value must also be calculated numerically,

$$c_2 = \frac{B_{\mathrm{p}}^2}{U}. \tag{3.7}$$

The loaded quality factor Q_{L} of a cavity equals

$$Q_{\mathrm{L}} = \frac{\omega U}{P_{\mathrm{L}}} = \omega \tau, \tag{3.8}$$

where the loaded power P_{L} is the power dissipated in the cavity and radiated into the couplers, while τ is the corresponding decay time. Inserting (3.7) in (3.8) yields

$$B_{\mathrm{p}} = \sqrt{\mathrm{c}_2 \tau P_{\mathrm{L}}}. \tag{3.9}$$

With the constants c_1 and c_2 Eq. (3.5) becomes an expression of constants and measurands:

$$R_{\mathrm{S}} = 2\mu_0^2 c_1 \frac{(P_{\mathrm{DC1}} - P_{\mathrm{DC2}})}{c_2 \tau P_{\mathrm{L}}}. \tag{3.10}$$

In case of non-critical coupling P_{L} must be derived from the forward and the reflected power (P_{f} and P_{r}):

$$P_{\mathrm{L}} = 2P_{\mathrm{f}} \mp \sqrt{P_{\mathrm{r}} P_{\mathrm{f}}}, \tag{3.11}$$

with minus/plus for an under/over coupled input antenna. To derive P_{L} from only

one measurement the Quadrupole Resonator uses a fixed coupling. The device is equipped with two strongly overcoupled loop-antennas (coupling factor about 100 each). The resonator acts like a narrow band filter. Only a negligible amount of the power coupled in is dissipated in the resonator walls. Since the coupling geometries of the input and the output antenna to the resonator are identical, the coupling factor as seen from the input coupler is $\beta = 1$ (critical coupling, no power is reflected). The assumption that the forward power P_f equals the transmitted power P_t can be made. This allows to approximate $P_\mathrm{L} = 2P_\mathrm{f} = 2P_\mathrm{t}$. A third weakly coupled loop-antenna of same geometry but located at a position of lower field serves as pick-up probe to measure P_t.

Furthermore, the geometry factor of the sample G_Sample is introduced. It is defined in the same sense as for accelerating cavities by Eq. (1.2), but considers only losses on the sample surface. Therefore campared to Eq. (1.2) the unloaded quality factor of the cavity Q_0 is replaced by the quality factor of the sample Q_Sample:

$$G_\mathrm{Sample} = R_\mathrm{S} Q_\mathrm{Sample} = \mu_0^2 \frac{2\omega U}{\int\limits_\mathrm{Sample} |\vec{B}|^2 \mathrm{d}S} \tag{3.12}$$

Using the definitions of c_1 (Eq. (3.6)) and c_2 (Eq. (3.7)) G_Sample can be written as

$$G_\mathrm{Sample} = 2\omega\mu_0^2 \frac{c_1}{c_2} \tag{3.13}$$

allowing to express the surface resistance as:

$$R_\mathrm{S} = G_\mathrm{Sample} \frac{(P_\mathrm{DC1} - P_\mathrm{DC2})}{\omega\tau P_\mathrm{L}}. \tag{3.14}$$

The constants c_1, c_2 and G were derived by two different computer codes. CST Microwave Studio® (MWS) [102] is based on the finite integral technique. For the simulation of resonant structures the Eigenmode Solver is best suited. The symmetry of the field configuration allowed to simulate only one fourth of the structure, see Fig. 3.6. After several refinements, especially in the gap between sample and crooked endings of the resonator rods, the simulation model was approximated by almost 2 million hexahedrales. It was solved with a standard PC. Ansoft HFSS® [103] is based on the finite element method. The program approximates the simulation model by a tetrahedral mesh, including curved etches. For highly resonant structures HFSS comprises an Eigenmode Solver like MWS. The maximum amount of usuable mesh-cells is lower compared to MWS, but the tetrahedral mesh allows a much better approximation of the simulation model, compared to a hexahedral mesh, especially when curved elements are used. The biggest challenge in simulating the Quadrupole Resonator was to find a mesh, which is very fine in the 1 mm

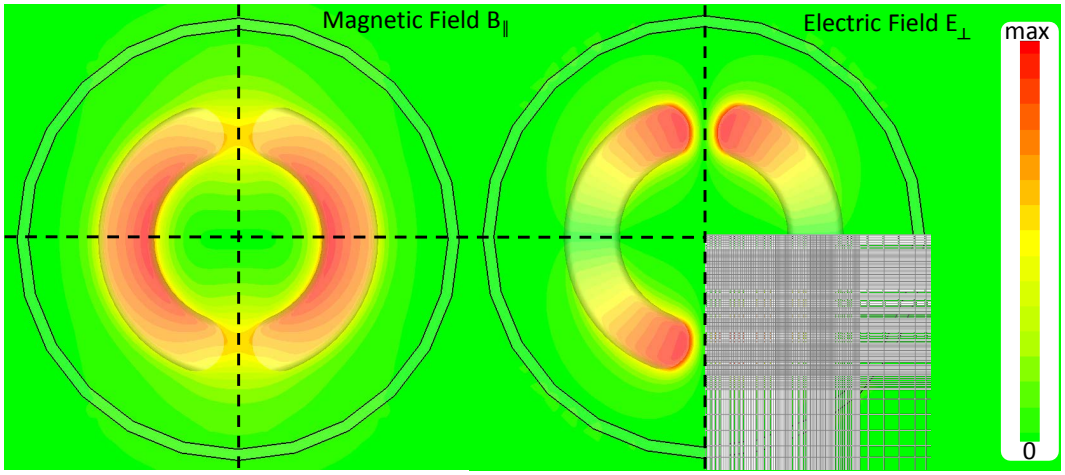

Figure 3.6.: Magnetic (left) and electric (right) field distribution at 400 MHz on the sample surface calculated with Microwave Studio. The fields are highly concentrated around the crooked endings of the resonator rods. The symmetry of the field configuration, indicated by the dashed lines, allowed calculating only one fourth of the structure. On the bottom right the mesh used to approximate the geometry is displayed.

gap between sample and crooked endings of the resonator rods. The hexahedral mesh used by MWS, allowing for more mesh cells, was found to be more effective for this task. Therefore in the following the parameters derived from Microwave Studio will be used. The values of agree within 6 % with the values derived using HFSS, see Tab. 3.1.

Table 3.1.: Field parameters of the Quadrupole Resonator calculated with CST Microwave Studio/Ansoft HFSS

f in MHz	c_1 in m^{-2}	c_2 in T^2/J	G_{Sample}
399.6/399.4	1408/1431	0.105/0.104	106.3/109.1
803.1/803.2	1403/1488	0.105/0.105	212.9/225.9
1211.1/1208.8	1569/1540	0.121/0.116	311.6/318.5

Pulsed Operation Measurements are performed in continuous wave (CW) operation if possible. At relative high fields, low temperature and/or high surface resistance however, the power dissipated by RF may yield a sample temperature above the temperature of interest. In this case the RF signal has to be modulated in amplitude with a rectangular pulse and for P_L one has to take the average power over one pulse including the part where the RF is off. Its measurement can be performed with a spectrum analyzer. Additional error sources occur in pulsed

operation. The Q-value of the Quadrupole resonator is approx. 10^6 corresponding to a decay time τ of a few 100 microseconds, depending on frequency. During this time the field applied is not at its maximum. So if the surface resistance increases with field and the rise time is not short compared to the pulse length, the surface resistance will be underestimated. On the other hand the pulse length may not be too long, otherwise a steady increase and decrease of the sample temperature will occur, diminishing stable temperature control. A modulation frequency of 20 Hz was found to be a good compromise. Duty cycles between 10 and 50 % corresponding to a pulse length between 5 and 25 ms, were used for surface resistance measurements. To probe the critical RF fields even shorter pulses of about 1 ms length were applied.

3.4. Electric and Magnetic Field Configuration

Cylindrical cavities operated in a TE mode are often used for material characterization. These cavities expose the samples attached only to an RF magnetic field. The Quadrupole Resonator with its different field configuration exposes the samples to electric and magnetic fields simultaneously.

The electrical field $\vec{E}$ on the Quadrupole Resonator sample surface scales linearly with frequency for a given magnetic field $\vec{B}$, as required by the law of induction when applied to the geometry in between the crooked endings of the rods and the sample. For a peak magnetic field B_p=10 mT, the peak electric field is E_p =0.52, 1.04 and 1.56 MV/m for 400, 800 and 1200 MHz, respectively. These values are small compared to E_p-field levels on elliptical cavities, but the area of high electric field is larger. In elliptical cavities excited in the TM_{010}-mode the surface electric field is mainly concentrated around the iris of the cavity. In the Quadrupole Resonator it is approximately spread over the same area on the sample surface as the magnetic field, see Fig. 3.6. The fact that the ratio of the mean values $E_\mathrm{mean}/B_\mathrm{mean}$ for elliptical cavities and the Quadrupole Resonator are comparable is a valuable feature for the latter if real accelerator cavity surfaces are to be studied. Analogous to Eq. (3.14) one can define the electrical surface resistance R_S^E [52]:

$$R_\mathrm{S}^\mathrm{E} = G_\mathrm{Sample}^\mathrm{E} \frac{(P_\mathrm{DC1} - P_\mathrm{DC2})}{\omega \tau P_\mathrm{L}}, \tag{3.15}$$

with the definition of the electric geometry factor:

$$G_\mathrm{Sample}^\mathrm{E} = \frac{\mu_0}{\varepsilon_0} \frac{2\omega U}{\int\limits_\mathrm{Sample} |\vec{E}|^2 \mathrm{d}S}. \tag{3.16}$$

To relate electric and magnetic losses to each other the constant c_3 is introduced

$$c_3 = \frac{G^{\mathrm{E}}_{\mathrm{Sample}}}{G_{\mathrm{Sample}}} \tag{3.17}$$

The ratio between the magnetic and the electric geometry factor scales quadratically with frequency. This follows directly from the law of induction for the Quadrupole Resonator geometry and has been verified with an agreement better than 1% using MWS. This allows to normalize c_3 to 400 MHz

$$c_3^{400} = \frac{G^{\mathrm{E}}_{\mathrm{Sample}}}{G_{\mathrm{Sample}}} \frac{(400\,\mathrm{MHz})^2}{f^2}. \tag{3.18}$$

Calculated by MWS c_3^{400}=53.5 is found. Equation (3.18) applied to Eq. (3.15) yields

$$R^{\mathrm{E}}_{\mathrm{S}} = \frac{c_3^{400} \cdot (400\,\mathrm{MHz})^2}{f^2} G_{\mathrm{Sample}} \frac{(P_{\mathrm{DC1}} - P_{\mathrm{DC2}})}{\omega\tau P_{\mathrm{L}}} = \frac{c_3^{400} \cdot (400\,\mathrm{MHz})^2}{f^2} R_{\mathrm{S}}. \tag{3.19}$$

This implies that a power dissipated by the RF field on the sample surface P_{RF} corresponding to a magnetic surface resistance of 1 nΩ is equivalent to an electric surface resistance of 53.5 nΩ at 400 MHz. At 800 MHz an RF heating corresponding to R_{S}=1 nΩ is equivalent only to $R^{\mathrm{E}}_{\mathrm{S}}$=13.4 nΩ.

With the Quadrupole Resonator it is impossible to measure magnetic and electric losses independently. Therefore, if not explicitly stated the surface resistance will always be calculated as the magnetic surface resistance. In case losses are caused by an electric field, R_{S} must be understood as the equivalent magnetic surface resistance, which would yield the same losses if the surface resistance would be caused by the magnetic field. In the following when data is fitted to a model including electric losses, these contributions will be converted to the equivalent magnetic surface resistance, using Eq. (3.19). This approach allows to display data comprising magnetic and electric surface resistances in the same graph.

3.5. The RF Control System

The key components of the Quadrupole Resonator's RF control system are displayed in Fig. 3.7. Underlined words in the following text indicate a component displayed in this figure. There and throughout this section the Quadrupole Resonator is only referred to as resonator.

The RF input signal is controlled by a synthesizer, to which a function generator is attached. The function generator sends a periodic rectangular voltage of a few

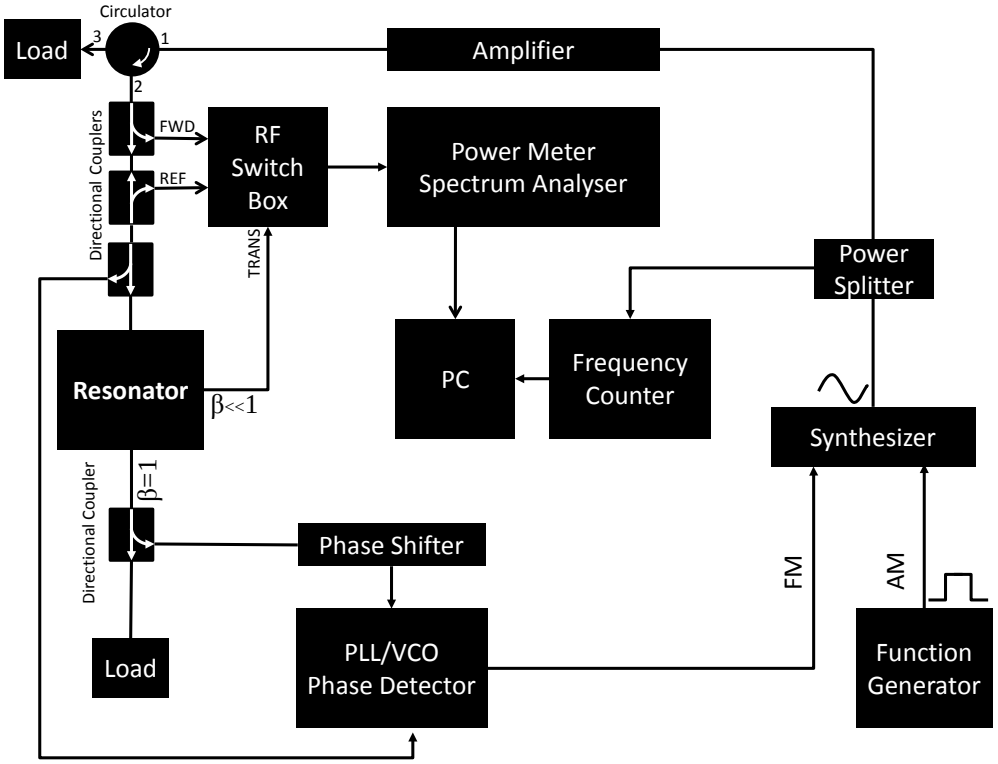

Figure 3.7.: The RF system of the Quadrupole Resonator.

Hz to the synthesizer. The synthesizer now multiplies the rectangular pulse with the RF sine wave of 400, 800 or 1200 MHz to create the output signal (Amplitude Modulation, AM). The function generator enables to set the duty factor of the output signal. For continuous wave (CW) measurements the AM is simply disabled by the internal settings of the synthesizer.

Only in CW operation the frequency counter attached to the synthesizer via a power splitter enables to measure the RF output frequency. The modulated signal is amplified before transferred to the resonator, which is equipped with two output antennas: one is critically coupled to the input antenna (β=1), the other one is strongly undercoupled ($\beta \ll 1$). The resonator itself is strongly overcoupled. The measurement technique relies on the assumptions that the energy, which is coupled in is completely coupled out, see Sec. 3.3. In this picture one may regard the resonator as a filter of narrow bandwidth. The strongly coupled antenna has two purposes. It provides the critical coupling between input and output and enables the closed loop operation as described below. The weakly coupled antenna is used for the measurement of the transmitted power directly related to the electromagnetic fields stored in the resonator. As one can see in Fig. 3.7 its signal is directly transferred to an RF switch box (so are attenuated signals

of the forwarded and the reflected wave). The RF switch box enables to choose which of the signals one wants to measure with the attached power meter and spectrum analyzer.

Three directional couplers are placed between the cavity and the circulator. One is coupling to the reflected; two of them are coupling to the forward signal. A fourth directional coupler is placed behind the strongly coupled output. The majority of the power coupled out is dissipated in a load, while the smaller part is transferred to a phase-locked loop (PLL). The PLL multiplies the transmitted signal with the forward signal. In the time domain the forward voltage can be written as

$$U_{\mathrm{f}}(t) = \hat{U}_{\mathrm{f}} \cos(\omega_{\mathrm{f}} t) \tag{3.20}$$

with an arbitrary phase. The transmitted voltage U_t has not necessarily the same phase as the forward voltage. Therefore, a phase difference φ needs to be taken into account.

$$U_t(f) = \hat{U}_{\mathrm{t}} cos(\omega_{\mathrm{t}} t + \varphi). \tag{3.21}$$

The PLL multiplies U_t with U_f yielding with simple trigonometry

$$U_{\mathrm{out}} = U_{\mathrm{t}} U_{\mathrm{f}} = \frac{1}{2} \hat{U}_{\mathrm{t}} \hat{U}_{\mathrm{f}} \left[\cos((\omega_{\mathrm{f}} - \omega_{\mathrm{t}})t - \varphi) - \cos((\omega_{\mathrm{f}} + \omega_{\mathrm{t}})t + \varphi)\right] \tag{3.22}$$

The second cosine term is of high frequency and is suppressed by an internal low pass filter. The leading cosine term gives an output U_{out} according to the phase and frequency difference of the two signals. If ω_f=ω_t the system is referred to as being locked, U_{out} is only depended on the phase difference φ. This offset needs to be adjusted to a value of approx. $\pi/2$ by a phase shifter connected between the resonator and the PLL to ensure that the system is operating in the regime, where U_{out} depends almost linearly on $\omega_f - \omega_t$. The phase shift between transmitted and forward signal can be measured with a phase detector integrated in the same box as the PLL.

The output of the PLL is connected to the synthesizer, where U_{out} is used for frequency modulation (FM) with the carrier frequency f_{c} to yield the RF output signal. In practice, the resonance frequency of the resonator is measured after cool down using a network analyzer. The derived frequency is taken as f_{c}. Afterwards the phase is adjusted to yield zero reflection. Now the system is locked. Due to variations of the helium pressure, changing of the sample temperature or other disturbances the resonant frequency changes. This yields a non-zero PLL output voltage. The FM now changes the frequency of the synthesizer's output according to

$$\omega_{\mathrm{out}} = \omega_{\mathrm{c}} + K_{\mathrm{m}} \cos((\omega_{\mathrm{f}} - \omega_{\mathrm{t}})t), \tag{3.23}$$

where the modulation constant K_{m} is a measure for the strength of the modulation.

An automatic phase control system has been developed in the framework of this thesis. It maximizes the transmitted power by altering the phase between transmitted and forward power. This programmed phase shifter enables completely automatic measurements of the surface resistance. A LabView® [104] program for surface resistance data acquisition has been written. The penetration depth and the quench fields are manually measured. A second LabView program allows to acquire this data, which is stored and analyzed using a standard PC.

3.6. Performance Discussion

3.6.1. Field Limitations and Excitable Modes

At present, the Quadrupole Resonator is capable of measuring the surface impedance (resistance and penetration depth) and the critical field at 400, 800 and 1200 MHz. The quadrupole modes at 1600 and 2000 MHz could also be used, if all the equipment for measurements at these frequencies would be available. Currently, amplifiers with a power of more than 5 W and circulators are missing for measurements at 1600 and 2000 MHz. It is planned for future experiments to include these modes.

At 400 MHz the highest field level achieved was approx. 60 mT on the sample surface. This corresponds to a maximum field of approx. 70 mT on the rods opposite to the sample surface, which is the maximum field in the whole structure. This value is well below the expected critical RF field of niobium. The quench field is unaffected by the applied RF duty cycle. Even single pulses of one millisecond length do not enable higher field values. When a quench occurs on the sample surface, the sample temperature always rises above T_c. However if the sample is not DC heated and its temperature is identical to the cavity temperature, the quench occurs, while the sample temperature does not rise. In this case the quench is located on the host cavity and not on the sample surface. The fact that the quench field is independent of duty cycle is an indication that it is triggered by a relatively fast process, which could be field emission or multipacting. The surface electric field of the Quadrupole Resonator is at maximum in the middle of the transmission line. For a surface magnetic field on the sample disk of 60 mT the peak electric field on the rods is about 15 MV/m, a field level at which field emission for cavities prepared by buffered chemical polishing (BCP), like the Quadrupole Resonator, might well appear [105, 106]. An additional rinsing with ultrapure water at about 5 bar did not yield a higher field level. Rinsing at higher pressure was not available at CERN during cavity preparation.

A possible diagnostic tool to distinguish between multipacting and field emission would be to implement an X-ray detector to the test stand. While field emission

appears for high electron energies creating X-rays, multipacting appears at relative low impact energies, where no X-rays are created. At 800 MHz no multipacting was observed, while at 1200 MHz multipacting at 15 mT, close to the maximum available amplifier power appeared . This barrier was processable[1], unlike the 60 mT barrier at 400 MHz, which yielded the quench of the cavity.

The quench location could not be detected with oscillating superleak transducers (OSTs) [107]. Detailed investigations of the properties of these detectors have shown that they are sensitive to rather low energy [108] and that a second sound wave can be reflected at a niobium surface [109]. Therefore these sensors should be able to detect the quench even if it would occur on the bottom of the rods, where the magnetic field is at maximum. This is why, further improvements, especially noise reduction, of the OST system are promising for localizing the quench in the Quadrupole Resonator.

3.6.2. Mechanical Vibrations

When the field level is raised the power transmitted can be strongly modulated in amplitude, especially when the 1200 MHz mode is excited. In the worst case these modulations might completely prevent measurements. The following observations have been made, see Fig 3.8:

1. The modulations are most severe at 1200 MHz.
2. The modulation frequency is 69 Hz at 800 and 1200, but not at 400 MHz.
3. The 69 Hz oscillation is observed twice.
4. At 400 MHz a 278 Hz oscillation is dominant. This modulation is a lot less severe.
5. The effect is very strong in normal fluid helium and a lot less pronounced if the resonator is operated in superfluid or subcooled helium.

There are two possible explanations why the 69 Hz oscillation is not observed at 400 MHz. It could either be not excited or canceled out by the feedback system. A fast Fourier transform (FFT) analysis of the PLL feedback signal shows that the 69 Hz peak and its harmonics are dominating the spectrum if the cavity is excited 1200 MHz, see Fig. 3.9 (left). The PLL fails to stabilize the RF signal here. At 400 MHz a wide spectrum is observed. A 69 Hz peak is not found in the spectrum. The two closest ones are found at 63.4 and 72.3 Hz, see Fig. 3.9

[1] Applying a CW RF field slightly below 15 mT for several minutes was sufficient to make the multipacting barrier disappear.

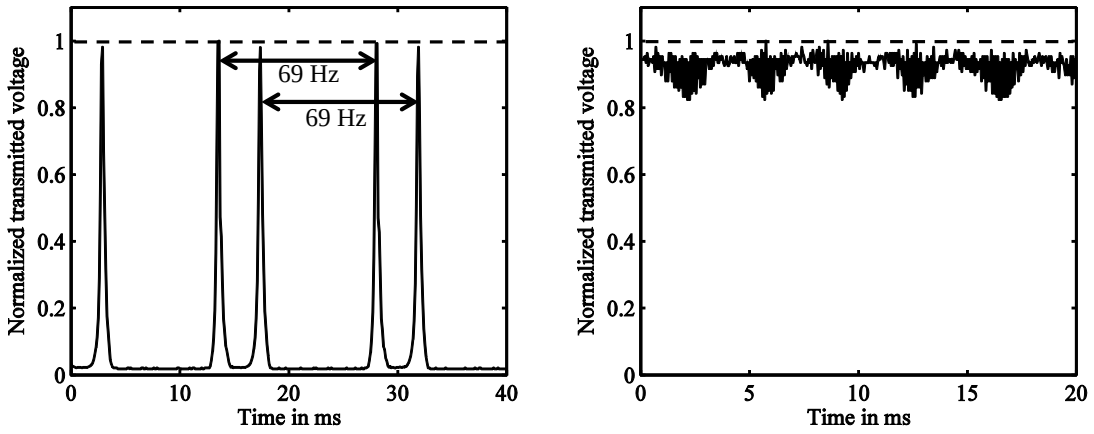

Figure 3.8.: Transmitted voltage at 1200 (left) and 400 MHz (right) measured in a normal fluid helium bath. The maximum voltage corresponds in both cases to a peak field on the sample surface of approx. 15 mT. The dashed lines indicate the transmitted voltage one would measure if no vibrations would perturb the measurement.

(right). Therefore, one can conclude that the 69 Hz oscillation is not excited if the resonator is operated at 400 MHz.

In general, there are two possible causes for the observed oscillations. They could be forced from an external source, for example a vacuum pump, or it could be a resonant phenomenon. Vibrations can be measured by an accelerometer [110]. In order to test if oscillations from an external source are transmitted to the Quadrupole Resonator a piezoelectric accelerometer (Brüel & Kjaer 4507-B-005) was placed outside onto the cryostat. All vibrations transmitted to the resonator should be measurable at this position. The obtained spectrum shows two dominant peaks at 75 and 96 Hz. No peak at 69 Hz was observed, see Fig. 3.10 (left). This indicates that this oscillation is not forced from an outside source. The fact it is not observed if the resonator is excited at 400 MHz is also strong evidence for a resonant phenomenon.

After the resonator was warmed up the accelerometer was mounted on a metal bar. The diameter of the bar was about 2 mm and its length about 500 mm. This bar was inserted inside one of the hollow resonator rods, so that one ending reached the crooked half rings from the inside. To the other ending the accelerometer was fixed. The bar was used to set the rods into vibration. After this excitation was stopped, the bar was kept in contact with the resonator rods. During the excitation a wide frequency spectrum was measured by the accelerometer, but only one peak at 69 Hz was observed after the excitation was stopped, see Fig. 3.10 (right). This shows that the 69 Hz oscillations observed in the RF signals originate from resonant oscillations of the rods. The observation of two 69 Hz oscillations in the RF signal, see Fig. 3.8 (left) is simply due to the fact that there are two rods

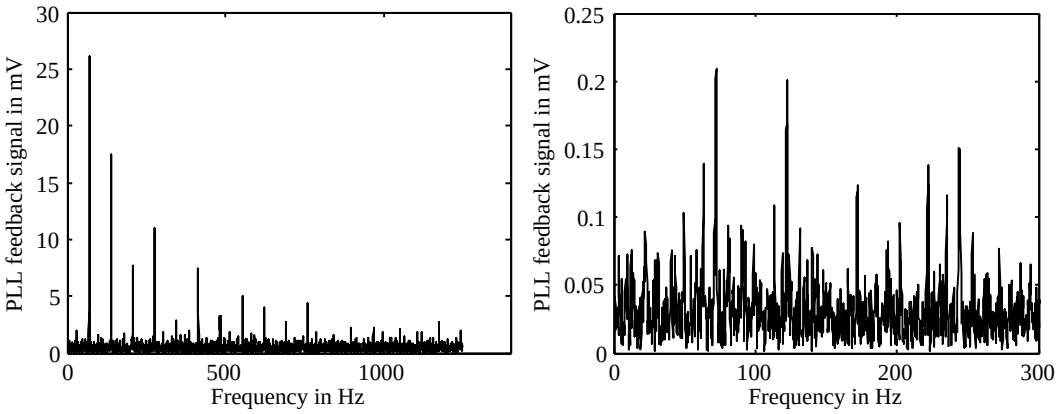

Figure 3.9.: PLL feedback signal measured when the resonator was excited at 1200 (left) and 400 MHz (right) in a normal fluid helium bath. The corresponding transmitted power for both signals are displayed in Fig 3.8

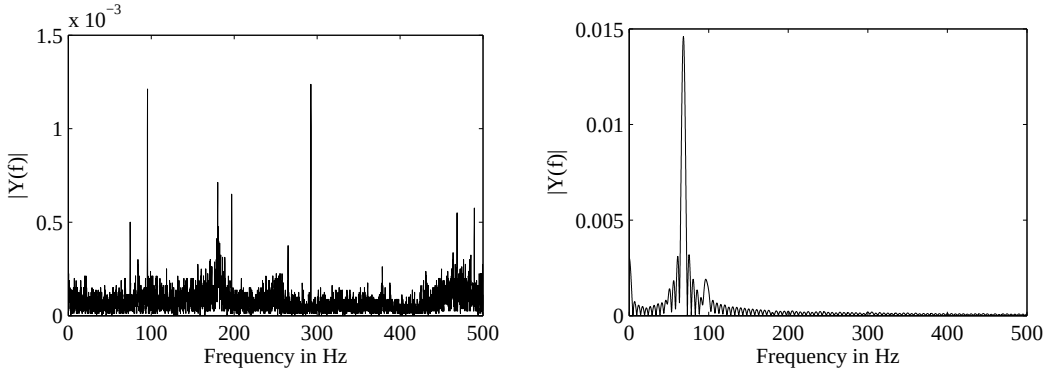

Figure 3.10.: FFT signal obtained with an accelerometer. Left: The accelerometer was placed outside the cryostat. Right: The accelerometer was fixed to a metal bar. This bar was used to excite the vibrations inside the hollow resonator rods.

inside the resonator both vibrating at the same resonant frequency. The source of the vibrations is identified by nucleate boiling, explaining why the oscillations are mainly observed in a normal fluid helium bath. At 400 MHz less power is dissipated and hence less bubbles are excited, since RF losses scale approx. with f^2.

A more rigid support cannot suppress the oscillations, since the rods inside the cavity are vibrating. A solution would be a faster feedback system, which can keep the cavity on resonance even when the rods are vibrating. The current system is similar to the systems applied for all vertical cavity test stands at CERN (LHC, SPL, HIE Isolde). It has only been modified to be capable for measurements at the three resonant modes used, by replacing the implemented local oscillator with an external frequency generator. A feedback system based on a self-excited loop

[111] could suppress the oscillations furthermore. The implementation is currently under discussion [112].

The oscillations can be suppressed, but not completely avoided by measuring inside a superfluid helium bath. At none of the three exploited modes the mechanical oscillations set the final limitation for the highest field level reached. They only made measurements more cumbersome.

3.6.3. Obtained Accuracy and Resolution

The resolution of the Quadrupole Resonator is limited by the minimum detectable heating. The temperature controller used (Lake Shore 340) enables to measure the temperature of the sample surface with a resolution of 0.1 mK. This corresponds to a heating between 2.5 µW at 2 K and 12.5 µW at 8 K for a reactor grade bulk niobium sample ($RRR \approx 70$) see Fig. 3.11 (left). To derive the minimal measurable surface resistance from the minimal detectable heating Eq. (3.10) is differentiated with respect to P_{DC2} to yield

$$|\Delta R_{\mathrm{S}}| = \frac{2\mu_0^2 \Delta P_{\mathrm{DC2}}}{\int\limits_{\mathrm{Sample}} B^2 \mathrm{d}S}. \tag{3.24}$$

From this equation one can obtain the lowest detectable surface resistance. For B_{p}=5 mT it would be 0.44 nΩ at 2 K and 2.2 nΩ at 8 K. For higher magnetic field the resolution is better, while for materials of higher thermal conductivity, in particular niobium films on copper substrate, it is worse.

If one wants to analyze the surface resistance as a function of temperature measured at a single resonant mode for constant magnetic field, the following statistical error sources need to be taken into account for the analyses if a possible offset is not considered. The helium bath temperature could only be stabilized to approx. ± 0.3 mK. This yields an uncertainty three times higher than the minimal detectable heating. Usually the noise of the current source used to control the sample temperature (Lake Shore 340), which is 50 µV+0.001 % of its value as defined by the manufacturer, exceeds this contribution. The voltmeter used to measure this (Keithley 2001) was operated in the 200 V range. Here the resolution of the device is 10 µV, well below the current source noise. The 200 V range was always used, to avoid possible errors in the measurements from range switching. The non-linearity within this single range must also be taken into account as a systematic error. The manufacturer defines this value as less then 1 ppm (typical) and less then 2 ppm (maximum) of range, corresponding to 200(400) µV (typical and maximum) here. These values are high compared to the statistical contributions. However, they are defined for the full 200 V range, while only voltages below

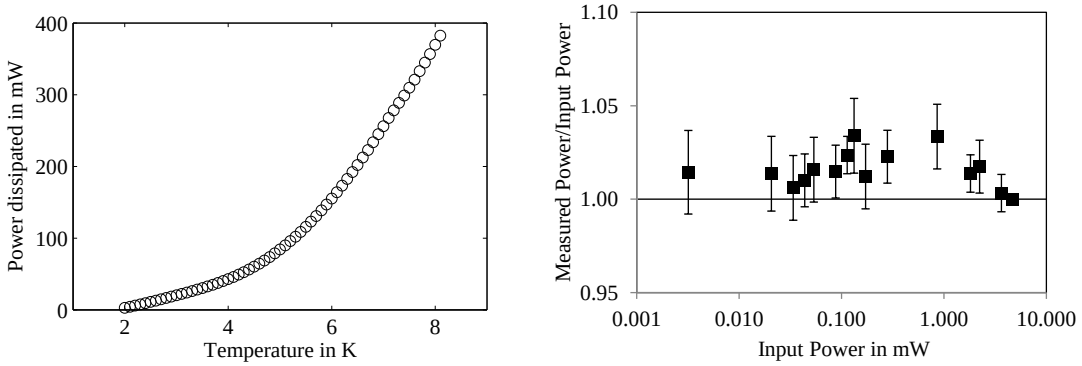

Figure 3.11.: Left: Power dissipated on the sample surface of a reactor grade bulk niobium sample as a function of temperature. Right: Power measured with spectrum analyzer from a calibrated input source. The error bars include calibration uncertainties of the used attenuators.

25 V were measured.

If the surface resistance as a function of field for one resonant mode is being investigated the non-linearity of the spectrum analyzer (HP 8519) needs to be taken into account. The device can be calibrated by an internal source. It is not as straight forward to define the linearity of the spectrum analyzer as for the voltmeter. In order to maintain high sensitivity over a wide power range, one needs to allow the spectrum analyzer to switch between internal attenuators depending on input power. Defining a fixed attenuation level would either limit the measurement range or yield poor accuracy in the low power regime. Instead of relying on data given by the manufacturer calibrated attenuators were used to compare the reading of the spectrum analyzer with the applied power, see Fig. 3.11 (right). Deviations of up to 3.4 % were measured. The spectrum analyzer systematically overestimates the input power.

If one is interested in comparing measurements of different frequencies further systematic uncertainties need to be taken into account. The spectrum analyzer is used to measure the transmitted power in the control room. The value measured here must be correlated to the power transmitted from the cavity. This value is measured with a power meter (Agilent 3500A). This device has an absolute accuracy of 5.4 %. Only the power transmitted from the cavity through the coaxial cable inside the cryostat can be measured directly. To derive the losses in the coaxial cable a network analyzer is used to measure the cable attenuation. The network analyzer has a transmission uncertainty of 2.1 %. In combination with the uncertainties from the field calculations, which need to be taken into account here as well the total absolute uncertainty is about 8 %. Only at very low fields do the statistical uncertainties described above dominate the overall uncertainty.

3.7. Summary

In this chapter it was shown that the Quadrupole Resonator enables to measure the surface resistance of superconducting samples at multiple frequencies. Its magnetic field distribution is almost identical for the 400, 800 and 1200 MHz Quadrupole modes. This, in combination with its frequency dependent ratio between surface magnetic and electric field, enables unique tests of the non-linear surface resistance.

Possible limitations for operation at 800 and 1200 MHz were identified. The biggest constraint is set by mechanical oscillations of the resonator rods, triggered by helium boiling inside them. These were found to be most perturbing at 1200 MHz but not preventing measurements in a superfluid helium bath.

4. Results on Surface Impedance and Critical RF Field

In this chapter measurement results obtained with the Quadrupole Resonator with regard to surface impedance and critical RF field are presented. A bulk niobium and a niobium thin film sample sputtered on top of a copper substrate are studied in detail. Even though made from the same material different preparations (Sec. 4.1) can yield different loss mechanisms and limitations under RF exposure.

Measuring the penetration depth as a function of temperature enables to determine material parameters related to the purity of the samples, see Sec. 4.2. These are used for analyzing surface resistance (Sec. 4.3 and 4.4) and critical RF field (Sec. 4.5) data. A comparison of measurement results with predictions from theoretical models introduced in Chap. 2 is also carried out.

4.1. Sample Preparation for RF Testing

A reactor grade ($RRR \approx 50$) bulk niobium sample was prepared by buffered chemical polishing (BCP). For the final tests precautions were taken to ensure that the acid temperature did not exceed 15 °C, to avoid an increased surface resistance caused by hydrides [1]. BCP uses a mixture of hydrofluoric, nitric and phosphoric acids. For the preparation of superconducting cavities these chemicals are usually used in the volume ratio of 1:1:1 or 1:1:2. The nitric acid oxidizes the niobium surface. The hydrofluoric acid reduces the niobium pentoxide into a salt, which is soluble in water. The phosphoric acid acts as the moderator in this chemical reaction giving rise to a less turbulent and more controllable reaction. A description of the process and possible alternative surface preparation techniques are described in [113]. For the preparation of the bulk niobium sample the 1:1:2 ratio was used, which gives an etching rate of approx. 1 µm/min [114].

In total, this sample was cooled down nine times. Almost all the results presented are from the last test run. Exceptions are explicitly mentioned. The first eight cooldowns had mainly the purpose of developing the test stand and the integration of new equipment. In the measurements performed between the fifth and eighth cooldown the sample had a larger surface resistance caused by hydrides (Q-disease) and quenched at lower field due to a local defect. In the following

the sample will be referred to as dirty bulk niobium sample, if measurements were taken during one of these cooldowns. If the data presented is from the last cooldown the sample will be referred to as clean bulk niobium sample. No data from the first four cooldowns will be presented. If the condition is not explicitly mentioned the term bulk niobium sample refers to the clean bulk niobium sample. Before each RF test in the Quadrupole Resonator the sample was rinsed with ultrapure water (R>17.5 MΩ) at about 5 bar.

The second sample investigated is a niobium film DC magnetron sputtered with a normal incident angle on to a oxygen-free high thermal conductivity (OFHC) copper substrate, in the following referred to as niobium film sample. The deposition procedure was identical to the one applied for the LHC cavities. In fact a dummy LHC cavity built of stainless steel was used as sample holder during sputtering. The sample was placed in a position at the equator of the cavity, see Fig. 4.1. In a superconducting cavity operated in the accelerating TM_{010}-mode this is the position of high magnetic and low electric surface fields. The sputter gas used was argon. Prior to coating, the copper substrate was chemically polished in order to obtain a clean and smooth surface. The polishing agent used is called SUBU. It is a mixture of sulfamic acid, hydrogen peroxide, n-butanol and ammonium citrate [62, 115]. Preparation and first tests on this sample were done in 1998. Before being retested in 2011 it underwent the same cleaning procedure as applied to the bulk niobium sample, rinsing with ultrapure water. In between these tests the sample was kept under normal air.

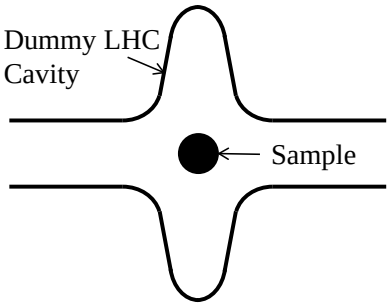

Figure 4.1.: Position of sample for sputtering.

4.2. Penetration Depth

The fact that in the superconducting state the penetration depth λ changes rapidly with temperature can be used for its measurement [97]. If ω varies only slowly with time ($\omega^{-2} d\omega/dt << 1$), U/ω is an adiabatic invariant [116]. In this case the Slater theorem [117, 118] can be applied. It gives a relation between the changes of the stored energy U and the resonant frequency f,

$$\frac{\Delta U}{U} = \frac{\Delta f}{f}. \tag{4.1}$$

At the transition between vacuum and a superconductor the electric field needs to be perpendicular to the interface. For this boundary condition the Slater theorem reads:

$$\frac{\Delta f}{f} = \frac{\frac{1}{4}\int_{V}^{V+\Delta V}(\epsilon_0|\vec{E}|^2 - \mu_0|\vec{H}|^2)\mathrm{d}V}{U} \tag{4.2}$$

For clean superconductors the perpendicular electric field penetrates less than 1 nm in the material and the depth does not change with temperature [52]. This is why, the electric contribution of Eq. (4.2) can be neglected, allowing to simplify the expression to

$$\frac{\Delta f}{f} = -\frac{\frac{1}{4}\int_{V}^{V+\Delta V}(\mu_0|\vec{H}|^2)\mathrm{d}V}{U}. \tag{4.3}$$

An increase of the penetration depth λ is equivalent to an increase of the electromagnetic cavity volume V and therefore $\mathrm{d}V = \mathrm{d}A\mathrm{d}\lambda$. The definition of the sample geometry factor G_{Sample} Eq. (3.12) is used to derive

$$\Delta\lambda = \lambda(T) - \lambda_0 = -\frac{G_{\mathrm{Sample}}}{\pi\mu_0 f^2}\Delta f, \tag{4.4}$$

where λ_0 is the penetration depth at 0 K. Measuring the resonance frequency of the Quadrupole Resonator for different sample temperatures enables to obtain $\Delta\lambda$. Since the host cavity is thermally decoupled, $\Delta\lambda$ is the value of the sample surface only. The measurement has been performed using a frequency counter with a resolution of 1 Hz (Racal Dana 1992). The results obtained for the bulk niobium sample are displayed in Fig. 4.2 (left). The right side shows the data for the niobium film sample.

From a least squares fit to the Gorter-Casimir expression [119]

$$\lambda(T) = \frac{\lambda_0}{\sqrt{1-(\frac{T}{T_\mathrm{c}})^4}} \tag{2.44}$$

λ_0 and T_c are derived. The fit results are displayed by the blue lines in Fig. 4.2. From λ_0 the electron mean free path l can be obtained from an expression found by Pippard [66]:

$$\lambda(l) = \lambda(l\to\infty)\sqrt{1+\frac{\pi\xi_0}{2l}}. \tag{2.46}$$

The London penetration depth λ_L and the BCS coherence length ξ_0 are assumed to be independent on temperature. Their values were taken from literature, where for niobium films both values have found to be lower compared to bulk niobium,

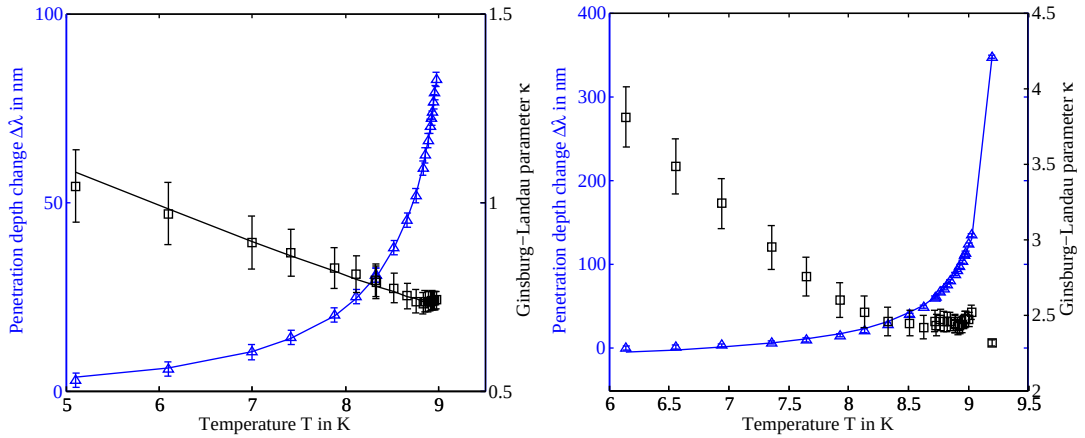

Figure 4.2.: Blue Triangles: Penetration depth change as a function of temperature measured at 400 MHz for the bulk niobium sample (left) and the niobium film sample (right). Blue Line: Least squares fit to two fluid model. Black squares: Derived Ginsburg Landau parameter. Black line (left): $\kappa(T) = 1.41/(1 + (T/T_c)^2)$.

see Tab. 4.1. The residual resistance ratio RRR was calculated from l using the empirical relation [16]

$$l[\mathrm{nm}] = 2.7 \cdot RRR. \tag{4.5}$$

All values of material parameters derived from the $\Delta\lambda$ measurements are shown in Tab. 4.2. The uncertainties for the parameters are systematically higher for the bulk niobium sample for two reasons. The sample has a lower thermal conductivity and therefore a less uniform temperature distribution on the surface. The value λ_0 is close to λ_L, resulting in a high uncertainty for l, as can be seen from Eq. (2.46).

The Ginsburg-Landau parameter κ can be derived from the measured penetration change $\Delta\lambda$ and the derived penetration depth at 0 K λ_0 by Eq. (2.43):

$$\kappa = \frac{\lambda(T,l)}{\xi_{\mathrm{GL}}} = \frac{2\sqrt{3}}{\pi}\frac{\lambda(T,l)^2 \cdot (1 - (\frac{T}{T_c})^2)}{\xi_0 \lambda_{\mathrm{L}}}, \tag{2.43}$$

where $\lambda(T,l) = \lambda_0 + \Delta\lambda$. The Ginsburg Landau parameter is expected to depend

Table 4.1.: Literature values of material parameters

Sample	λ_{L} in nm	ξ_0 in nm	References
Bulk niobium	32	39	[53]
Niobium film	27	33	[62]

on temperature as

$$\kappa(T) = \frac{\kappa(0)}{1 + \left(\frac{T}{T_c}\right)^2}, \tag{4.6}$$

as can be seen be applying Eq. (2.44) to Eq. (2.43). This dependency is well observed for the bulk niobium sample, see Fig. 4.2 (left). For the niobium film sample this is not the case for the whole temperature range. Figure 4.2 (right) shows an increase of κ for decreasing temperature as expected, but close to the critical temperature T_c, κ is almost constant. This can be explained by the non-uniformity of the film. The penetration depth for which κ is obtained is between 74 nm close to 0 K and up to 500 nm close to T_c.

Table 4.2.: Material parameters derived from least square fits to penetration depth measurements

Sample	λ_0 in nm	T_c in K	l in nm	RRR
Bulk niobium	39±4	9.25±0.03	110±40	42±16
Niobium film	73.8±1.6	9.244±0.002	12.1 ±0.4	4.5±0.2

4.3. Low Field Surface Resistance

The Quadrupole Resonator was designed to measure the surface resistance R_S of the samples attached by the RF-DC compensation technique, introduced in Sec. 3.3. For magnetic fields below 15 mT R_S is assumed to be independent of the field strength and can be written as a sum of BCS and residual resistance,

$$R_S = R_{BCS}(f, T) + R_{Res}(f). \tag{4.7}$$

Figures 4.3 and 4.4 display R_S for an applied RF magnetic field of approx. 15 mT in the temperature range between 2 and 10.6 K for the bulk niobium and the niobium film sample respectively.

In the normal conducting regime above T_c, the surface resistance depends only slightly on temperature as can be seen from the flat curves in this area. For these temperatures the normal conducting surface resistance of the sample R_N can also be derived by a non-calorimetric 3 dB bandwidth method [120]. The measurement is only possible when the sample is normal conducting and the coupling changes from strongly overcoupled to strongly undercoupled. This means that in the latter case the majority of the power coupled in is dissipated on the sample surface instead of being coupled out. The loaded quality factor Q_L consists of the quality

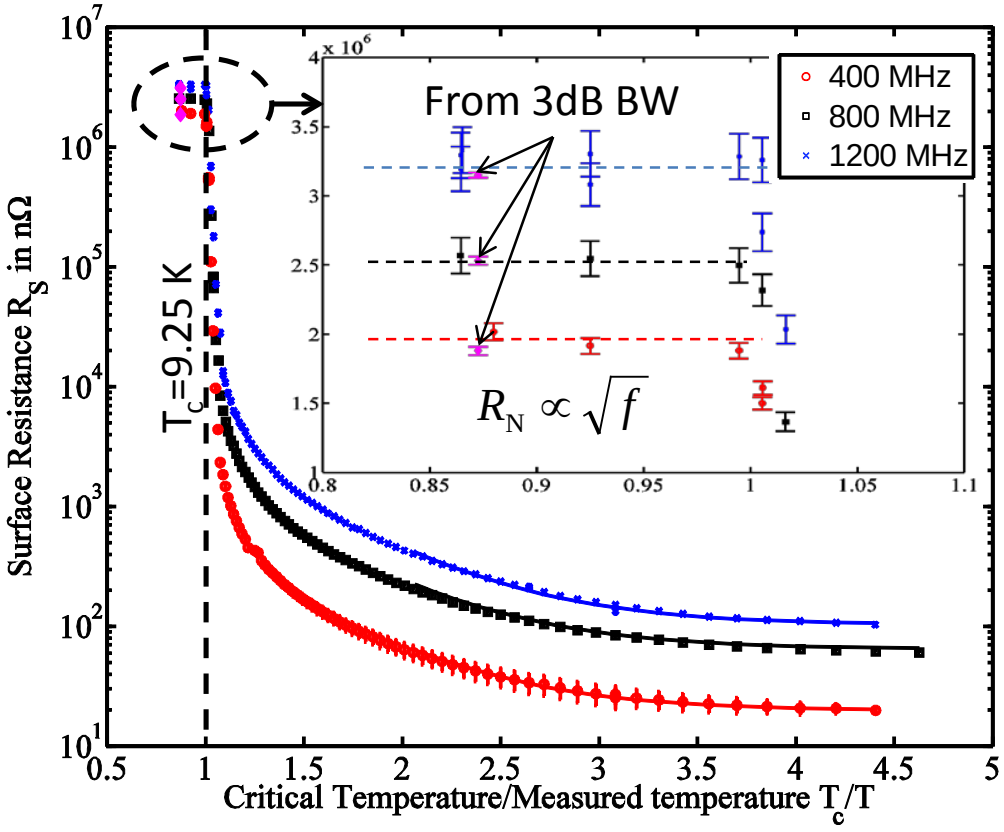

Figure 4.3.: Surface resistance of the bulk niobium sample for three frequencies as a function of temperature, measured at a magnetic field of about 15 mT. The solid lines show least squares fits to BCS theory. In the normal conducting regime above T_c the surface resistance was also derived from 3 dB bandwidth measurements.

factors of the host cavity Q_C, the sample Q_{Sample} and the two couplers combined Q_{ext}

$$\frac{1}{Q_L} = \frac{1}{Q_{ext}} + \frac{1}{Q_C} + \frac{1}{Q_{Sample}}. \tag{4.8}$$

In the superconducting state Q_L was measured to be about 10^6, dependent on frequency. The quality factor of the sample Q_{Sample} can be derived from the calorimetric measurement:

$$R_S = \frac{G_{Sample}}{Q_{Sample}}, \tag{4.9}$$

where G_{Sample} is the geometry factor of the sample. It relates the losses on the sample surface to the stored energy in the cavity. At 2 K R_S is several tens of nanoohms corresponding to Q_{Sample} values of several times 10^9. The host cavity

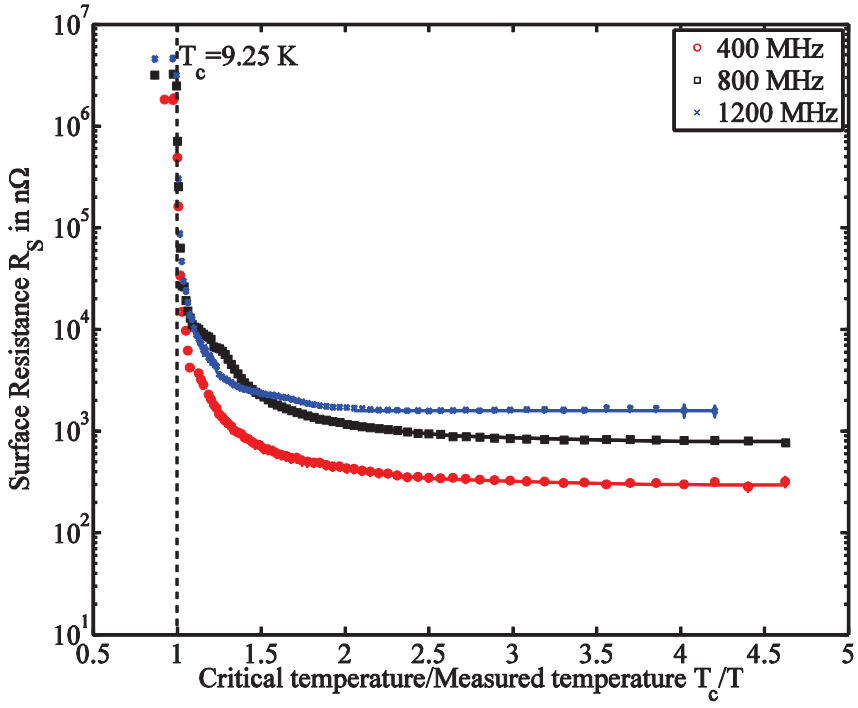

Figure 4.4.: Surface resistance of the niobium film sample for three frequencies as a function of temperature, measured at a magnetic field of about 15 mT. The solid lines show least squares fits to BCS theory.

is made of the same material as the sample. Therefore, its surface resistance is considered to be almost identical. From this assumption and the field configuration of the Quadrupole Resonator one can estimate Q_{C} to be about ten times lower than Q_{Sample}. This is still two orders of magnitude higher than Q_{L}, allowing to simplify Eq. (4.8) to

$$\frac{1}{Q_{\mathrm{L}}} = \frac{1}{Q_{\mathrm{ext}}}. \tag{4.10}$$

If the sample is normal conducting the system becomes undercoupled. The host cavity remains superconducting, since it is thermally decoupled from the sample. Thus, $1/Q_{\mathrm{C}}$ remains negligible and Eq. (4.8) reads

$$\frac{1}{Q_{\mathrm{L}}} = \frac{1}{Q_{\mathrm{ext}}} + \frac{1}{Q_{\mathrm{Sample}}}. \tag{4.11}$$

Q_{Sample} can now be calculated with Q_{ext} obtained from the measurement in the superconducting state. From Q_{Sample} one derives R_{S} using Eq. (4.9).

The results from these non-calorimetric 3 dB bandwidth measurements agree within 4 % with the results obtained from the calorimetric measurements, see

Fig. 4.3. They verify the calorimetric approach and therefore give also confidence in the measurements at lower temperatures. The surface resistance in this normal conducting regime is found to be proportional to $\sqrt{f}$ as expected for normal skin effect. It can be expressed as

$$R_{\mathrm{N}} = \sqrt{\frac{\pi f \mu_0}{RRR \cdot \sigma_0}}, \tag{4.12}$$

where σ_0 is the electrical conductivity at room temperature. Its value $6.58 \cdot 10^6\,(\Omega\mathrm{m})^{-1}$ is taken from literature [7] to derive RRR=68.6±3.5. This value is larger than the one derived from the penetration depth measurements, see Sec. 4.2, which can be explained by the different thickness of the surface layer penetrated by the magnetic field. In the normal conducting state the penetration depth is about 10 times higher than in the superconducting state for the bulk niobium sample at the frequencies investigated[1].

The solid lines in Fig. 4.3 and 4.4 show predictions from least squares fits to BCS theory performed with Win Super Fit [121, 122]. The program uses the Levenberg-Marquardt algorithm [123, 124] for χ^2 minimization. It is based on the widely used Halbritter code for the calculation of the surface resistance [45]. The implementation has been done using the algorithms found in [125]. For the data presented here the superconducting energy gap Δ and the residual resistance R_{Res} were varied to minimize χ^2. The derived values for both samples are given in Tab. 4.3. Other input parameters, which were set constant in the program are the critical temperature T_{c} and the mean free path l derived from penetration depth measurements, see Tab.4.2. The BCS coherence length ξ_0 and the London penetration depth λ_L were taken from the literature, see Tab. 4.1.

The obtained residual resistance R_{Res} of the bulk niobium sample is as expected for reactor grade material [126]. For the niobium film sample R_{Res} is about 10 times higher at all frequencies. A further analysis of the residual resistance of both samples can be found in the next section. The energy gap Δ of the bulk niobium sample is found consistent for the three measurements. It is also consistent with theory and other measurements [53]. For the niobium film sample Δ has a lower value. This sample was kept under normal air for 11 years prior to the measurements presented here. Therefore it is strongly oxidized. It has been shown that oxidation can reduce the energy gap [127]. Taking this into account allows to conclude that for the niobium film sample the energy gap is also obtained consistent with theory and other measurements at 400 MHz and 800 MHz [127]. At 1200 MHz

[1] Deriving RRR by this method is only applicable for the bulk niobium sample, because the normal conducting penetration depth in niobium is larger than the film thickness of the niobium film sample. The magnetic fields not only penetrate the niobium film but also the copper substrate.

a derivation of Δ was impossible, because at this frequency the error of the surface resistance is higher than for the two other frequencies due to mechanical vibrations of the resonator rods, see Sec.3.6.2. These vibrations result in fluctuations of the transmitted power, inversely proportional to the surface resistance. The energy gap Δ is correlated only to the BCS and not to the residual part of the surface resistance. At 2 K and 1200 MHz the BCS contribution to the surface resistance of this sample is 6.8 nΩ [45]. This is about ten times lower than the statistical fluctuations of the total surface resistance R_S.

Another observation is that at 1200 MHz the increase of the surface resistance with temperature was lower than expected from BCS theory. Due to the high surface resistance the measurement was performed with variable pulse lengths up to 4 K, because in CW operation the RF dissipation would have resulted in a higher temperature even for low field. The fact that the surface resistance increases less than expected in the regime where the measurement was performed with variable pulse length is an indication for a loss mechanism which is more pronounced at low duty cycle and/or low temperature. This could for example be the permanent quenching and re-condensation of a weak spot. Another feature, which cannot be explained within BCS theory for pure niobium, is that R_S is higher at 800 MHz than at 1200 MHz in the temperature regime between 6 and 8 K, see Fig. 4.4. The gradient dR_S/dT of the 800 MHz-curve in this temperature regime is higher than expected from BCS theory, indicating an additional loss mechanism. This could also be the permanent quenching and re-condensation of a weak spot. It might be only observable at 800 MHz, because at 400 MHz the spot remains superconducting and normal conducting for 1200 MHz, yielding permanent dissipation only at 800 MHz. These deviations from the BCS values of pure niobium might be correlated to oxygen enrichment at the surface, which can cause weak spots with transition temperatures below 7.2 K [128].

For the frequencies of 400 and 800 MHz at temperatures below 6 K all data can be well understood within BCS theory for pure niobium. This is the regime, which will be used to analyze the dependency of the surface resistance on field in the following.

Table 4.3.: Material parameters derived from low field surface resistance measurements below 4.5 K

	Bulk Niobium		Niobium Film	
f in MHz	Δ/k_B in K	R_{Res} in nΩ	Δ/k_B in K	R_{Res} in nΩ
400	18.2±0.5	19.8±0.8	14.9±0.9	295±8
800	18.4±0.4	62.8±0.6	15.8±0.5	788±3
1200	18.5±0.2	99.8±0.7	-	1600±30

4.4. Surface Resistance as a Function of Applied Field

4.4.1. Analysis of Individual Curves

In this section individual curves of the surface resistance as a function of applied field are presented. Measurement results are compared with analytical expressions introduced in Chap. 2. Results obtained at 4 K are investigated due to the high sensitivity of the calorimetric method at this temperature. At 4 K measurements can be performed in CW mode up to relatively high field values, avoiding error sources only relevant for pulsed measurements, see Sec. 3.3. The frequency of 400 MHz allows for measurements at 4 K up to highest achievable RF fields in CW operation, because at this frequency the least power is dissipated on the sample surface. This mode is least affected by mechanical vibrations and is the only mode for which the maximum RF field is not limited by the available amplifier power, see Sec. 3.6.

For the bulk niobium sample results will be presented from two cooldowns. In the tests performed during the sixth cooldown the sample showed a higher surface resistance caused by hydrides and early quench at a local defect. In this dirty condition the sample had a residual resistance of $55.6\pm0.2\,\mathrm{n\Omega}$. Its energy gap $\Delta/k_\mathrm{B}=17.0\pm1.1\,\mathrm{K}$ was found to be lower as compared to $18.4\pm0.5\,\mathrm{K}$ for the sample being in a clean condition. The clean condition was obtained before the ninth and final cooldown by an additional chemical etching (BCP 100 µm), see Sec. 4.1.

Figures 4.5 and 4.6 display the surface resistance as a function of applied RF magnetic field for the clean and the dirty sample respectively. For the niobium film sample the data is displayed in Fig. 4.7. In the following the applicability of five models, introduced in Sec. 2.3, to the individual curves will be discussed. These models account for the non-linear surface resistance by different field dependent loss mechanisms.

- The *pair breaking* and the *weak layer* model consider the energy gap to be dependent on magnetic field.
- The *hot spots* model takes localized heating from defects into account.
- Scattering of thermally activated quasiparticles at impurities is the source for non-linear losses as described by the *impurity scattering* model.
- Tunneling of electrons between localized states in oxides and states in the superconductor yields losses as described by the *interface tunnel exchange* model.

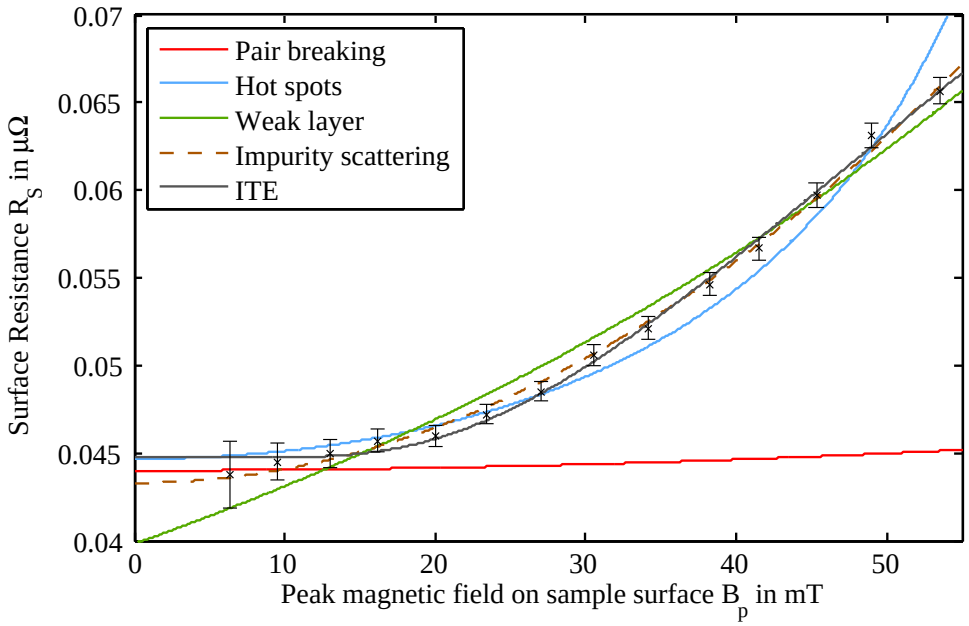

Figure 4.5.: Surface resistance at 400 MHz and 4 K as a function of applied magnetic field for the clean bulk niobium sample.

The data has been analyzed using the standard MATLAB® [129] algorithms from the curve fitting toolbox, including the coefficient of determination R^2. The closer the value of R^2 is to unity the better the data is represented by the applied model compared to the simple average. Therefore data of the clean bulk niobium sample with the largest spread between minimum and maximum value of R_S gave the highest values of R^2 for all models. For the niobium film sample R^2 is lowest for all models due to its high residual resistance. This has to be taken into account when the applicability of one model to the individual samples is compared, while R^2 values obtained for one sample by different models can be directly compared to each other. Tables 4.4 to 4.7 show the derived fit parameters and the coefficient of determination R^2 for all models, except for the *pair breaking* model, which does not include any free parameters. The errors given for the derived parameters are the 95 % confidence bounds.

Interface tunnel exchange: To fit the data according to the *interface tunnel exchange (ITE)* model an additional residual surface resistance R_res accounting for the losses at low field is added to Eq. (2.26). The complete formula reads

$$R_\mathrm{S} = R_\mathrm{res} + \frac{R^\mathrm{E}_{400}}{c_3}\frac{f}{400\,\mathrm{MHz}}\left[\mathrm{e}^{-b/E_\mathrm{p}} - \mathrm{e}^{-b/E^0}\right], \quad E_\mathrm{p} \geq E^0. \tag{4.13}$$

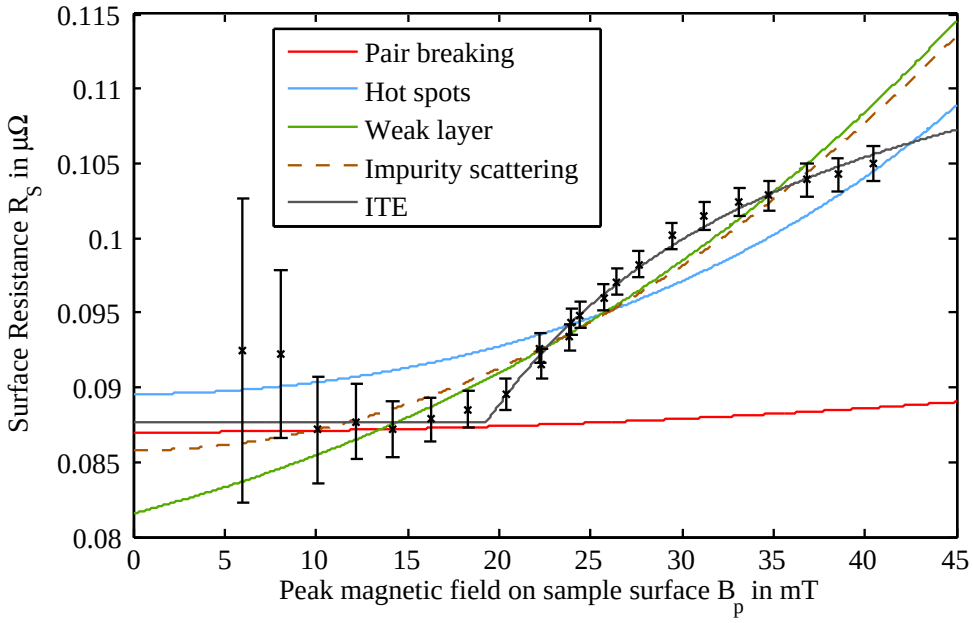

Figure 4.6.: Surface resistance at 400 MHz and 4 K as a function of applied magnetic field for the dirty bulk niobium sample.

The frequency dependent factor c_3 introduced in Sec. 3.4 transforms the electric losses to an equivalent magnetic surface resistance. This allows writing the residual losses assumed to be caused by the magnetic field and the non-linear losses caused by the electric field in one sum. The model can give a good prediction for all three data sets. It is the only model giving a reasonable fit for the dirty bulk niobium and the niobium film sample. The source for losses from interface tunnel exchange is oxidation and especially crack corrosion along grain boundaries [57]. It is therefore not surprising that ITE is the dominant loss mechanism for dirty bulk niobium and niobium film surfaces. The derived fit parameters, found in Tab. 4.4, have high uncertainties for b and R^{E}_{400}. These two parameters influence each other very strongly. If one is altered the other can compensate for this change giving a good fit over a wide parameter range. A better determination of these parameters is possible by a collective fit to a larger data set comprising curves of different frequencies. These are discussed in the following section.

Table 4.4.: Fit parameters interface tunnel exchange model

	R_{Res} in nΩ	R^{E}_{400} in µΩ	E^0 in MV/m	b in MV/m	R^2
Bulk clean	44.8±0.5	0.13±0.03	<1.06	5.0±0.5	0.996
Bulk dirty	87±1	0.3-1.4	1.00±0.05	0.8-3.8	0.993
Film	320±20	0.15-800	0.48±0.22	<23.5	0.943

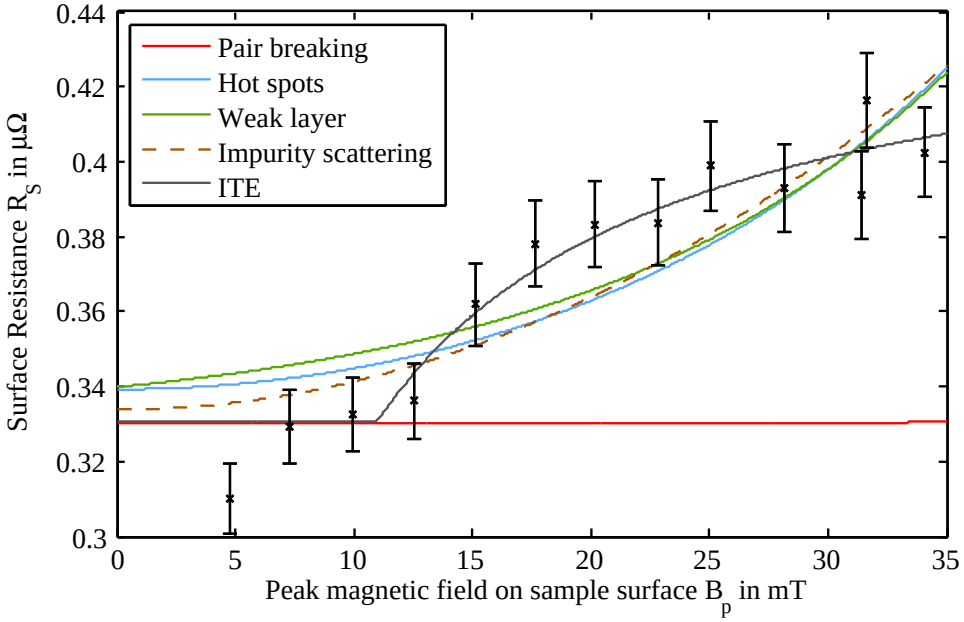

Figure 4.7.: Surface resistance at 400 MHz and 4 K as a function of applied magnetic field for the niobium film sample.

Pair breaking and thermal feedback: The *pair breaking model*, Eq. (2.15) includes no free fit parameters. The total surface resistance R_S including also BCS and residual losses is expressed as

$$R_S = \left[1 + \frac{\pi^2}{384}\left(\frac{\Delta}{T}\right)^2\left(\frac{B_p}{B_c}\right)^2\right] R_{BCS} + R_{Res}, \tag{4.14}$$

where R_{Res} and R_{BCS} are taken from the low field surface resistance measurements, see Sec.4.3. The predicted increase of R_{Res} with applied RF magnetic field is far too low to explain any of the three data sets. It cannot be correlated to global thermal feedback either, because this effect does not occur in the Quadrupole Resonator. The measured temperature is precisely the temperature of the RF side. Therefore, it can be concluded that global thermal feedback, even in combination with pair breaking in the current carrying state can be excluded as the dominant mechanism for the medium field Q-slope.

Results from Ciovati on temperature maps of the outer cavity surface of elliptical cavities as a function of applied field have shown that localized defects contribute to the medium field Q-slope [122]. Localized heating is detectable with the Quadrupole Resonator. Four temperature sensors are placed on the back side of the sample. Since the RF field is axial symmetrically distributed on the sample surface, see Fig 4.8 (left), two diodes should always measure the same temperature

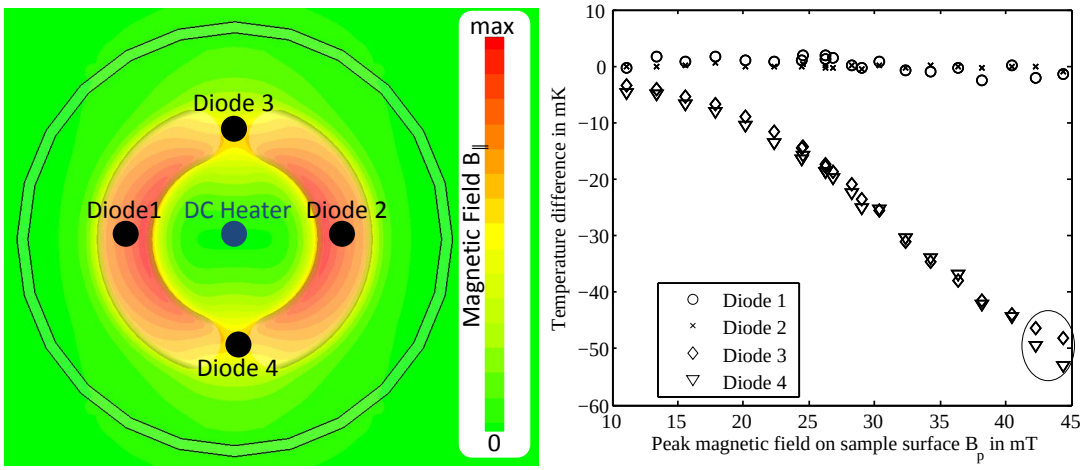

Figure 4.8.: Left: Position of the temperature sensors (diodes) on the back side of the sample and magnetic field B on the sample surface. Right: Difference of the temperature without and with the RF field applied measured with four diodes as a function of applied field B.

if the heating is uniform. Figure 4.8 (right) shows the difference of the measured temperature without and with the RF field applied. The data is depicted for the bulk niobium sample in dirty condition, corresponding to the measurement of the surface resistance displayed in Fig. 4.6. The DC current applied to the heater on the back side of the sample is controlled to keep the temperature of diode 1 constant. Diode 2, located opposite to diode 1, shows the same temperature independent of the applied RF magnetic field, see Fig. 4.8 (right). This indicates uniform heating. The diodes 3 and 4 are placed in a position of lower field. Therefore, these two sensors show a lower temperature when the heating is mainly caused by RF (higher field). These two diodes also show no indication of localized heating up to 40 mT, within their resolution, represented by the size of the symbols in Fig. 4.8 (right). Only above 40 mT diode 3 shows a higher temperature than diode 4 when the RF field is being applied. Above 45 mT the temperature cannot be controlled any more. It slowly rises until a quench occurs. The surface resistance becomes unmeasurable. It can be concluded that medium field Q-slope can occur without localized heating even if a defect is found on the sample.

Hot spots: The conclusion that localized heating is not responsible for the nonlinear losses is also supported by the relatively poor agreement of the *hot spots* model with all measured curves. It is represented by Eq. (2.20) and the linear

resistance $R_{\mathrm{lin}} = R_{\mathrm{BCS}} + R_{\mathrm{res}}$:

$$R_{\mathrm{S}} = R_{\mathrm{lin}} \left[1 + \frac{g}{1 - (B_{\mathrm{p}}/B_{\mathrm{b0}})^2} \right]. \tag{4.15}$$

For the clean bulk niobium sample it has a relatively high coefficient of determination R^2=0.96, but one can clearly see in Fig. 4.5, that the data is systematically underestimated between 30 and 45 mT. The measurement is not well represented by the fit.

The hot spots model has been successful in predicting the surface resistance of a bulk niobium cavity which showed a Q-drop around 120 mT [130]. In this publication a relative high coefficient of determination R^2=0.960 was derived. However, the fit presented underestimated the medium field Q-slope and the high value of R^2 was only obtained, because the data included high field data, where the Q-drop occurs. Localized heating at hot spots can certainly cause quenching; it might also be responsible for the Q-drop at high fields. However, strong medium field Q-slope cannot be explained by this model.

Table 4.5.: Fit parameters hot spots model

	B_0 in mT	g	R_{lin} in nΩ	R^2
Bulk clean	50-77	0.02-0.9	24-47	0.96
Bulk dirty	45-80	0.04-2.6	24-87	0.82
Film	40-75	0.08-16	24-330	0.74

Weak layer: The *weak layer* model can predict the data slightly better than the hot spots model. It is represented by

$$R_{\mathrm{BCS}} = A \exp\left(-\frac{\Delta}{k_{\mathrm{B}} T} + \frac{p_{\mathrm{F}} v_{\mathrm{s}}}{k_{\mathrm{B}} T} \right). \tag{4.16}$$

with[2]

$$\frac{p_{\mathrm{F}} v_{\mathrm{s}}}{k_{\mathrm{B}} T} = \frac{B_{\mathrm{p}} \lambda_0 e v_{\mathrm{F}}}{k_{\mathrm{B}} T} \left(\frac{1}{\rho_{\mathrm{s}}} \right)^{1/2}, \tag{2.18}$$

where ρ_{s} is the superfluid density, which is one at 0 K and zero above the critical temperature T_{c}. For the clean bulk niobium sample the data is especially well fitted by the model. The biggest issue with the derived fit parameters however is, that ρ_{s} is found with an unphysical value above 1 for all curves, see Tab. 4.6.

[2] These two formulas are derived without taking into account a weak layer. The model is named here weak layer model only, because the formula was derived as part of a model which contains a weak layer to describe the surface resistance especially in the low field region.

Table 4.6.: Fit parameters weak layer model

	A in $\mu\Omega$	ρ_s	R^2
Bulk clean	1.69±0.10	16-23	0.97
Bulk dirty	2.00±0.10	10-16	0.95
Film	1.2±0.9	2-17	0.76

Impurity scattering: The *impurity scattering* model is represented by Eq. (2.16) plus BCS and residual losses:

$$R_S = \left[1 + \gamma(l, \omega, T)\left(\frac{B_p}{B_c}\right)^2\right] R_{BCS} + R_{Res}. \tag{4.17}$$

It fails to give a good prediction for the dirty bulk niobium and the niobium film data. The R^2 value for the dirty bulk niobium sample is relatively high, but it can be clearly seen in Fig. 4.6 that the model systematically overestimates the data between 10 and 20 mT, while it underestimates the data between 20 and 30 mT. The measurement is not well represented by the fit. This model predicts the curve of the clean bulk niobium sample best, see Tab. 4.7.

Table 4.7.: Fit parameters impurity scattering model

	R_{BCS} in nΩ	γ	R^2
Bulk clean	24.3±0.5	11.7±0.6	0.997
Bulk dirty	30±2	16±4	0.94
Film	40±20	80±60	0.78

In other publications a quadratic dependence of the surface resistance on field has been widely found in the intermediate field region, see for example [57]. It is, however, unknown how the parameter γ depends on temperature. The *percolation model* [61] predicts a factorization of the temperature and the field dependent part of the non-linear surface resistance and therefore γ, to be independent of temperature. In contradiction the *impurity scattering* [37, 59] model predicts γ to decrease with temperature similar to the pair breaking model.

Experimental results for the frequency dependence of γ are rare. Elliptical cavities can be excited at multiple frequencies, but the field configurations are different for each mode. The other option is to use several cavities of same shape and field configuration but with different size and resonance frequency. In this case the challenge is to produce identical surface conditions for each cavity. The Quadrupole Resonator modes at 400 and 800 MHz have almost the same magnetic field configuration. This, and the wide available temperature range, make it the

perfect tool for probing the dependence of γ on temperature and frequency. Figure 4.9 shows the BCS surface resistance of the clean bulk niobium sample as a function of field at 400 (left) and 800 MHz (right) for several temperatures. The residual resistance derived in Sec. 4.4 has been subtracted for all curves. The data is plotted in a semi-logarithmic scale. This allows to see how γ depends on T. If the curves are parallel, γ is a constant. This seems to be the case for most of the curves. The measurement at 400 MHz and 6 K appears to deviate from a constant γ. However, it is apparent that the derived least squares fit overestimates the low field data and underestimates the high field data, yielding a lower value of γ. Figure 4.10 depicts all the derived values of γ. Within the error bars, representing the 95 % confidence bounds, there is no dependency of γ on temperature or frequency.

This allows to conclude that γ is independent of temperature, at least between 3 and 7.5 K. Furthermore, no significant dependence on frequency at least between 400 and 800 MHz is found. A constant γ implies a factorization of the non-linear surface resistance in a temperature and a field dependent part as predicted by the *percolation model*.

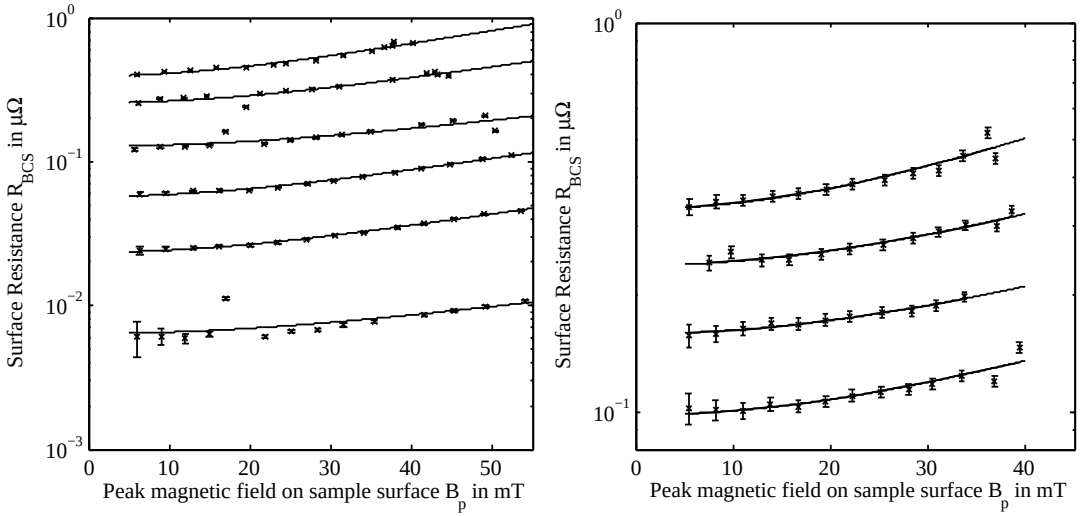

Figure 4.9.: Surface resistance at 400 (left) and 800 MHz (right) as a function of applied magnetic field for the bulk niobium sample in clean condition. The curves are from buttom to top for 3, 4, 5, 6, 7 and 7.5 K at 400 MHz and for 4, 5, 5.5 and 6 K at 800 MHz.

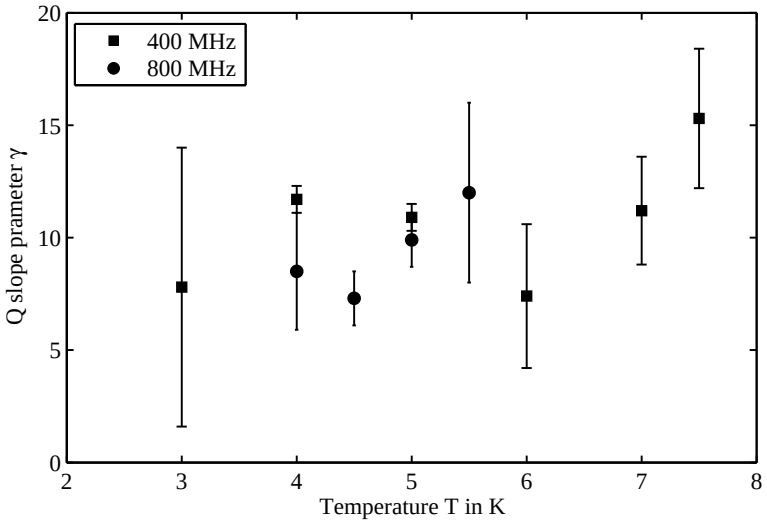

Figure 4.10.: Q slope parameter γ of the clean bulk niobium sample as a function of temperature for 400 and 800 MHz. The values are derived from the data displayed in Fig. 4.9.

4.4.2. Analysis of Large Data Sets

In the following, two data sets each comprising about 200 quadruples (R_S, B, T, f) obtained with the Quadrupole Resonator are investigated by least squares multiparameter fits to the whole data sets. Tested are the *percolation* and the *interface tunnel exchange* model. All the other models, considered in Sec. 4.4.1 were in contradiction with the data of the single curves and will not be considered anymore.

The data sets comprise only measurements performed at 400 and 800 MHz. At 1200 MHz the available amplifier power limited the measurement range to about 15 mT[3]. Furthermore, stabilizing the field level at this frequency is rather difficult due to 69 Hz mechanical oscillations of the resonator rods, see Sec. 3.6. Results obtained on the clean bulk niobium sample and the niobium film sample will be presented. No data of the dirty bulk niobium sample will be considered here, because it was only measured at 400 MHz for fields above 15 mT, since a 800 MHz amplifier was not available during these early tests.

Percolation Model Data of the bulk niobium sample consisting of 215 quadruples (R_S, B, f, T) has been analyzed by a least squares fit to the *percolation model*, introduced in Sec. 2.3.2. This model assumes the total surface resistance R_S to be

[3] Later on measurements of the critical field at 1200 MHz for higher field levels will presented. These measurements were carried out with a different amplifier, which was unavailable at the time the surface resistance measurements were performed.

a sum of a linear BCS contribution R_{BCS}, a non-linear field depended part R_{nl} and a residual part independent of temperature and magnetic field B

$$R_{\mathrm{S}}(f,T,B) = R_{\mathrm{BCS}}(f,T) + R_{\mathrm{nl}}(f,T,B_{\mathrm{p}}) + R_{\mathrm{Res}}(f), \tag{4.18}$$

where for the BCS contribution

$$R_{\mathrm{BCS}} \simeq \frac{3\Delta}{2k_BT}\mu_0^2\omega^2\sigma_0 \cdot RRR \cdot \frac{\lambda(T,l)^4}{l} \ln\left(\frac{1.2T\Delta\xi_0^2}{\hbar^2\omega^2\lambda(T,l)^2}\right) e^{-\Delta/k_BT} \tag{2.12}$$

is used here, since it gives a good approximation if the mean free path l is larger than the BCS coherence length ξ_0 [1]. For the clean bulk niobium sample this is the case, as has been shown by penetration depth, low field surface resistance and normal conducting surface resistance measurements. All the parameters of Eq. 2.12 were derived by at least one of these methods. Since Eq. 2.12 is only an approximation, it was decided to vary the penetration depth at 0 K and use the Gorter-Casimir expression [50] for its temperature dependence

$$\lambda(T) = \frac{\lambda_0}{\sqrt{1-\left(\frac{T}{T_{\mathrm{c}}}\right)^4}}. \tag{2.44}$$

The value of the superconducting energy gap Δ/k_B=18.4 K was taken from the low field surface resistance measurements. The residual resistance ratio RRR and the mean free path l are directly proportional to each other [16]

$$l[\mathrm{nm}] = 2.7 \cdot RRR. \tag{4.5}$$

Their values have no influence on R_{BCS}, because in the clean limit the surface resistance is not affected by impurity scattering [1]. The values of the conductivity at room temperature for niobium σ_0=$6.58 \cdot 10^6\,(\Omega\mathrm{m})^{-1}$ [7] and the BCS coherence length ξ_0=39 nm [53] are taken from literature. The residual resistance comprises a constant and one part scaling quadratically with frequency:

$$R_{\mathrm{Res}} = \mu_0^2\omega^2\sigma_0 \cdot RRR \cdot \lambda_0^2\Delta y + R_{\mathrm{Res2}}. \tag{2.28}$$

Here RRR=42 is taken from the penetration depth measurements, see Sec. 4.2. Fit parameters used for R_{Res} are its penetration depth Δy and its frequency inde-

pendent part R_{Res2}. The non-linear surface resistance is described by

$$R_{\mathrm{nl}} = \left[R_{\mathrm{Res1}} + \mu_0^2 \omega^2 \sigma_0 RRR \cdot \Delta x^3 \Theta(T' - T) \left(\frac{(T - T')}{(T_c - T')} \right) \right] \cdot (-1) \left[\frac{1}{\kappa^2} + \frac{\ln \left[1 - \kappa^2 \left(\frac{B_{\mathrm{p}}}{B_c(T)} \right)^2 \right]}{\kappa^4 \left(\frac{B_{\mathrm{p}}}{B_c(T)} \right)^2} \right], \tag{2.23}$$

Three parameters from this equation are altered for the least squares fit. They are the field but not temperature depended residual resistance R_{Res1}, the penetration depth of the non-linear resistance Δx and the percolation temperature T'. The critical temperature T_{c}=9.25 K and the Ginsburg-Landau parameter $\kappa(0\,\mathrm{K})$=1.41 are taken from the penetration depth measurement. The dependence of κ on T is assumed to be

$$\kappa(T) = \frac{\kappa(0)}{1 + \left(\frac{T}{T_{\mathrm{c}}} \right)^2}, \tag{4.19}$$

as derived in Sec. 4.2. The critical thermodynamic field B_{c}=199 mT is taken from literature [131, 132].

In total six parameters are varied to minimize χ^2. From Eq.(2.12) the penetration depth at 0 K, λ_0 is altered. To account for the residual resistance R_{Res2} and Δy are varied in Eq. (2.28). The surface resistance is field dependent already below the percolation temperature T'. This is accounted for by R_{Res1}. For temperatures above T' the surface resistance increases with applied field by a factor related to the penetration depth of the non-linear surface resistance Δx.

For comparison the data has been analyzed using a simple quadratic factorization of the BCS resistance, instead of the non-linear resistance from the percolation model. The residual contribution is used identically, yielding for the total surface resistance R_{S}:

$$R_{\mathrm{S}} = R_{\mathrm{BCS}} \left(1 + \gamma \left(\frac{B_{\mathrm{p}}}{B_{\mathrm{c}}} \right)^2 \right) + \mu_0^2 \omega^2 \sigma_0 RRR \cdot \lambda_0^2 \Delta y + R_{\mathrm{Res2}} \tag{4.20}$$

with the same expression for the BCS resistance as used for the percolation model, Eq. (2.12). The *quadratic BCS factorization* model has only one parameter γ to account for the non-linear losses. In total it has two fit parameters less than the percolation model accounting for the field dependent surface resistance with Δy, R_{Res1} and T'.

About one fifth of the complete data set and the predictions from the two models are displayed in Fig. 4.11. The error bars in this graph account for all statistical

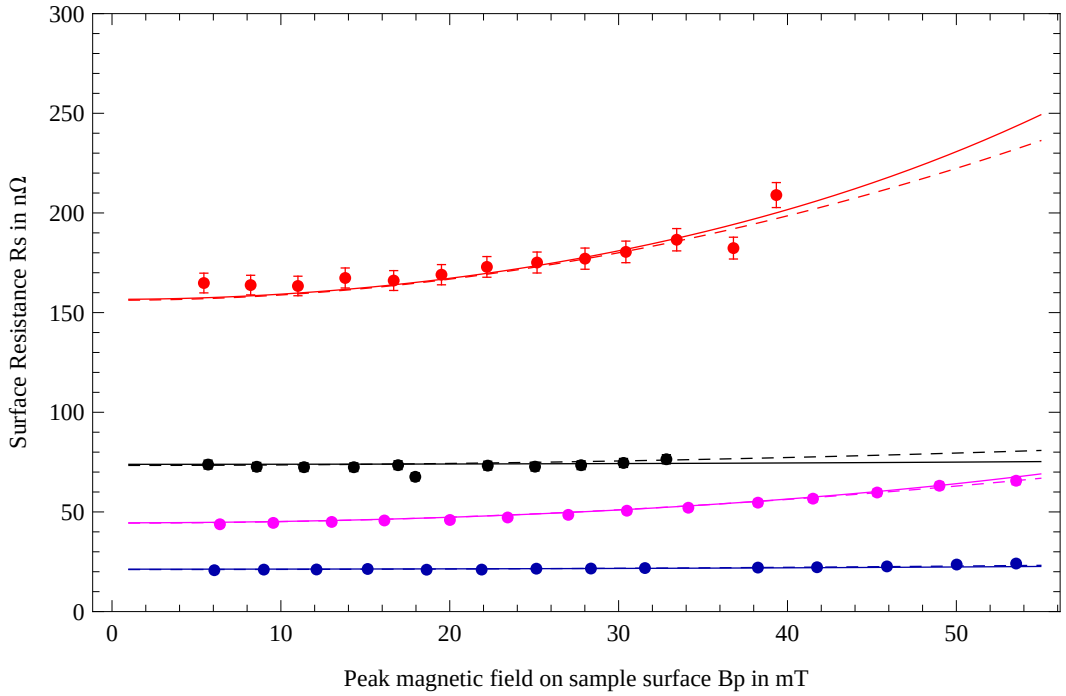

Figure 4.11.: Surface resistance at 400 MHz (2.5 K (blue), 4 K (magenta)) and 800 MHz (2.5 K (black), 4 K (red)) of the clean bulk niobium sample. The lines show predictions from least squares multiparameter fits to the complete data set comprising 215 values $R_S(B, f, T)$. Solid line: Prediction from Percolation Model. Dashed line; Prediction from quadratic BCS factorization model.

uncertainties. All the derived parameters can be found in Tab. 4.8. The given errors are the 95 % prediction bounds. For a χ^2 statistics they can be calculated for each parameter as following [125]:

- The parameter, for example λ_0, for which the error shall be calculated is set to a fixed value, different from the value for which χ^2 was at its minimum χ^2_{min}.
- By varying all other parameters a new minimum of $\chi^2 > \chi^2_{\text{min}}$ is derived.
- The value of λ is altered in both directions until $\chi^2 = \chi^2_{\text{min}} + 4$ is found. This value defines the 95 % confidence bounds.

This can be understood as the projection of an N-dimensional ellipse in parameter space to the one dimensional space of the parameter λ_0, where N is the number of free parameters. As an example $\chi^2 - \chi^2_{\text{min}}$ is displayed for the penetration depth λ_0 in Fig. 4.12 (left) as calculated with the percolation model. The right

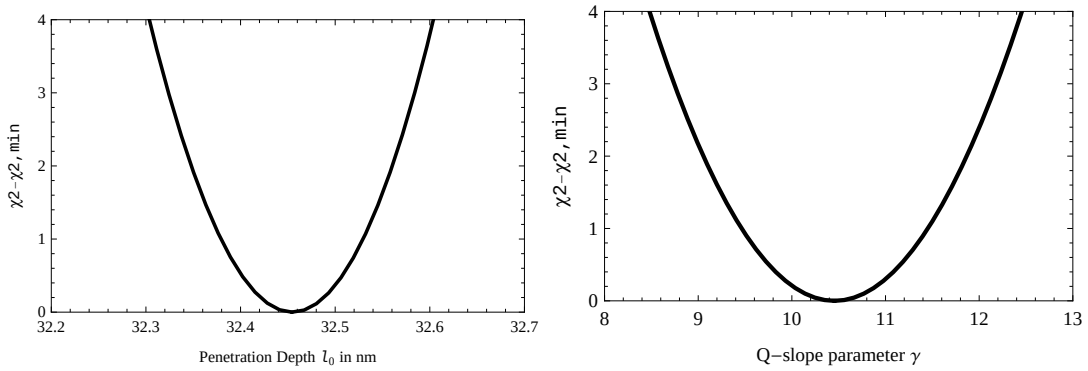

Figure 4.12.: Calculation of the 95 % prediction bounds for the parameters λ_0, from a least squares fit to the percolation model (left) and γ derived from a least squares fit to the quadratic BCS factorization model (right).

side of this figure shows the Q-slope parameter γ, derived with the quadratic BCS factorization model.

Both models find a value of χ^2 close to the number of quadruples, see Tab. 4.8. This is an indication that the data is well represented. The simpler model (quadratic BCS factorization) gives the larger value of χ^2 indicating a worse prediction. The two models share three common parameters, which are found with identical values within the uncertainties. The value of the penetration depth at 0 K λ_0 is closer to the London penetration depth λ_L=32 nm than to value of 39 nm derived from its direct measurement, see Sec. 4.2. This can be correlated to the

Table 4.8.: Parameters derived for least square fits to two different models for the surface resistance of the clean bulk niobium sample

Parameter	Percolation Model	Quadratic BCS	Values from [61]
λ_0 in nm	32.45 ± 0.15	32.4 ± 0.2	-
Δy in nm	3.29 ± 0.06	3.26 ± 0.07	1
R_{Res2} in nΩ	3.4 ± 0.4	3.3 ± 0.7	3
R_{Res1} in nΩ	28 ± 6	-	25
T' [K]	2.78 ± 0.08	-	2.015
Δx in nm	76.0 ± 1.5	-	41
γ	-	10.5 ± 1.7	-
Quadruples (R_{S}, B_{p}, f, T)	215	215	
χ^2	204.8	241.2	-

approximative nature of Eq. (2.12).

The parameter describing the frequency independent part of the residual resistance R_{Res2} is found as expected. The other parameter accounting for residual losses Δy is found higher than in [61]. Since this contribution is linked to losses from electrons remaining unpaired even for lowest temperatures, Δy can only be understood as an effective penetration depth. Being the only fit parameter accounting exclusively for frequency dependent residual losses; it must be certainly correlated to the defect density of the material. In [61] a variety of cavities of different surface treatment were investigated by a χ^2 minimization. These cavities were made of high grade material. It is therefore not surprising that a higher value Δy is found for the reactor grade bulk niobium sample.

The parameters accounting for the non-linear surface resistance in the percolation model T', Δx and R_{Res1} are all found with larger values compared to [61]. Only R_{Res2} is consistent within the error range. The physical interpretation of Δx must be as an effective penetration depth, similar to Δy. It is correlated to the number of unpaired electrons created by the percolation effect, see Sec 2.3.2. These allow for early flux entry already at magnetic field values below about 100-130 mT, where the Q-drop starts and complete flux tubes enter the material. The percolation temperature T' is found to be significantly higher than in [61]. However, it must be stated that only measurements at 2 K and above have been taken into account for the analysis presented here and at 2 K the residual resistance was highly dominating the overall losses. Further tests of the percolation model with the Quadrupole Resonator would require a lower bath temperature and a sample with lower residual resistance. For the tests carried out in the framework of this thesis the lowest bath temperature achieved was 1.8 K and the lowest residual resistance was about 20 nΩ.

Even though, χ^2 is lower for the percolation model, one may argue that the introduction of a separate non-linear resistance might not be necessary, since the data can be well represented by the factorization of the BCS resistance. The value found for γ is consistent with the values derived in Sec. 4.4.1 for the same sample but different temperature range. For the collective fit here the range between 2 and 4.5 K was used. Above 4.5 K Eq. (2.12) becomes invalid. For the analyses of the single curves temperatures between 3 and 7.5 K were investigated. Below 3 K the residual resistance is the dominant contribution resulting in a large uncertainty for γ, if it is derived from a single curve with fixed temperature.

Due to the inhomogeneous field distribution on the sample surface of the Quadrupole Resonator, the non-linear surface resistance R_{nl} is underestimated compared to a system with a complete uniform magnetic surface field. If R_{nl} increases quadratically with magnetic field it is underestimated by a factor of 0.55 identically for the modes at 400 and 800 MHz as has been calculated with Microwave

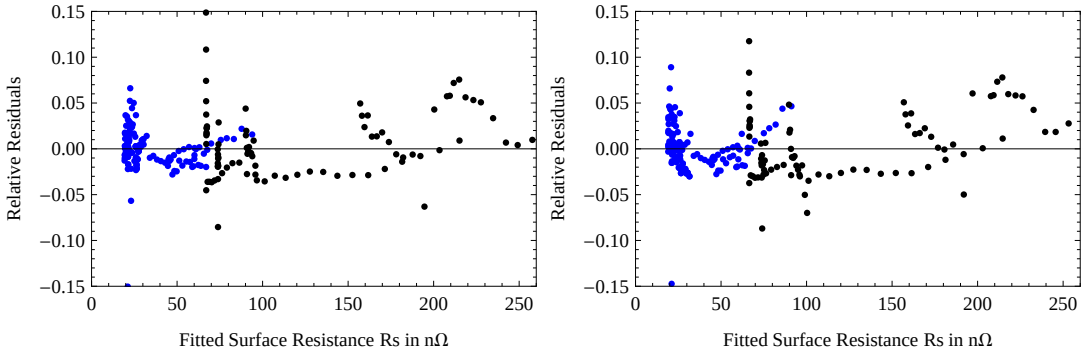

Figure 4.13.: Relative residuals from the χ^2 minimization to the percolation model (left) and the quadratic BCS model (right); blue dots (400 MHz), black dots (800 MHz)

Studio® [102]. This affects the parameter γ of the quadratic BCS factorization model and Δx and R_{Res2} of the percolation model. If one would measure the surface resistance of the bulk niobium sample with a system with a completely uniform magnetic field one would derive a value of γ=19.1 instead of 10.5 as found with the Quadrupole Resonator. This is important to note in order to compare results obtained with different systems. For example elliptical cavities designed to accelerate particles traveling close to the speed of light underestimate the local field only by a factor of about 0.9 [64]. A detailed description how to correlate the measured R_{S} to its local value can be found in [64].

Systematic deviations of the derived surface resistance $R_{\mathrm{S}}(f_{\mathrm{i}}, B_{\mathrm{p,i}}, T_{\mathrm{i}})$ can be found by visualizing the residuals [133]

$$\varepsilon_{\mathrm{i}} = R_{\mathrm{S}}(f_{\mathrm{i}}, B_{\mathrm{p,i}}, T_{\mathrm{i}}) - R_{\mathrm{S,i}}. \tag{4.21}$$

Since all measured $R_{\mathrm{S,i}}$ have approx. the same relative error it was decided to analyze the relative residuals $\varepsilon_{\mathrm{i}}/R_{\mathrm{S}}(f_{\mathrm{i}}, B_{\mathrm{i}}, T_{\mathrm{i}})$. In Fig. 4.13, they are displayed as a function of $R_{\mathrm{S}}(f_{\mathrm{i}}, B_{\mathrm{i}}, T_{\mathrm{i}})$ for the percolation model (left) and the quadratic BCS factorization model (right). The relative residuals are evenly distributed around zero, but systematic trends can be seen. For example the 800 MHz data is systematically underestimated between 110 and 150 nΩ. These values correspond to one measurement at constant field. Above 150 nΩ R_{S} is systematically overestimated. The same trends are found for both models, indicating that they are either caused by a common term used in both models, for example the BCS resistance, or by systematic deviations in the measurements. Subtracting the mean value of the residuals separately for these two surface resistance ranges and minimizing χ^2 again yielded no change for the parameters derived within their prediction bounds, allowing to conclude that these systematic deviations have no influence on the parameter values derived.

Interface tunnel exchange The *interface tunnel exchange (ITE)* model could not give a reasonable fit for the data set of the bulk niobium sample. Two predictions from this model are not found in the data. According to ITE the increase of the surface resistance is only slightly dependent on temperature with the energy gap Δ and losses caused by ITE scale linearly with frequency. One can clearly see from Fig. 4.11 that both predictions are in contradiction to the measurement results. Note the strong slope observed for 4 K at 400 MHz, in comparison to the flat curve at 2.5 K and 800 MHz. It can be concluded that interface tunnel exchange is not the main contributor to the Q-slope observed for the bulk niobium sample in clean condition.

In the following a data set comprising 183 quadruples $(R_\mathrm{S} f, T, B)$ of the niobium film sample will be analyzed by χ^2 minimization. For this sample the field dependency of the surface resistance was found to be different compared to the bulk niobium sample. An exponential increase going into saturation for higher fields was found. This behavior could not be explained by the percolation or the quadratic BCS factorization model, but has been correlated to losses from interface tunnel exchange (ITE), see Sec. 4.4.1. These losses are caused by the surface electric field. That is why, for the total surface resistance an additional term R_S^E accounting for these has to be added. Assuming this part to be additive to the other losses, R_S becomes

$$R_\mathrm{S}(f, T, B_\mathrm{p}, E_\mathrm{p}) = R_\mathrm{BCS}(f, T) + R_\mathrm{nl}(f, T, B_\mathrm{p}) + R_\mathrm{Res}(f) + \frac{R_\mathrm{S}^\mathrm{E}(f, E_\mathrm{p})}{c_3}, \qquad (4.22)$$

where the frequency dependent factor c_3, introduced in Sec. 3.4, transforms the electric losses to an equivalent magnetic surface resistance allowing to write the complete losses in one summation.

For the niobium film sample the scaling of the residual resistance with frequency was found to be linear rather than quadratic, indicating other loss mechanisms. A linear dependence on frequency is a hint for losses contributed once per RF cycle. From the low field surface resistance measurements, Sec. 4.3, a residual resistance of $(295\pm8)\,\mathrm{n\Omega}$ at 400 Mhz and $(788\pm3)\,\mathrm{n\Omega}$ at 800 Mhz was found under the assumption that they are caused by the magnetic field. It is unlikely that R_Res is correlated to the surface electric field, because for the Quadrupole Resonator the electric surface resistance R_S^E and the magnetic surface resistance R_S are correlated to each other by

$$R_\mathrm{S}^\mathrm{E} = c_3 R_\mathrm{S} = 53.5 R_\mathrm{S} \frac{400\,\mathrm{MHz}}{f^2}. \qquad (4.23)$$

Thus, if one assumes the residual surface resistance to be caused by the electric field, one derives from the measured heating $R_\mathrm{S}^\mathrm{E}=(1580\pm40)\,\mathrm{n\Omega}$ at 400 Mhz and $R_\mathrm{S}^\mathrm{E}=(1050\pm40)\,\mathrm{n\Omega}$ at 800 Mhz. This would imply an unphysical higher electric

surface resistance at lower frequency. This allows to conclude that R_{Res} is at least mainly caused by the magnetic field. For the data analysis of the niobium film sample the residual resistance is assumed to be a sum of a frequency independent part plus a term scaling linearly with frequency, normalized to 400 Mhz

$$R_{\mathrm{Res}} = R_{\mathrm{Res2}} + R_{\mathrm{Res400}} \frac{f}{400\,\mathrm{MHz}}. \tag{4.24}$$

Two parameters of this equation R_{Res2} and R_{Res400} are altered to minimize χ^2. For the BCS resistance

$$R_{\mathrm{BCS}} = \mu_0^2 \omega^2 \sigma_0 RRR \cdot \lambda(T,l)^3 \frac{\Delta}{k_B T} \ln\left(\frac{\Delta}{\hbar\omega}\right) \frac{e^{-\Delta/k_B T}}{T} \tag{2.11}$$

is used, which is a good approximation in the dirty limit ($l \ll \lambda$) and therefore applies better than the clean limit to the niobium film sample, for which λ was found to be larger than l, even at 0 K. All the parameters of Eq. (2.11) were either derived by the penetration depth or the low field surface resistance measurement. However, since Eq. 2.11 is only an approximation, it was decided in analogy to the analysis of the bulk niobium sample, to vary the penetration depth at 0 K and use the Gorter-Casimir expression Eq. (2.44) for its temperature dependence. The residual resistance ratio RRR=4.5 is taken from the penetration depth and the superconducting energy gap Δ/k_{B}=15.3 K from the low field surface resistance measurement.

The field dependent surface resistance is assumed to comprise magnetic and electric contributions. For the magnetic part a quadratic factorization of the BCS resistance with one free parameter γ, as found for the bulk niobium sample, is assumed. The dominant non-linear loss mechanism for this sample is caused by interface tunnel exchange described by Eq. 2.26

$$R_{\mathrm{S}}^{\mathrm{E}} = R_{\mathrm{S,400}}^{\mathrm{E}} \frac{f}{400\,\mathrm{MHz}} \left[\mathrm{e}^{-b/E_{\mathrm{p}}} - \mathrm{e}^{-b/E^0}\right], \quad E_{\mathrm{p}} \geq E^0, \tag{2.26}$$

with the fit parameters $R_{\mathrm{S,400}}^{\mathrm{E}}$, b and E^0. In total seven parameters were varied to minimize χ^2. The values found and the corresponding 95 % prediction bounds can be found in Tab. 4.9.

The penetration depth at 0 K is found consistent with the value of its direct measurement, see Sec. 4.2. The residual resistance is found to be lower compared to the measurement at low field, see Sec.4.3. The reason for this is that ITE already contributed to the losses for this measurement performed at approx. 15 mT. The value of the parameter γ, accounting for the non-linear magnetic surface resistance, is close to the value derived for the bulk niobium sample. The non-linear losses are

Table 4.9.: Parameters derived for a least squares fit to the interface tunnel exchange model for the surface resistance of the niobium film sample

Parameter	Value	Uncertainty
λ_0 in nm	73.0	1.1
R_{Res2} in nΩ	50	4
R_{res}^{400} in nΩ	225	3
γ	13.4	0.5
$R_{\mathrm{S,400}}^{\mathrm{E}}$ in nΩ	6800	200
b in MV/m	0.84	0.08
E^0 in MV/m	0.625	0.015
Quintuples		
(R_{S},B,E,f,T)	183	
χ^2	157.2	

mainly caused by interface tunnel exchange, but adding this parameter lowered χ^2 by about 20 %. The value of $b{=}2\alpha\Delta\epsilon_{\mathrm{r}}/e\beta_{\mathrm{FE}}$ corresponds with the decay constant of the wave function into Nb_2O_5 $\alpha \cong (1.6\text{-}5.3)\,\mathrm{nm}^{-1}$ and the relative dielectric constant of Nb_2O_5 $\epsilon_{\mathrm{r}} \cong$ 10-15 [57] to a static field enhancement factor β_{FE} between 60 and 500. Even higher values up to 700 have been reported in literature, when field emission was investigated [134–136]. For a direct comparison it has to be noted that field emission is usually caused by localized particles at the surface, while the field enhancement responsible for the interface tunnel exchange is likely correlated to sharp grain boundaries. The value of $E^0{=}2\Delta\epsilon_{\mathrm{r}}/e\beta_{\mathrm{FE}}d$ has the same order of magnitude as b. This means that the wave function decays over a range comparable to the thickness of the oxide layer d.

The comparison of the parameters derived for the losses originating from ITE with literature values could not be undertaken due to lack of experimental data. In several publications this model was considered to be responsible for the Q-drop at high field [67, 69–72], but taking it into account for losses at low field for niobium films has not been done so far [137].

Figure 4.14 shows about one fourth of the data analyzed, consisting of 183 values $R_{\mathrm{S}}(B_{\mathrm{p}}, E_{\mathrm{p}}, f, T)$. The surface resistance is displayed as a function of applied magnetic field here. After subtracting all magnetic terms from Eq. (4.22) the electric surface resistance caused by interface tunnel exchange can be displayed separately, see Fig. 4.15. From this curve one can see that these losses only appear above the threshold field E^0. They are independent of temperature and scale linearly with frequency, as predicted by the model. Some values of $R_{\mathrm{S}}^{\mathrm{E}}$ for 400 MHz and 4 K are negative but are still consistent with zero, except for only one data point. An electric surface resistance of 1000 nΩ corresponds to a magnetic surface resistance

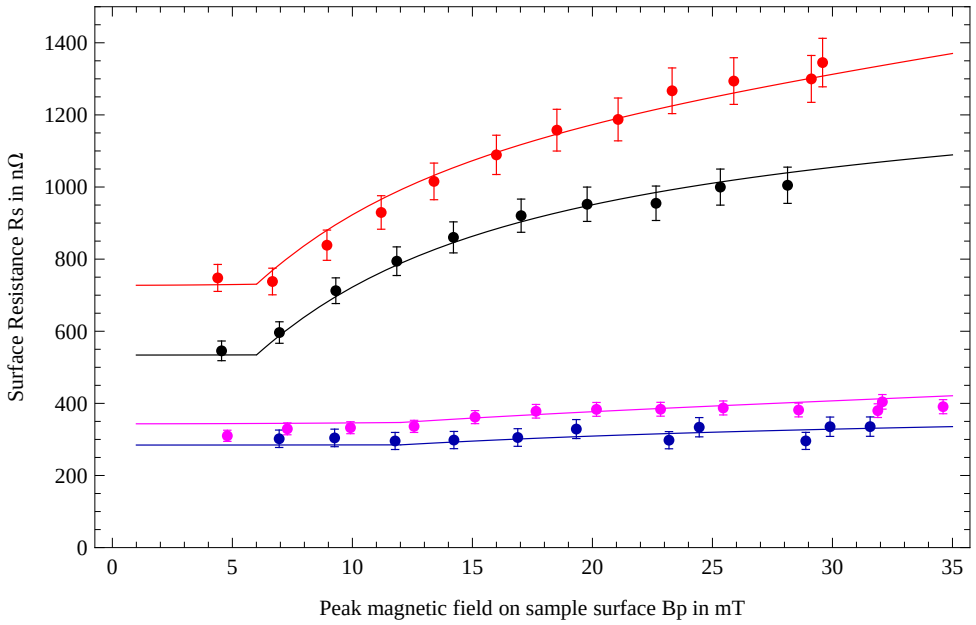

Figure 4.14.: Surface resistance at 400 MHz (2.5 K (blue), 4 K (magenta)) and 800 MHz (2.5 K (black), 4 K (red)) of the niobium film sample. The lines show predictions from a least squares multiparameter fit a the data set comprising 183 values $R_S(B, f, T)$.

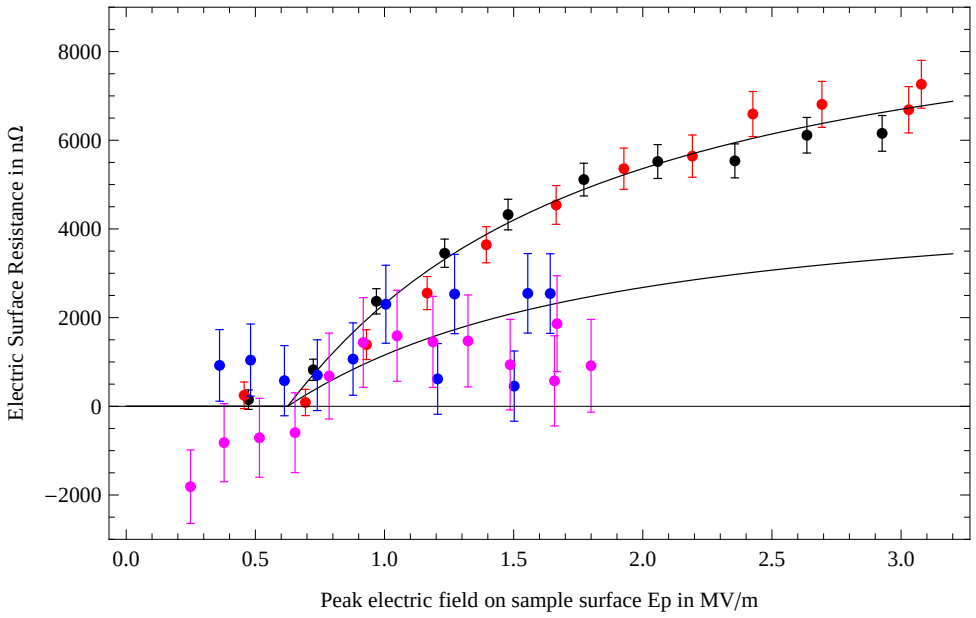

Figure 4.15.: Electric surface resistance at 400 MHz (2.5 K (blue), 4 K (magenta)) and 800 MHz (2.5 K (black), 4 K (red)) of the niobium film sample. The lines show predictions from a least squares multiparameter fit to a data set comprising 183 values $R_S(E, f, T)$.

of only 18.7 nΩ at 400 MHz. Comparison with Fig. 4.14 shows that the majority of the overall losses at 400 MHz are caused by the magnetic field. The peak electrical field E_p on the Quadrupole Resonator sample surface scales linearly with frequency for a given peak magnetic field B_p, as required by the law of induction as applied to the geometry in between the crooked ending of the rods and the sample. For a peak magnetic field B_p=10 mT, the peak electric field is E_p =0.52(1.04) MV/m for 400(800) MHz, respectively, as previously mentioned. That is why, the data at 400 MHz was only measured for electric fields below 2 MV/m, which corresponds to 35.0 mT. Measurements at higher field level were prevented by thermal runaway.

The residuals are evenly distributed. No apparent trend, that data is systematically over- or underestimated for one frequency or a specific area of the surface resistance can be found in Fig. 4.16. The residuals are systematically smaller at 800 MHz than at 400 MHz indicating that the model is better suited to describe the electric than the magnetic losses, which are only dominant at the higher frequency.

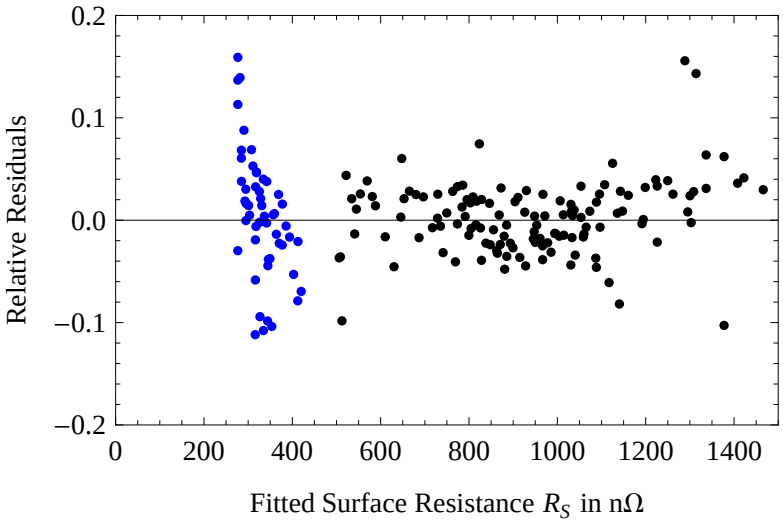

Figure 4.16.: Relative residuals from the χ^2 minimization to the interface tunnel exchange model; blue dots (400 MHz), black dots (800 MHz)

4.4.3. Comparison of results with HIE-ISOLDE cavity data

The HIE-ISOLDE 101.28 MHz quarter-wave cavities are currently under development at CERN. The design goal is a surface resistance of less than 46 nΩ at a peak surface magnetic field of 58 mT [138]. Similar to the niobium film sample investigated above the cavities are built by sputtering a micrometer thin niobium film

onto a copper substrate. Diode and magnetron sputtering are both investigated [139].

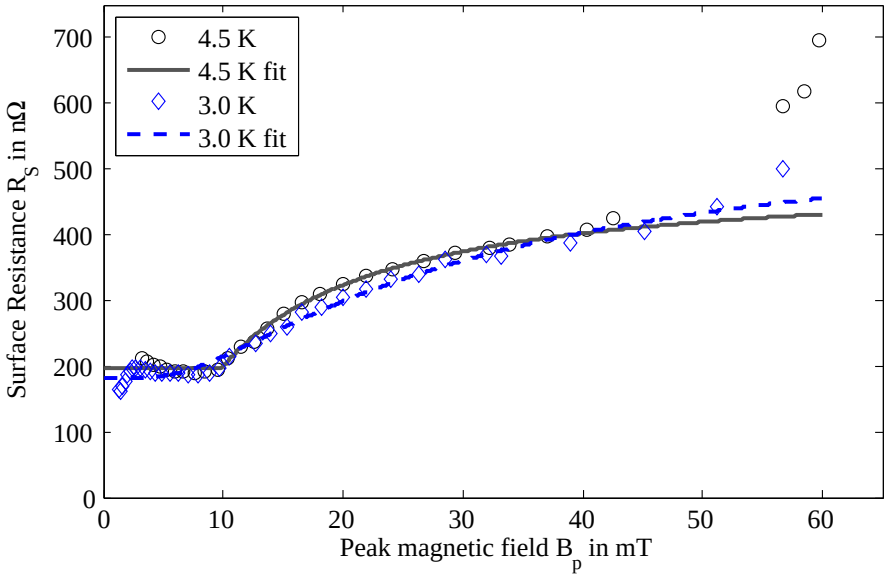

Figure 4.17.: Surface resistance of the HIE-Isolde quarter-wave cavity at 3 and 4.5 K [140]. The uncertainty is about 10 % for each data point. Measurement were performed by M. Therasse and I. Mondino (CERN).

In January 2012 the prototype cavity was produced by diode sputtering [140] on the basis of the experience of the Laboratori Nazionali di Legnaro (LNL) [141]. Unfortunately the cavity was performing below requirement for three reasons, see Fig. 4.17. In the low field regime the residual resistance is already at 200 nΩ. Above 40 mT R_S is strongly increasing due to field emission. At these field levels X-rays were detected. In the intermediate field region between 20 and 40 mT R_S is increasing by 200 nΩ. This can be correlated to losses from interface tunnel exchange, because the surface resistance starts to increase only above a threshold field, saturates at higher field and the slope is independent on temperature. For this cavity the magnetic and the electric geometry factor are almost equal. While the former is G=30.34 Ω [138], the latter is G^{E}=29.16 Ω [142]. So if one assumes $G \approx G^{\mathrm{E}}$ the electric and magnetic surface resistance can be displayed in one graph and the error caused by this assumption is only about 4 %. The ratio between peak electric and magnetic field is $E_{\mathrm{p}}/B_{\mathrm{p}}$=0.56 (MV/m)/mT [138]. The lines in Fig. 4.17 show predictions from least squares fits to

$$R_{\mathrm{S}} = R_{\mathrm{res}} + R^{\mathrm{E}}_{400}\frac{f}{400\,\mathrm{MHz}}\left[\mathrm{e}^{-b/E_{\mathrm{p}}} - \mathrm{e}^{-b/E^0}\right], \quad E_{\mathrm{p}} \geq E^0. \tag{4.25}$$

The electric surface resistance at saturation R^{E}_{400} is again normalized to 400 MHz

for direct comparision with the Quadrupole Resonator results. Data for fields below 5 mT was excluded for the fit, since Eq. (4.13) cannot describe the curve in this area, where the measurement is not completely understood. Data for fields above 40 mT was also excluded, because the increasing surface resistance in this area is caused by field emission and not by interface tunnel exchange.

The fit parameters obtained, Tab. 4.10, can be directly compared with the parameters found for the samples tested with the Quadrupole Resonator, Tab. 4.4 and 4.9. The onset field E^0 is higher for the HIE-ISOLDE cavity compared to the niobium film sample, indicating a lower field enhancement factor. The electric surface resistance at saturation R^{E}_{400} is approx. half the value compared to the results on the niobium film sample. This can be correlated to a weaker oxidation of the HIE-ISOLDE cavity and therefore less available localized states for the interface tunnel exchange process. The parameter b is again fitted with a value comparable to E^0, confirming that the wave function decays over a range comparable to the thickness of the oxide layer at the interface between the grains. The value of b is significantly higher at 4.5 K. At this temperature the BCS surface resistance is higher and non-linear magnetic losses are more relevant than at 3 K.

These HIE-Isolde cavity measurements confirm the conclusion from the Quadrupole Resonator results; ITE can significantly increase the surface resistance of superconducting cavities at relative low fields, especially for oxidized granular surfaces.

To reach the design requirements for the HIE-ISOLDE accelerator the losses in all three field areas have to be reduced. In the intermediate field region, the identification of ITE to be responsible for the dissipation can be exploited for the optimization of the sputtering and handling processes of future prototype cavities.

Table 4.10.: Fit parameters interface tunnel exchange model to HIE-ISOLDE cavity data

T in K	R_{Res} in nΩ	R^{E}_{400} in nΩ	E^0 in MV/m	b in MV/m	R^2
3	193±3	2600±900	5.4±0.2	3.5±1.6	0.9985
4.5	188±4	1640±80	5.0±0.4	9±3	0.9973

4.4.4. Summary and Conclusions

The field dependent surface resistance of a bulk niobium and a sputter coated niobium film sample on copper substrate has been investigated. First datasets of about 15 values of $R_{\mathrm{S}}(B_{\mathrm{p}})$ for fixed temperature and frequency have been analyzed. Several models have been tested on the data. It was shown that the non-linear surface resistance of the niobium film sample and the bulk niobium sample in dirty condition is mainly caused by the RF electric field via interface tunnel exchange

(ITE) between the superconductor and localized states in adjacent oxides. The field dependent surface resistance of the bulk niobium sample in clean condition is caused by the RF magnetic field and factorizes into a temperature and a field dependent part. These findings rule out several theoretical models. The non-linear surface is not caused by pairbreaking in the current carrying state, thermal feedback or localized heating at hot spots. A simple method to analyze surface resistance data of superconducting cavities is found. Simply from the shape of the measured curve R_S vs. B_p or E_p one can clearly distinguish between losses caused by the electric field acting through interface tunnel exchange and losses caused by the magnetic field. A concave curve indicates a magnetic and a convex curve an electric surface resistance.

Fitting data with fixed temperature and frequency to the theoretical models gave high uncertainties for the derived fit parameters. The models examined had up to four free parameters. In order to find out if the data can be explained with physically reasonable fit parameter values, large datasets of about 200 values $R_\mathrm{S}(B_\mathrm{p}, f, T)$ have been analyzed by least squares fits to the collective data. For the niobium film sample ITE was confirmed to be the dominant loss mechanism. In particular the electrical losses were found to be independent of temperature and to scale linearly with frequency. The electrical surface resistance is zero below a threshold field and saturates when all localized states participate in the exchange, as predicted by the ITE model. The data of the bulk niobium sample could be explained with the percolation model and a quadratic factorization of the BCS surface resistance. Both models assume the factorization of the magnetic non-linear surface resistance in a field and a temperature dependent part, as was found from the analysis of the single curves.

The result that ITE is a loss mechanism which can significantly increase the surface resistance, especially of superconducting niobium thin film cavities, could be further confirmed by recent measurements of the surface resistance of a HIE-ISOLDE quarter-wave cavity.

The combination of a quadratic factorization of the BCS surface resistance and additive losses from ITE give a complete picture of the non-linear surface resistance, at least for the samples investigated here and for fields below exponential increase (Q-drop). Experimentally these losses can be distinguished between by measuring at a relative high and low temperature T, since ITE losses only slightly depend on T.

4.5. Maximum RF Field

The Quadrupole Resonator has been designed for measuring the surface resistance of the attached samples. In the framework of this thesis further measurement capabilities have been investigated. It was found that the device is also suited to probe the maximum RF field $B_{\mathrm{max,RF}}$ of the samples. When a quench occurs a sudden drop of the transmitted power by several orders of magnitude is detected. One can easily determine, without further diagnostics, if it happened on the host cavity or on the sample by measuring the sample temperature in the moment the quench occurs. If the temperature rises above the critical temperature T_c it was on the sample, otherwise it must have been on the host cavity.

The critical field under RF exposure has been investigated using pulses just long enough that the stored energy in the cavity reaches steady state (pulse length $\approx 2\,\mathrm{ms}$) and also in continuous wave (CW) operation. Different field levels and dependencies on frequency have been found for each case. For analyzing the CW measurements it is assumed that $B_{\mathrm{max,RF}}$ has the same dependence on temperature as the critical thermodynamic field B_{c} and can therefore be written as

$$B_{\mathrm{max,RF}}(T) = B_{\mathrm{max,RF}}(0)\left(1-\left(\frac{T}{T_{\mathrm{c}}}\right)^2\right). \tag{4.26}$$

In order to measure the critical field in continuous wave (CW), first the magnetic field on the sample surface B_{p} is set to a fixed level. Then the sample temperature is slowly raised until the quench occurs. Usually a sudden temperature rise above T_{c} is observed the moment the quench occurs. If measured in CW the quench field is dependent on frequency and surface properties. In early tests the dirty bulk niobium sample quenched at relatively low field levels due to a local defect. A second etching (BCP 100 µm) yielded higher field levels for the clean sample, see Fig. 4.18. The fact that B_{p} vs. T^2 gives a straight line is an indication that an intrinsic superconducting field limitation is found for all curves. This can be explained by a local defect heating its surrounding area. When the temperature in the vicinity of the defect exceeds the field dependent critical temperature the quench occurs.

Fitting a straight line to the data displayed in Fig. 4.18 allows to derive T_{c} and $B_{\mathrm{max,RF}}(0)$. The intersection of each line with the x-axis gives T_{c}^2 and the slope $B_{\mathrm{max,RF}}(0)/T_{\mathrm{c}}^2$. The parameter values found for all curves are listed in Tab. 4.11. The quench field in CW is about twice as high at the lower frequency. This cannot be explained with the model for thermal breakdown introduced in Sec. 2.4.5, which assumes that quenching is completely a thermal effect caused by a normal conducting defect of surface resistance R_{N} heating the surrounding superconducting material. According to this model the quench occurs when the defect and the

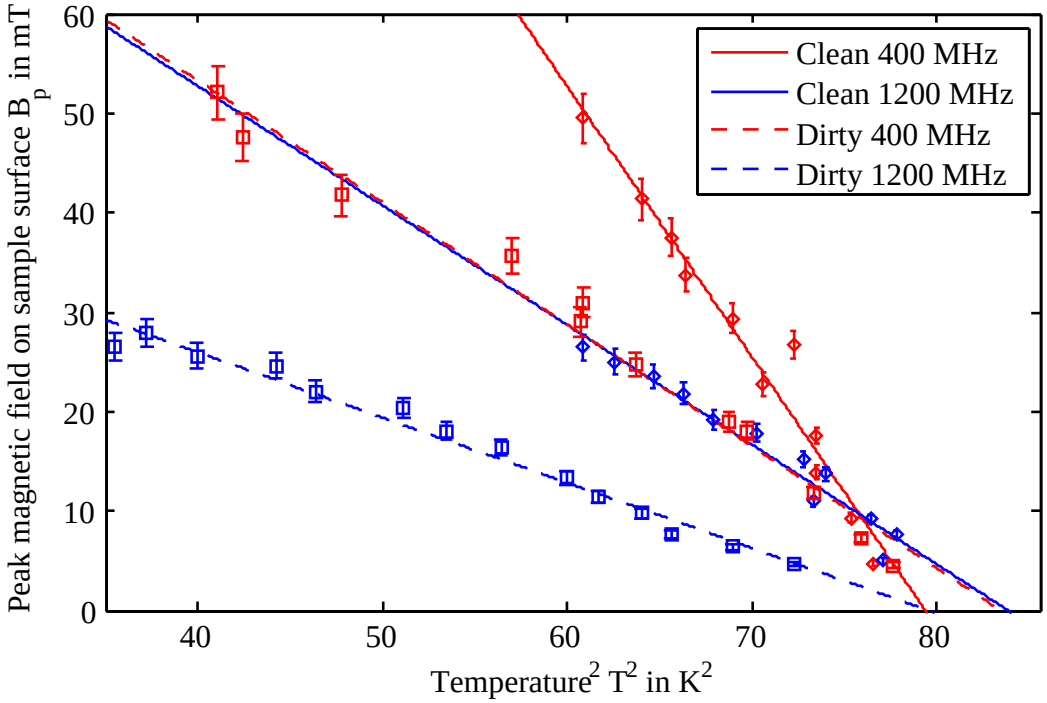

Figure 4.18.: Quench field $B_{\mathrm{max,RF}}$ of the bulk niobium sample in clean and dirty condition, measured in CW.

surrounding superconducting area reach a temperature above T_c. For a defect with normal skin effect this implies that the quench field scales with $f^{-0.25}$. The prediction for the measurements presented here is that the quench field at 400 MHz is only 1.3 times higher than at 1200 MHz. This is clearly in contradiction to the measurement results. It can also be excluded that the quench is a complete magnetic effect. In this case the same maximum field would be reached independent of frequency and duty cycle.

At 400 MHz $B_{\mathrm{max,RF}}(0)$ is above the critical thermodynamic field B_c of 199 mT [131, 132] for the clean sample. If short pulses are used an even higher value is found. A lower critical temperature compared to the value derived from the low field surface resistance and the penetration depth measurements was obtained. This is due to the fact that the position of highest field value is located about 1.5 mm closer to the heater than the position of the temperature sensors. For the following comparison of the maximum RF field with the models, introduced in Sec. 2.4, the value of 9.11 K derived from the pulsed measurement will be used.

Figure 4.19 shows the measured maximum RF magnetic field B_p normalized to the thermodynamic critical field B_c as a function of temperature. Here one can clearly see that B_p systematically exceeds B_c. Critical RF fields above B_c

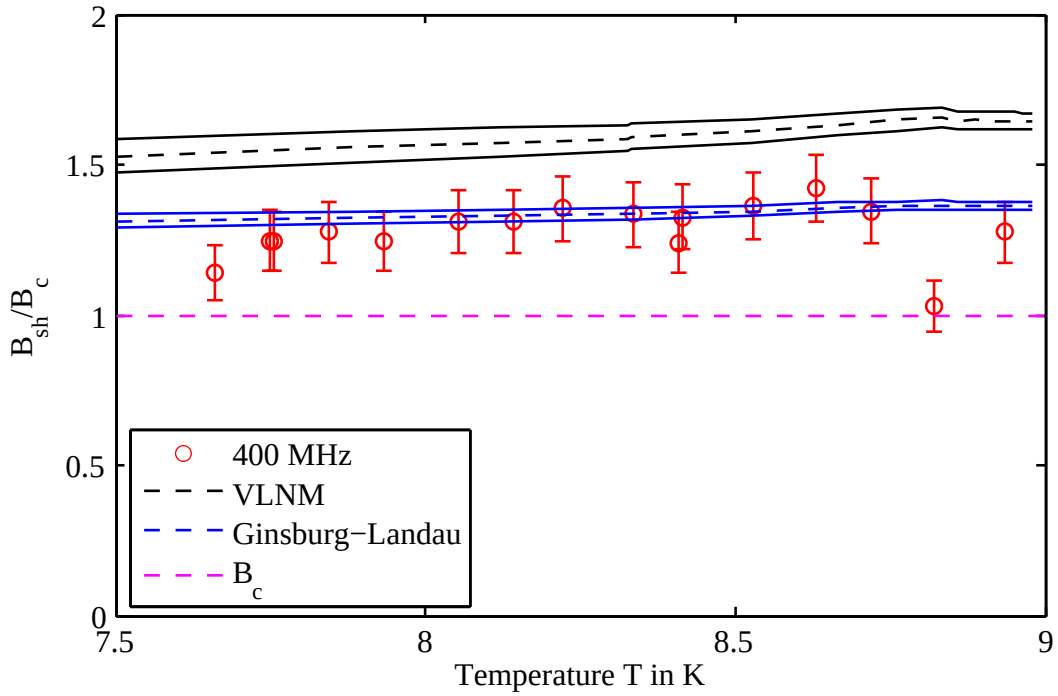

Figure 4.19.: Critical field under RF (short pulses) of the clean bulk niobium sample.

have also been measured in several other publications [91, 143, 144]. The results are explained by a superheating field B_{sh} either derived from considering a metastable state preventing flux entry by a surface barrier [87, 88] or by a thermodynamic energy balance [41, 94, 95]. Figure 4.19 shows the predictions from the vortex line nucleation model (*VLNM*) [95] and the approximate formulas from [88] based on Ginsburg-Landau theory and therefore in the following named the Ginsburg-Landau model (*GLM*). Both models relate the superheating field to the Ginsburg-Landau parameter κ and the critical thermodynamic field B_{c}. The latter

Table 4.11.: Critical RF field of the bulk niobium sample

Measurement technique	Sample condition	f in MHz	$B_{\mathrm{max,RF}}(0)$ in mT	T_{c} in K
CW	dirty	400	102±8	9.14±0.14
CW	dirty	1200	52±3	8.92±0.14
CW	clean	400	216±29	8.91±0.09
CW	clean	1200	101±13	9.16±0.12
Pulsed	clean	400	243±15	9.11±0.06

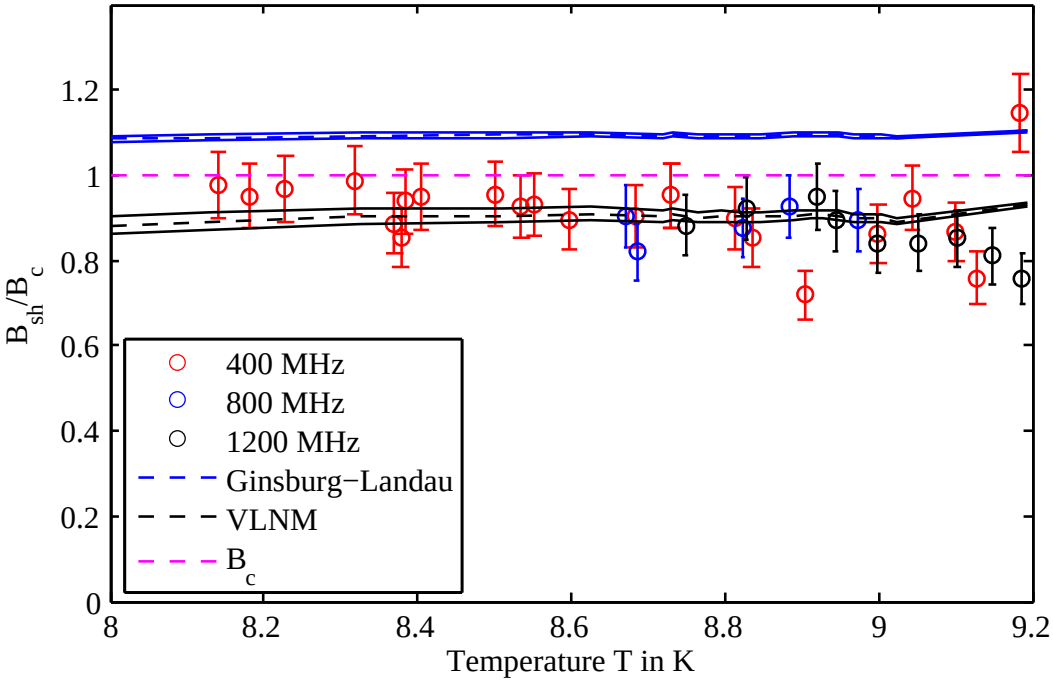

Figure 4.20.: Critical field under RF (short pulses) of the niobium film sample.

parameter was taken from literature, while κ has been calculated from the penetration depth measurements, see Sec. 4.2. The error bands are directly correlated to the uncertainties of κ. For low values of κ (long mean free path) the Ginsburg-Landau model predicts B_{sh} higher than the VLNM. This is the case for the clean bulk niobium sample, for which $B_{\mathrm{max,RF}}$ was measured with values consistent with the Ginsburg-Landau model, see Fig. 4.19.

For high values of κ (low mean free path) the Ginsburg-Landau model predicts B_{sh} higher than the VLNM. High values of κ correspond to the niobium film sample, see Fig. 4.20. For this sample the critical temperature T_{c}=9.28 ±0.03 was found to be consistent with the low field surface resistance measurements. The niobium film is sputtered onto a copper substrate with higher thermal conductivity. That is why the sample temperature is more homogeneous than for the bulk niobium sample. The maximum RF field for this sample does not exceed B_{c}. The values are consistent with the VLNM. For all three frequencies the same value of $B_{\mathrm{max,RF}}$ is found if sufficiently short pulses are used. This shows that the intrinsic critical RF field can be measured with the Quadrupole Resonator.

Conclusions The critical RF field was investigated in CW and pulsed operation. In CW the breakdown field can be explained by an interplay of magnetic and thermal effects supporting the results from Eeremeev et al. [99]. From measure-

ments in pulsed operation the intrinsic critical field could be revealed, because for all three frequencies the same maximum field was found. The results have been compared with predictions from two models, which have been successful in explaining experimental results in previous publications. For material of high purity the Ginsburg-Landau model gives the lower limitation, while for low purity it is set by the vortex-line nucleation model. The former case applies for the bulk niobium and the latter for the niobium film sample. For both samples the lower limitation is met. Therefore, it is possible that both mechanisms set limits to the maximum field under RF in superconducting cavities.

It can however not be excluded that the limitation set by the VLNM can be overcome for cleaner surfaces. It has been stated that for very high values κ this model predicts unrealistic low values for the superheating field [90]. Investigations of the maximum RF field of bulk niobium cavities have been performed by several authors. Measurements on niobium films prepared for superconducting cavities have not been done previously, because usually they are not considered for applications relying on high accelerating gradient. The values for $B_{\mathrm{max,RF}}$ found here are consistent with what one would expect for a bulk niobium cavity with the same RRR value. The conclusion is that cavities coated with films of higher purity should therefore be able to reach accelerating gradients as high as bulk niobium cavities.

4.6. Summary

The surface resistance and the critical RF field were measured using the Quadrupole Resonator. Tested were bulk niobium and niobium thin film on copper substrate samples. For differently prepared samples different loss mechanisms and limitations were observed.

The field dependent surface resistance of clean bulk niobium surfaces was found to be caused by the RF magnetic field. A factorization in a field and temperature dependent part was measured. The critical RF magnetic field $B_{\mathrm{crit,RF}}$ was found to exceed the critical thermodynamic field B_{c} and could be explained by a theoretical superheating field.

For a strongly oxidized niobium film sample $B_{\mathrm{crit,RF}}$ was found to be lower than B_{c}. A thermodynamic energy balance argument yields theoretical values agreeing with the measurement results. For this sample the majority of the non-linear losses are not caused by surface magnetic field, but by the surface electric field. An explanation of these results could be given by a novel interpretation of the interface tunnel exchange model.

5. Surface Characterization

In the previous chapter the surface resistance and critical RF field of superconducting niobium was investigated. Significantly different results were obtained for bulk and thin film samples. In particular, the major contribution to the non-linear losses originated from the RF magnetic field for the bulk niobium and from the RF electric field for the niobium film sample. Even though made from the same material, different manufacturing techniques can yield different surface properties. In this chapter a comparison of grain size, roughness, elasticity and elemental composition is presented. A correlation of these surface properties to the RF results is then made.

5.1. Sample Preparation for Surface Analysis

The Quadrupole Resonator enables to expose samples of 75 mm diameter to an RF field. These flat disks are electron beam welded to cylinders of 110 mm height. For mounting to the host cavity the sample cylinders are vacuum brazed to stainless steel flanges of 152 mm diameter. For the surface analytic measurements presented in this chapter the dissection of the samples was necessary. First, the flat sample disks were cut from the sample cylinders. This enabled to examine them using an optical microscope and by a profilometer based on white light interferometry. For further investigations by scanning electron microscopy (SEM), atomic force microscopy (AFM), ultrasonic force microscopy (UFM) and X-ray photon spectroscopy (XPS) the samples needed to be cut in even smaller pieces of approximately 1 cm^2.

5.2. Imaging

After RF testing and dissection, the samples have first been analyzed by an optical microscope (VEHO VMS-004 deluxe) [145]. Differences in the surface structure of the two samples can be seen in the obtained images. On the left side of Fig. 5.1 one can clearly see the grains on the bulk niobium sample. In principle they can already be recognized without any magnification, since their size is about 1 mm^2. The niobium film sample is found to comprise substructures and holes of several

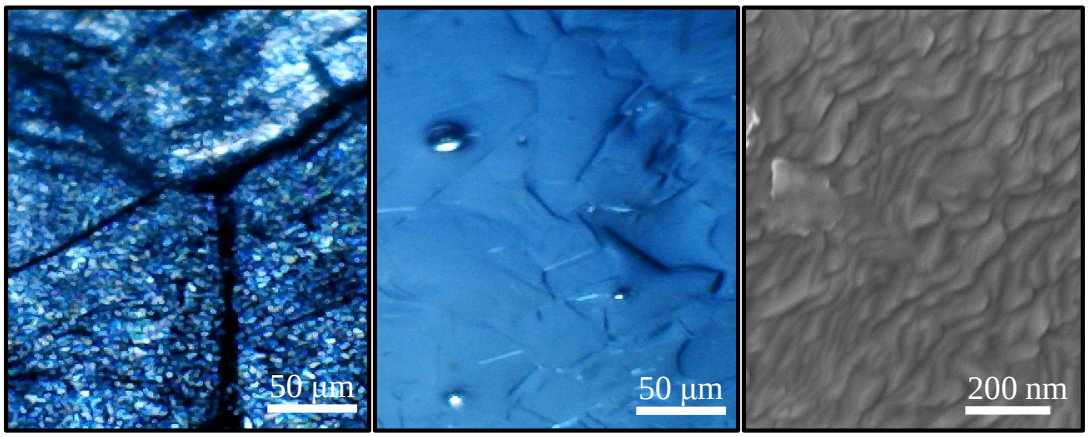

Figure 5.1.: Micrographs of the surface of the bulk niobium (left) and the niobium film (middle) sample obtained with a light microscope. Right: SEM image of the niobium film sample surface. The SEM micrograph has been taken by Ignacio Aviles Santillana (CERN).

tens of micrometers on the film, see Fig. 5.1 (middle). Its grain size is far too small to be measured with an optical microscope. A few tens to hundreds of nanometers are typical for micrometer thin sputter deposited niobium films [146]. In order to resolve the grain structure of this sample a Sigma Zeiss scanning electron microscope [147], available at CERN, was used. SEM images a sample by scanning it with an electron beam in a raster scan pattern. To avoid interaction with other atoms the system is operated under vacuum. There are several techniques and corresponding detectors to analyze the interaction between the electron beam and the sample. The one applied collects low-energy ($<$50 eV) secondary electrons, ejected from the outer orbitals of the sample atoms originating from inelastic scattering with the beam electrons. Figure 5.1 (right) depicts an SEM image of the niobium film sample. Its resolution is 2 nm, high enough to visualize the grains. They have a size of several tens of nanometers and an elongated shape.

5.3. Profilometry

A comparison of the surface profile and roughness of the bulk niobium and the niobium film sample for different scales of observation is the subject of this section. Whether these surface conditions are linked to the RF properties of superconducting cavities is an open issue. Widely discussed and cited in this sense is a model giving an explanation for the Q-Drop by quenching of grain edges [148].

Most of the analytic tools enabling to probe the surface profile and the roughness are designed to cope with sample sizes of a few millimeters. The diameter of

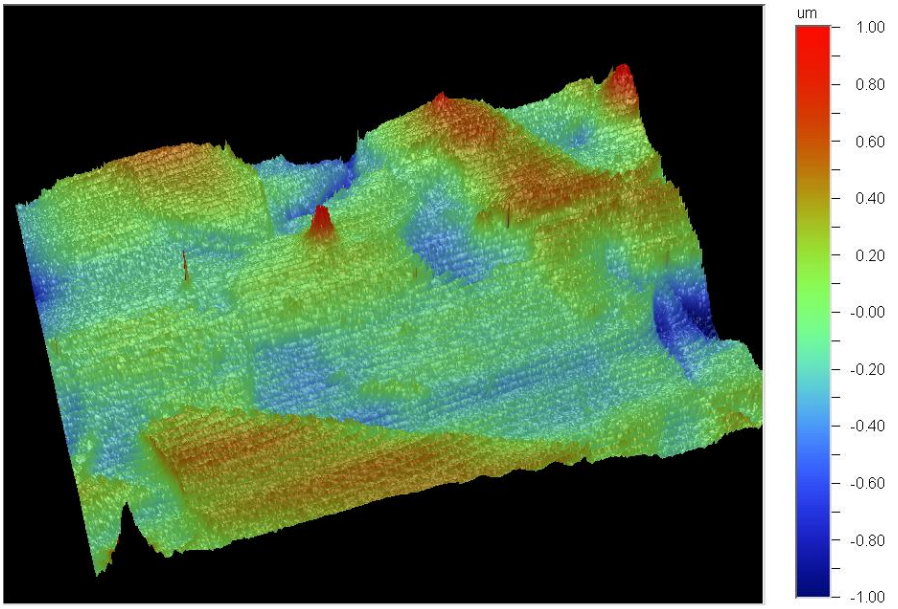

Figure 5.2.: Surface profile of the niobium film sample obtained from white light interferometry. The lateral resolution of the image is 500 nm and the surface area displayed 312 × 234 µm.

the Quadrupole Resonator samples is 75 mm, hence too large for most of these systems. An exception is white light interferometry, a technique allowing contactless profile and surface roughness measurements of relatively large samples. Its operation principle is based on interferometry of light reflected from the sample under investigation. A detailed description of the technique can be found in [149].

A Wyko NT 1100 white light interferometer [150], available at the University of Lancaster, was used to probe the samples. The obtained profiles are depicted in Fig. 5.2 for the niobium film and in Fig. 5.3 for the bulk niobium sample. Note the different vertical scales used. The substructures of the niobium film sample, which could already be seen under the light microscope, have step heights of up to 2 µm and can be identified to originate from the substrate structure, since the film thickness is only about 1 µm.

The bulk niobium sample surface was found to be rougher. Typical values for the average and root mean squared (rms) roughness $R_a(R_q)$ are 200(300) nm for the niobium film and 900(1100) nm for the bulk niobium sample over an area of 312 × 234 µm. The roughness of the niobium film sample can be correlated to the substrate roughness, since similar values of R_a and R_q were found in [151] for chemical polished OFHC copper samples measured with the same white light interferometer. For the bulk niobium sample the measured roughness is typical

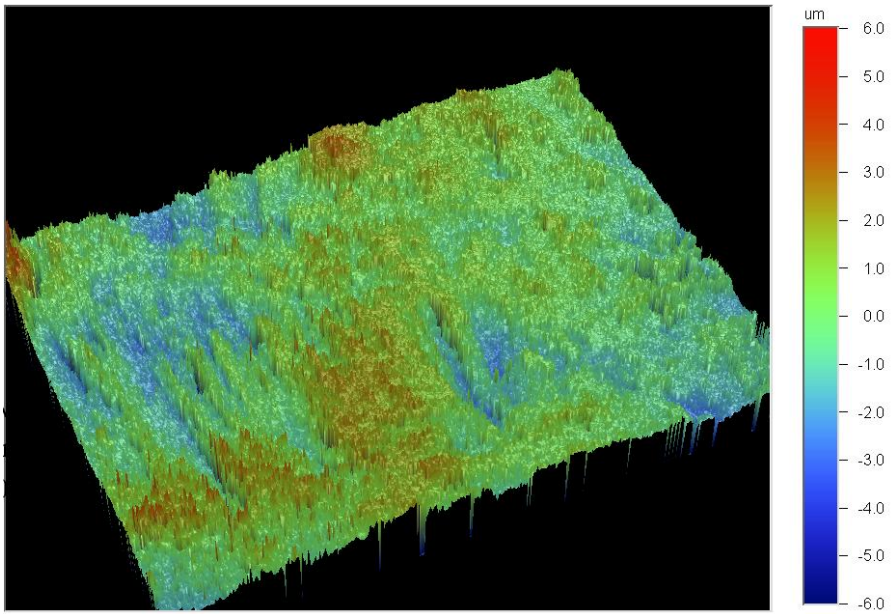

Figure 5.3.: Surface profile of the bulk niobium sample obtained from white light interferometry. The lateral resolution of the image is 500 nm and the surface area displayed 312 × 234 µm.

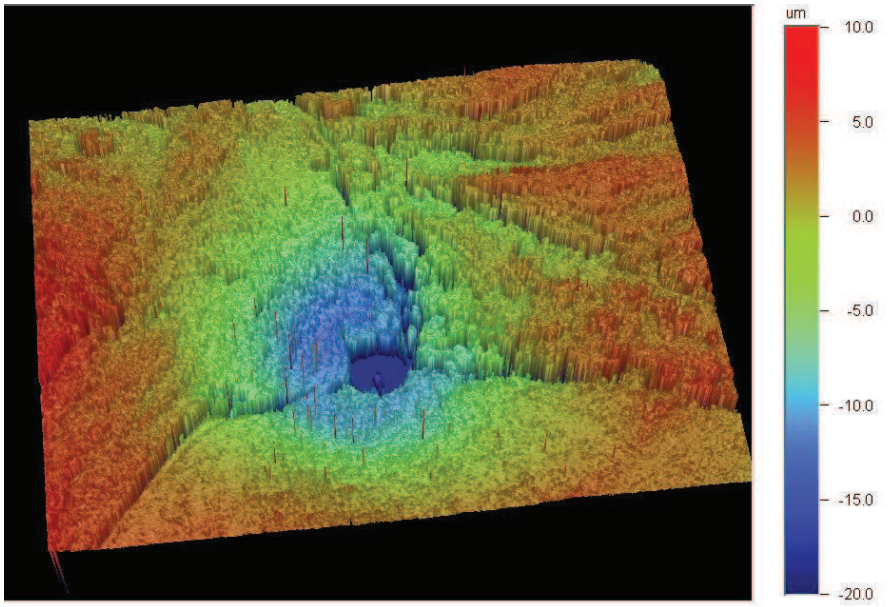

Figure 5.4.: Surface profile of the bulk niobium sample in the vicinity of a boundary between three grains obtained from white light interferometry. The lateral resolution of the image is 500 nm and the surface area displayed 312 × 234 µm.

for surfaces prepared by BCP, compare [113]. In the vicinity of grain boundaries the sample roughness is even higher. At an interface between three grains $R_a(R_q)$=3130(4100) µm was measured. Figure 5.4 shows an image of this surface area.

The lateral resolution of the white light interferometer was 500 nm. Roughness in this scale of observation can be excluded to have a major impact on the surface resistance of the samples being investigated here, since the smoother niobium film sample has a larger residual resistance and also a higher medium field Q-slope. A similar conclusion has been made for the Q-Drop of bulk niobium cavities in [152]. In this study thermometry was used to identify hot and cold spots on single cell cavities. The different samples did not show any difference in roughness, when being investigated by white light interferometry.

However, the length scales describing the RF properties of a superconductor exposed to an RF field (penetration depth λ, coherence length ξ and mean free path l) are in the order of several tens of nanometers. It is intuitive that the roughness might very well depend on the resolution of the applied method and the surface area being investigated. For example the niobium film sample with its small grain size might only appear smoother than the bulk niobium sample as long as the applied method is unable to resolve its grain structure. Therefore imaging and profiling with a higher a resolution method is important to correlate the RF and surface properties of the samples to each other.

Atomic force microscopy (AFM) [154], also called scanning force microscopy (SFM) is a very high-resolution type of scanning probe microscopy. It enables imaging and profiling with a resolution in the nanometer or sub-nanometer scale, more than 1000 times better than the optical diffraction limit. The setup of an AFM is sketched in Fig. 5.5. Its probe is a sharp tip with a radius of curvature of a few nanometers placed on a cantilever. Bringing the tip into proximity of a sample surface, the forces between tip and sample yield a deflection of the cantilever. Typically, the deflection is measured by a laser spot reflected from the top surface of the cantilever onto a quadrant photodiode, decoupling normal and lateral forces.

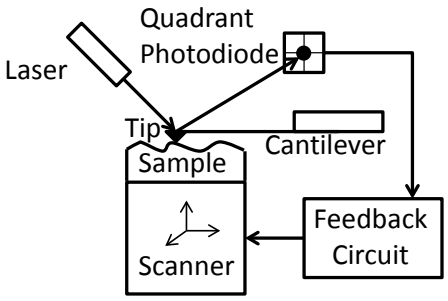

Figure 5.5.: AFM setup following [153].

Here the contact mode was applied, where the cantilever deflection is kept constant by altering the sample position. Two different AFMs, available at Lancaster

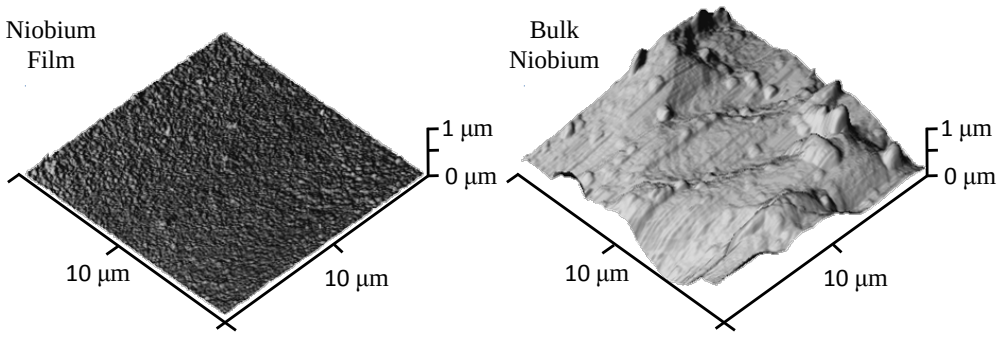

Figure 5.6.: Surface profile of the niobium film (left) and the bulk niobium sample (right) obtained from AFM. The lateral resolution of the pictures is 33 nm.

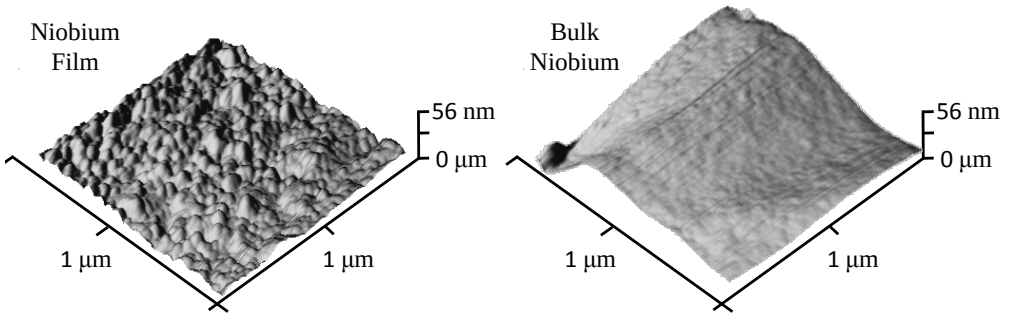

Figure 5.7.: Surface profile of the niobium film (left) and the bulk niobium sample (right) obtained from AFM. The lateral resolution of the pictures is 4 nm. Measurements were done in cooperation with Ilya Grishin (University of Lancaster).

University, were used. The Topometrix TMX 2000 [155] is suited for an observation scale of 10x10 µm. Its lateral resolution is 33 nm comparable to the grain size of the niobium film sample. Figure 5.6 shows AFM-images of the niobium film (left) and the bulk niobium sample (right) obtained with this device. For this scale of observation the average and rms roughness $R_a(R_q)$ are 91(107) nm for the bulk niobium sample and 6.9(14.5) nm for the niobium film sample. Therefore, roughness observed at a 10 times higher resolution compared to the white light interferometry can also be excluded as the major source of non-linear surface resistance and residual losses.

The second AFM system used was a Digital Instruments Multimode [156] capable of even higher resolution. Figure 5.7 depicts AFM-images for a ten times smaller scale (1x1 µm) and a ten times higher resolution (4 nm) compared to Fig. 5.6. The roughness of the bulk niobium and the niobium film sample are of the same order of magnitude for this scale of observation. For the former six different areas were scanned and $R_a(R_q)$=6.7±2.3(8.1±2.5) nm was measured, while for the niobium film sample nine different areas were scanned and $R_a(R_q)$=3.6±0.5

(4.7±0.6) nm was derived. The surface structure of the two samples appears quite different in these images. Like SEM, Fig. 5.7 (left), reveals the grain structure of the niobium film sample. For the bulk niobium sample the surface appears to be smoother, due to the larger grain size. Its surface is curved on a larger scale, which can be correlated to the surface preparation by BCP. This etching procedure is unable to even out such features [113].

5.4. Elasticity

In Sec. 4.4 it has been shown that the non-linear surface resistance of the niobium film sample could only be described by the interface tunnel exchange model. This model was not applicable to the data of the bulk niobium sample. Losses from interface tunnel exchange are caused by oxides localized on the surface at distinct positions, for niobium films preferably along grain boundaries. The Young modulus of Nb_2O_5 was measured to be 125 GPa [157]. This is significantly higher than the value of niobium, 105 GPa [158]. Therefore, mapping the elasticity of the two samples is interesting in order to find out whether there are differences in the oxygen distribution on the surface.

A method capable of this task is ultrasonic force microscopy (UFM) [159]. A UFM is built from an atomic force microscope by mounting the sample to a piezoelectric transducer [160]. By applying an alternating voltage to the transducer the sample is vertically vibrated at a frequency above the cantilever's primary resonance, increasing its effective spring constant due to inertia. The cantilever cannot follow the oscillation. This yields a constant feedback error signal, as long as tip and sample are in contact. Modulating the oscillation in amplitude allows to derive the threshold where contact is lost, from a change in the feedback error signal. In practice this signal is transmitted to a lock-in amplifier as input, while the amplitude modulation frequency is used as the reference. The lock-in amplifier only gives a signal if the contact between sample and cantilever is lost. For a stiffer or less adhesive sample the threshold amplitude is lower and therefore the lock-in amplifier output larger. The convention for UFM images is to use a brighter color for a higher lock-in amplifier output corresponding to a stiffer or less adhesive sample [153].

Built upon an AFM, UFM also provides information about the topography and the lateral force. While the former gives an AFM image, the latter is used to distinguish between elastic and adhesive forces. In general the elastic forces are dominant [160] and for the forces applied in the nN-range, plastic deformation was never observed, at least in the AFM resolution limit [153].

Figure 5.8 displays UFM images of the same sample areas as depicted for AFM in Fig 5.7. The AFM images, where taken simultaneously, exploiting the fact, that

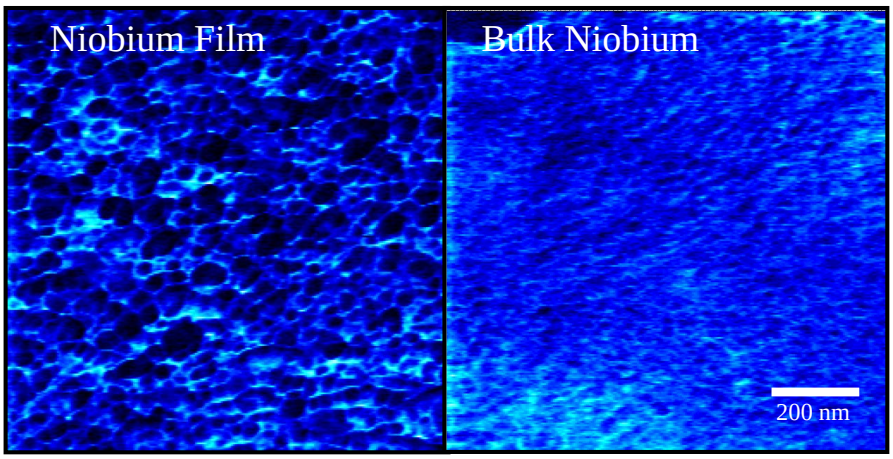

Figure 5.8.: UFM images of the niobium film (left) and the bulk niobium sample (right). A dark (light) color indicate areas of low (high) stiffness. The lateral resolution of the pictures is 4 nm and the surface area displayed is 1x1 µm for each sample. The same surface areas as in Fig. 5.7 are displayed here. Measurements were done in cooperation with Ilya Grishin (University of Lancaster).

UFM also gives the topographical information. The lateral forces were found to be homogeneously distributed on both samples. Therefore the contrast is not caused by adhesive forces and is unlikely due to topographical artifacts. This allows for the interpretation that the images display the Young modulus as a function of position on the sample surface, where a larger Young modulus (stiffer material) corresponds to a brighter color. The values obtained must be interpreted relatively with respect to each other. The test setup used does not enable to give a quantitative value of the Young modulus.

The structure of the bulk niobium sample appears more uniform compared to the niobium film. The softer (darker) regions of the latter can be correlated to single niobium grains. Their size is consistent with the AFM and SEM pictures. Around the grains are stiffer (brighter) areas caused by oxidation preferably located along the grain boundaries. This explains why losses from interface tunnel exchange are the dominant mechanism of this sample and why these are negligible for the bulk niobium sample.

If the hypothesis that the contrast is caused by oxidation is correct, the material appears uniform, if not the surface but a layer deeper in the film, protected from oxidation is investigated. Therefore, argon ion beam cross-section polishing [161] was used to remove material from the sample, creating a cross section tilted about 10 degrees with respect to the sample surface, see Fig. 5.9. On the left side of this figure an UFM image of the oxidized sample surface right next to the section is displayed. About 300 nm (middle) from the sample surface the structure appears more uniform and even more so at the interface between the niobium film and the

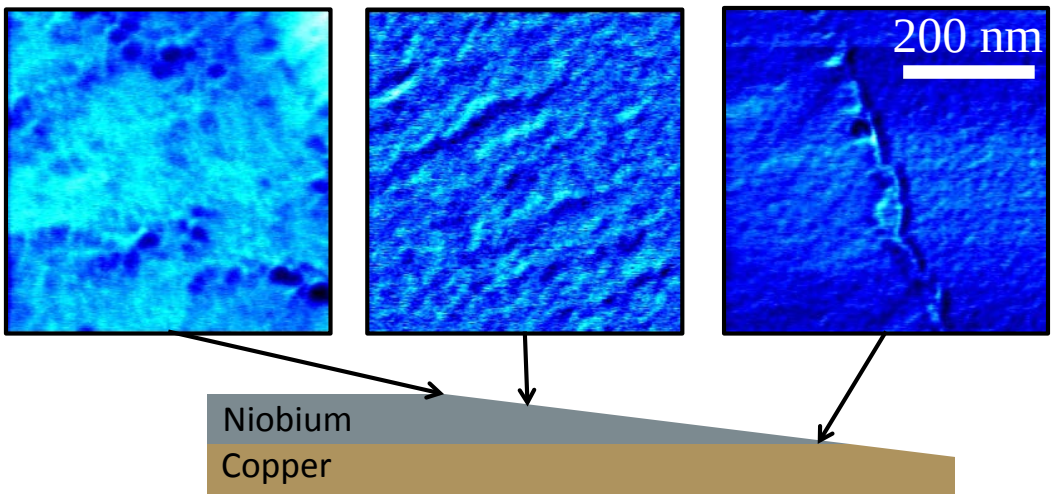

Figure 5.9.: UFM images of a cross section of the niobium film sample. Measurements were done by Ilya Grishin (University of Lancaster).

copper substrate (right), which can be clearly seen in the image.

5.5. Elemental Composition

It is well known that niobium is a reactive material [162]. When exposed to normal air, which is unavoidable during preparation, it immediately oxidizes, forming an oxide layer of 1 nm thickness within a few minutes. The thickness of this layer saturates at approximately 6 nm for longer oxidation time. These dielectric oxides are coated with a sorption layer of 0.5-3 nm containing oxygen and carbon. Impurities originating from the manufacturing process or the chemical treatment might also be found, for example, hydrocarbons from cleaning with alcohol [163, 164]. The effect of the different layers and residues, on the RF properties, especially on the surface resistance, is not well known. A comparison of the elemental composition of the first few nanometers could give further insight in the differences between cavities produced from bulk niobium and niobium films.

The bulk niobium sample investigated here was built from a niobium sheet. Forming the sheet involves several fabrications steps like cutting, grinding and rolling. One major difference in the production process was that the bulk niobium sample was buffered chemically polished, before the final rinsing, while no treatment was performed on the niobium film sample between deposition and final cleaning.

A tool enabling to provide information about the elemental composition for all elements except for H and He is X-ray Photoelectron Spectroscopy (XPS). It uses

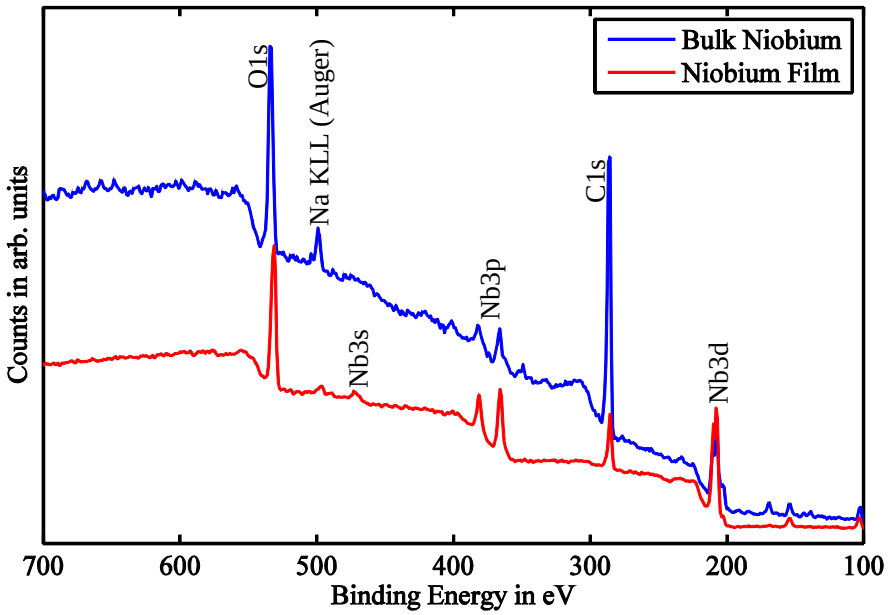

Figure 5.10.: XPS spectra of the bulk niobium and the niobium film sample. Measurements were done by Paul Unsworth (University of Liverpool).

an X-ray beam of usually 1-2 keV to irradiate the sample under investigation. The electrons knocked off from the sample have a kinetic energy

$$U_{\mathrm{kin}} = h\nu - U_{\mathrm{b}}, \tag{5.1}$$

where $h\nu$ is the incident photon energy and U_{b} the binding energy of the knocked-off electron. The photon energy is determined by the XPS system, while the values of U_{b} can be taken from literature. For the analyses here the U_{b} values were taken from the NIST database [165] to derive the elemental composition from the measured spectra.

Figure 5.10 shows XPS spectra for the niobium film and the bulk niobium sample. They were measured with a system at the University of Liverpool, using an Al K-α X-Ray source with a photon energy hν=1486.6 eV [166]. This corresponds to an information depth of approximately 7 nm, covering the oxide and the oxide/metal interface.

The major difference in the two spectra is a larger oxygen to carbon ratio found for the niobium film sample. This result is expected. The niobium film sample was kept under normal air for 11 years, while the bulk niobium sample was only exposed to normal air for a few hours after etching, for rinsing and mounting to the Quadrupole Resonator. Carbon hydrides quickly form a monolayer on a niobium surface but do not react with the niobium metal unlike oxygen [162]. The

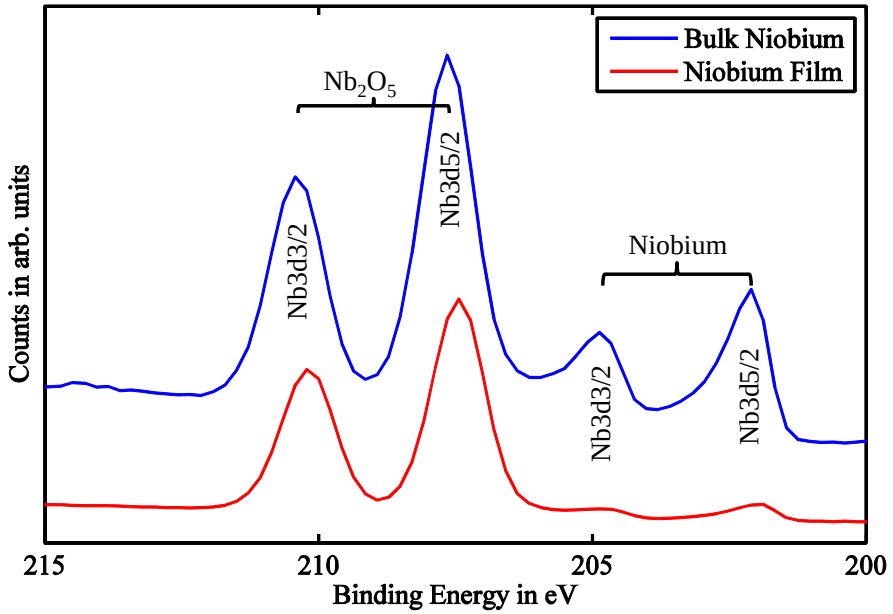

Figure 5.11.: High resolution XPS spectra of the bulk niobium and the niobium film sample. Measurements were done by Paul Unsworth (university of Liverpool).

ratio between oxygen and carbon can therefore be used to compare the grade of oxidation of the two samples.

There is no element only found for the niobium film sample, which could explain the weaker RF properties of this technology. However it must be stated that XPS, with its resolution of approximately 0.1-1 atomic percent is not sensitive enough to detect impurities. Both samples show a sodium peak and small silicon peaks for lowest binding energies. These originate from holders to which the samples were mounted for the measurement.

For the investigation of the niobium oxide structure a spectrum with a higher resolution (about 5 measurements per eV) was obtained, see Fig. 5.11. The ratio between the niobium oxides and the metal is larger for the niobium film, confirming the stronger oxidation of this sample.

5.6. Summary

White light interferometry and atomic force microscopy showed that the niobium film sample with the weaker RF properties has a smoother surface than the bulk niobium sample. This allows the exclusion of roughness as the cause for the residual and the non-linear surface resistance. The spatial distribution of the elasticity was probed with ultrasonic force microscopy. The elasticity of the bulk niobium

sample is more uniform than it is for the niobium film sample. Stiffer areas on the latter have been identified to be oxides along grain boundaries, which are responsible for RF losses caused by interface tunnel exchange (ITE). The uniform oxide distribution on the bulk niobium sample explains why ITE losses were not measured for this sample. The elemental composition was examined by X-ray photon spectroscopy. The major difference observed was a higher oxygen to carbon ratio on the niobium film sample, indicating stronger oxidation. A high Nb_2O_5 concentration was found for both samples, while the ratio between Nb_2O_5 and niobium metal was larger for the niobium film sample. The presence of Nb_2O_5 supports the interpretation of the ultrasonic force microscopy measurements and their correlation to the RF results from Sec. 4.4: The stronger Q-slope of sputter deposited niobium film - in comparison to bulk niobium cavities is correlated to the smaller grain size and higher Nb_2O_5 content. This surface structure causes additional RF losses from interface tunnel exchange between the superconducting material and Nb_2O_5 formed along grain boundaries.

6. Summary and Outlook

Refurbishment and extension of the Quadrupole Resonator In 1997 the Quadrupole Resonator was designed to measure the surface resistance of sputter coated niobium film samples at 400 MHz, the technology and RF frequency chosen for the Large Hadron Collider at CERN. For the studies presented in this thesis it has been refurbished and its measurement capabilities have been extended to 800 and 1200 MHz. It has been demonstrated that the device is also suited to probe the intrinsic critical RF magnetic field. The calorimetric results were compared with independent 3 dB bandwidth measurements for a sample in normal conducting state. The excellent agreement of the results verifies the calorimetric approach and therefore also gives confidence in the measurements at lower temperatures. For the next test, which marks the starting point of a new PhD project, the Quadrupole Resonator has been equipped with a coil placed inside the thermometry chamber. This allows to measure the frequency dependence of losses caused by trapped flux and to reveal the underlying loss mechanism. This new setup will first be tested on a bulk niobium sample. Afterwards the Quadrupole Resonator shall be used to investigate materials other than niobium, which could potentially have a lower surface resistance and/or a higher critical RF field, such as Nb_3Sn, MgB_2 or multilayers of super and normal conducting materials.

Non-linear surface resistance There are several models explaining how the surface resistance depends on the applied RF field strength. In this work these have been reviewed and arguments were presented whether or not they can account for differences observed between bulk niobium and niobium film cavities. Samples of these materials have been investigated with the Quadrupole Resonator and the results have been compared with predictions from the models. It was shown that the RF electric field dominates the losses for strongly oxidized niobium films, via interface tunnel exchange (ITE) of electrons between the superconductor and localized states in adjacent oxides. After subtraction of losses caused by the RF magnetic field, it was shown that the measured electric surface resistance is almost independent of temperature and scales linearly with frequency. It vanishes below a threshold field and saturates at higher fields at which all localized states participate in the exchange. All these observations are predicted by the ITE model.

Identifying ITE to be responsible for RF losses in the low and intermediate field

region allows optimizing the development of superconducting cavities. The surface resistance can be significantly lowered if extended periods of oxidation are avoided. ITE is caused by crack corrosion along grain boundaries and is therefore more pronounced for sputter coated niobium films, which have in general smaller grain size and higher oxygen content compared to bulk niobium cavities. There are two ways to minimize these losses. One could either reduce oxidation or produce coating resistant to crack corrosion along grain boundaries. The latter could be achieved by High Impulse Magnetron Sputtering (HIPIMS) [167]. The investigation of HIPIMS samples was planned to be performed with the Quadrupole Resonator in the framework of this thesis [168]. The bulk niobium sample used in this study was coated after one RF test. Unfortunately the film peeled off during rinsing with ultrapure water. It was shown that the films have these adhesion problems only when deposited on a niobium, but not onto a copper substrate. Therefore, future tests of HIPIMS samples with the Quadrupole Resonator will rely on copper substrate samples, which are currently prepared. The investigations of the HIPIMS coating technique are performed at CERN with the aim of exploitation for the SPL study and for LHC spare cavities. Avoiding oxidation in elliptical cavities is rather simple. If produced from thin films they can be put in a nitrogen atmosphere after deposition. For bulk niobium this should be done after chemical etching. For rinsing the cavities obviously need to be exposed to normal air, but the time should be kept as short as possible to avoid crack corrosion. For quarter wave resonators such as HIE-Isolde it is not as simple to avoid oxidation as for elliptical cavities, and additional precautions are advisable. Recent measurements on one of these prototype cavities showed large losses from ITE, confirming the Quadrupole Resonator measurements.

The ITE loss mechanism is negligible for well-prepared bulk niobium surfaces, even if they are coated by a natural grown oxide layer. This surface layer of several nanometers is only responsible for rather small residual losses. For well-prepared bulk niobium surfaces it has been shown that the RF losses are caused by the magnetic field and factorize into field and temperature dependent parts. This factorization rules out several models for the field dependent surface resistance. In particular it cannot be explained by pair-breaking in the current carrying state, global thermal feedback or localized heating at hot spots. The origin of the magnetic non-linear surface resistance is still not completely understood. Additional experiments, especially at very low temperatures, on samples or cavities with low residual resistance need to be carried out to make further conclusions.

Critical RF magnetic field The critical RF magnetic field has been measured in continuous wave (CW) operation and with short pulses. When measured in CW, the field levels and frequency dependency found was explained by a local

defect causing the quench, when the adjacent superconducting material exceeds the temperature dependent critical RF magnetic field. Measured in pulsed operation the intrinsic critical RF magnetic field was revealed. It was confirmed to be larger than the critical thermodynamic field for the bulk niobium sample and consistent with predictions for a superheating field derived from Ginsburg-Landau theory. For the niobium film sample the maximum field is lower and can be explained by a thermodynamic energy balance, vortex line nucleation model. Its value is consistent with what one would expect for a bulk niobium sample of the same purity. It was shown that for low purity material the vortex line nucleation model predicts a lower critical RF field than the Ginsburg-Landau model, while for a surface of high purity the latter model sets the lower limitation. For the surfaces investigated here it was found that the samples were always limited by the lower barrier. Therefore both mechanisms can set limitations to the maximum attainable RF magnetic field.

Surface Properties The study was accompanied by measurements of the surface properties of the samples by various techniques. The major difference between the bulk niobium and the niobium film sample was a less uniform elasticity of the latter. This was correlated to crack corrosion along grain boundaries on the niobium film sample, which is the origin of losses due to interface tunnel exchange. It explains why these losses were only measured for the stronger oxidized niobium film with the smaller grain size. X-ray photoelectron spectroscopy (XPS) measurements confirmed the presence of Nb_2O_5 responsible for these losses. An interesting future study could be to perform XPS and UFM measurements on samples of different grain size. One should start with unoxidized samples and then measure how oxidation changes the uniformity of the elasticity. This would allow confirming that crack corrosion is favored along grain boundaries and causes ITE losses. If confirmed, UFM could be used as a standard tool in the development of thin film cavities. The coating procedures could be optimized towards producing films resistant to crack corrosion.

Suggestions for future investigations

- Measuring the temperature dependence of the onset field E_0 in the ITE model to confirm its role for the nonlinear surface resistance. For temperatures close to the critical temperature, E_0 should decrease, since the superconducting energy gap decreases with temperature. The Quadrupole Resonator is the ideal instrument for these tests, due to its wide temperature range and the frequency dependent ratio between electric and magnetic surface fields.

- Study of HIPIMS coatings. This technique could potentially give coatings resistant to crack corrosion and yield surfaces with negligible ITE losses. This might be the key towards producing thin film cavities with equal RF properties as bulk niobium.

- Consider the systematic use of XPS and UFM in the development of future coatings. With these two methods combined one can identify coatings resistant to crack corrosion.

- Comparison of Type I and II superconductors. The origin of the magnetic non-linear surface resistance requires further experimental and theoretical studies to be fully understood. A systematic study on type I and type II superconductors can help to reveal loss mechanisms, which might only be relevant in the Shubnikov phase. Testing a sample made of lead with the Quadrupole Resonator is therefore suggested.

- Determining additional surface treatments. For example, in cavity tests it is suggested to measure the surface resistance always at lowest and highest available temperature. This allows for convenient separation of the electric and magnetic losses. Possible additional surface treatments can be performed accordingly.

A. Thermal Conductivity Measurements

In addition to the RF parameters, surface impedance and critical RF field, the thermal conductivity k of the attached sample can be directly measured with the Quadrupole Resonator. For this purpose the thermometry chamber allows to place up to eight temperature sensors at different distances from the DC heater (resistor). Four sensors are placed directly under the sample disk. They are circularly arranged around the heater and displaced by 90° with respect to each other. Two of them can be seen in the cross-sectional view, Fig. A.1 (left). When a current is applied to the heater, these four sensors should all measure the same temperature if the thermal conductivity of the sample is uniform. Up to four additional sensors can be placed in pistons and pressed against the inner wall of the sample cylinder. Thermal contact is established using Apiezon® N grease. In order to derive $k(T)$ the power applied to the heater on the back side of the sample is changed, while the temperature at the different positions is measured.

This technique is only able to derive k for the bulk material. For the niobium film sample the measurement would only give k for the substrate, but not for the thin film. Furthermore, the sample cylinder must be made of the same material as the sample disk or the value of k must be known for the sample cylinder. In case of the bulk niobium sample, cylinder and disk are made of niobium from the same batch, making this measurement technique applicable.

Figure A.1 (right) displays k for this sample as a function of temperature. The data can be approximated by a polynom of 3$^{\text{rd}}$ order. This allows to calculate the thermal conductivity at 4.2 K. The value found (13±2 W/mK) enables to derive RRR from the relation [16],

$$RRR = 4 \cdot k(4.2\,\text{K}). \tag{A.1}$$

The mean free path l can be obtained from Eq. (4.5) and the Ginsburg-Landau parameter κ is related to l via Eq. (2.45). All material parameters derived from the thermal conductivity are presented in Tab. A.1. The values are consistent with the results from the penetration depth measurements and lower than the ones derived from the normal conducting surface resistance. The difference of this method is that not only a surface layer of the sample disk is probed but the bulk material of

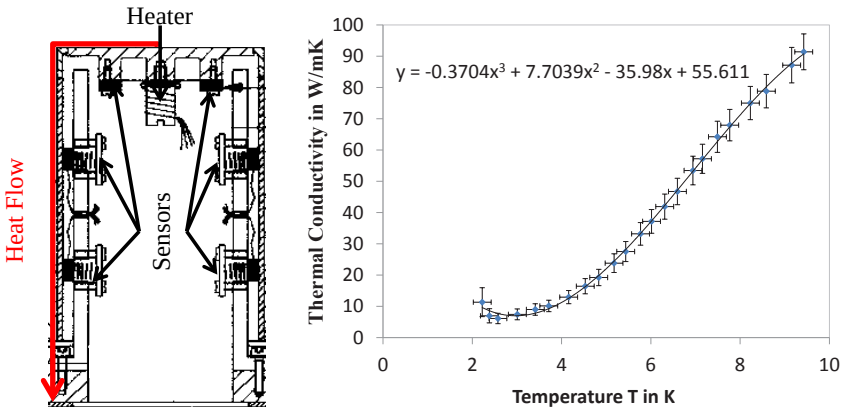

Figure A.1.: Left: Heat flow along the sample surface and the sample cylinder and position of heater and temperature sensors inside the thermometry chamber of the Quadrupole Resonator. Right: Thermal conductivity of the bulk niobium sample as a function of temperature.

sample disk and cylinder.

Table A.1.: Material parameters of the bulk niobium sample derived from thermal conductivity measurement

k at 4.2 K in W/mK	RRR	l in nm	κ at 4.2 K
13±2	52±8	140±22	1.08±0.06

B. Field Limitations of Superconducting Cavities

B.1. Multipacting

Multipacting is a resonant process where an electron emitted from the surface of a cavity, for example by a cosmic ray, is accelerated by the RF field. When the particle impacts the surface again it produces secondary electrons. The secondaries are accelerated as well and produce further secondaries. A resonant process starts, where the number of impacting electrons increases exponentially. The mean amount of secondary electrons released from one impact is the secondary electron coefficient (SEC) δ, depending on the surface material and the impact energy of the primary electron. Figure B.1 displays δ as a function of the impact energy for a generic material. At low energy the impacting electron loses all its energy within a thin surface layer of the material. Here the number of charges, the primary electron interacts with, is proportional to its impacting energy and δ is increasing with the energy of the impacting electron until a few 100 eV. An impacting electron of higher energy penetrates deeper into the material, interacting with electrons, which then are unable to escape the bulk. This yields a decrease of δ for higher impact energies, see Fig. B.1 (right). For energies above approx. 1000 eV, δ usually becomes lower than one [16].

Obviously multipacting can only occur if δ is larger than one and the electrons gain enough energy to produce secondary charges. A common multipacting scenario is when an electron returns to its origin after n impacts. These scenarios are referred to as n-point mulipacting [16].

The most frequent type of multipacting in superconducting cavities used to be one point multipacting. Emitted electrons are accelerated by an electric field perpendicular to the cavity's surface, while the magnetic field forces the charges on quasi cyclotron orbits. After m RF periods the charges impact the wall, while they have gained enough energy to release secondaries [16].

If one-point multipacting of order m is to occur, the cyclotron frequency ω_c needs to equal a multiple integer of the cavity's drive frequency ω_g

$$\omega_g = m\omega_c. \tag{B.1}$$

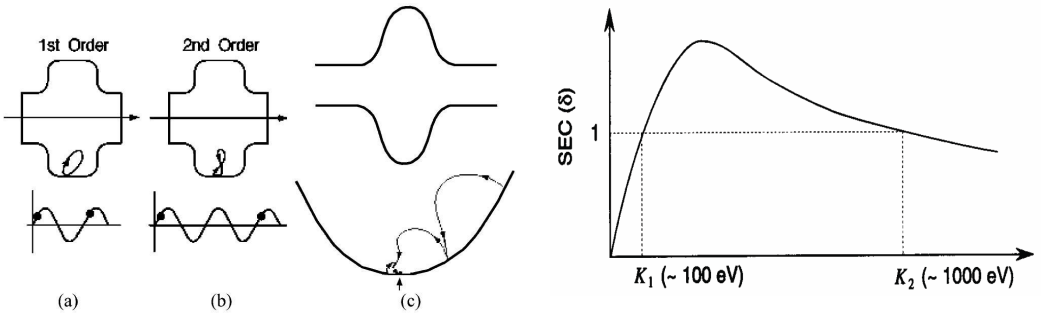

Figure B.1.: Left: One point multipacting of order 1 (a) and 2 (b). When the cavity shape is rounded, the electrons drift to the equator. Here the electric field almost vanishes and secondaries cannot gain enough energy to regenerate (c). Right: Secondary emission coefficient (SEC) of a generic material (δ) as a function of impact kinetic energy K. Reproduced from [16]

Figure B.1 (left) displays one point multipacting trajectories of order 1 (a) and 2 (b). The most successful solution to overcome one point multipacting is to round the cavity wall. In a rounded shape the magnetic field varies along the whole surface and no stable trajectories are possible. Electrons drift to the equator, where the electric field almost vanishes. Here multipacting ends because electrons do not gain enough energy to generate secondary charges, see Fig. B.1 (c). Therefore, in elliptical cavities one-point-multipacting is not an issue anymore. Two point multipacting may still occur but is rather rare. This scenario is more common in other RF components such as coaxial lines, couplers, heavy ion cavities or parallel plate geometries [16].

For parallel plate arrangements possible multipacting areas can be identified by analytical methods [169]. One point-multipacting can be treated with a semi analytical approach. After the electromagnetic fields in the structure are calculated by a computer code, dangerous areas can be identified from the ratio of electrical and magnetic field [170]. To identify multipacting scenarios with more than one impact site tracking codes are required. Two dimensional structures can be analyzed with a widely used dedicated multipacting code [171]. For three dimensional structures codes not exclusively designed for multipacting problems, like CST Particle Studio® [172] can be used.

B.2. Field Emission

The surface electric field can limit the maximum accelerating gradient of a superconducting cavity by field emission. Under normal conditions electrons inside a metal are unable to escape due to an electrostatic potential well. An electric field E applied on the surface of the metal can lower the work function Φ allowing

electrons to tunnel the potential well.

The theory of field emission has been worked out by Fowler and Nordheim [173]. They derived a relation for the current of the tunneling electrons

$$I(E) = \frac{K_1 A_e E^2}{\Phi} \exp\left(-\frac{K_2 \Phi^{3/2}}{E}\right), \tag{B.2}$$

where A_e the effective emitting area and K_1 and K_2 are the Fowler Nordheim parameters. Emitted electrons are accelerated by the electric field inside the cavity and when they impact the wall, bremsstrahlung will occur. To explain the measured X-ray intensities Eq. (B.2) had to be modified by a field enhancement factor β_{FN}. Substituting E with $\beta_{FN}E$ yields

$$I(E) = \frac{K_1 A_e (\beta_{FN} E)^2}{\Phi} \exp\left(-\frac{K_2 \Phi^{3/2}}{\beta_{FN} E}\right). \tag{B.3}$$

Field enhancement factors for different shapes have been calculated but whiskers or contaminations, which could explain enhancement factors agreeing with the measured X-ray intensity, are usually not found. Field emission from contaminations therefore has to be explained by a Tip-on-Top Model. According to this model a particle enhances the field by a factor β_1, while a smaller protrusions on the particle further enhances the field by a factor β_2 yielding a total enhancement factor of $\beta_1\beta_2$ [16].

On the surface of a superconducting cavity there are approximately 100 particles per cm^2 with a size between 0.3 and 20 µm. 10% of these particles are field emitters between 20 and 100 MV/m [16]. Small regions of emitting particles can sometimes be melted when the energy in the cavity is raised for the first time. Other particles can be processed. If the repulsive force due to the surface electric field becomes stronger than the adhesive force binding the particle to the surface, field emission can be stopped. Since field emission is usually caused by contaminations and not by whiskers on the surface chemical etching may be harmful to the performance, because during the process further particles could be placed on the cavity surface. Field emission can be suppressed by high pressure rinsing, what is nowadays routinely applied to superconducting cavities [174].

Symbols

a	defect radius
A	(generic) area
$\vec{B}$	magnetic induction also called magnetic field
B^*	in percolation model: threshold field for gradual flux entry
B_{b0}	in hot spots model: quench field in the absence of defects
B_{c}	critical thermodynamic field
B_{c1}	lower critical field
B_{c2}	upper critical field
$B_{\mathrm{crit,RF}}$	critical RF magnetic field
B_{ext}	external magnetic field
B_{p}	peak magnetic field on surface
B_{sh}	superheating field
B_{th}	in percolation model: threshold field for entry of complete flux tubes
c	speed of light in vacuum
c_1, c_2, c_3	Quadrupole Resonator field constants
d	in interface tunnel exchange model: thickness of Nb_2O_5 layer
e	electron charge
E	electric field
E_{F}	Fermi energy
E^0	in interface tunnel exchange model: threshold field for losses caused by this process
f	frequency
f_0	resonant frequency of the TM_{010}-mode
f_c	cyclotron frequency
f_g	generator frequency
g	in hot spots model: parameter related to the number and intensity of hot spots

G	geometry factor
G_{Sample}	(magnetic) geometry factor of the Quadrupole Resonator sample
$G^{\mathrm{E}}_{\mathrm{Sample}}$	electric geometry factor of the Quadrupole Resonator sample
h	Planck constant
$\vec{H}$	magnetic field strength
k	thermal conductivity
k_{B}	Boltzmann constant
K	kinetic energy
K_{m}	modulation constant
K_0	Bessel function of the second kind of order 0
K_1, K_2	Fowler-Nordheim parameters
l	electron mean free path also only referred to as mean free path
n	density of thermally activated normal conducting electrons
p_{F}	Fermi momentum
P	power
P_{RF}	power dissipated by RF
P_{DC1}	DC power applied to sample with the RF off
P_{DC2}	DC power applied to sample with the RF on
Q_0	unloaded quality factor
Q_{c}	quality factor of the Quadrupole Resonator without losses on the sample
Q_{ext}	external quality factor, describing the power coupled out through the antennas
Q_{L}	loaded quality factor
Q_{Sample}	quality factor of the Quadrupole Resonator sample
r	(generic) radius
R_{a}	average roughness
R_{BCS}	contribution of thermally activated normal conducting electrons to the surface resistance
R_{lin}	field independent (magnetic) surface resistance
R_{nl}	field dependent (magnetic) surface resistance
R_{q}	rms roughness
R_{res}	residual resistance
$R_{\mathrm{res,fl}}$	residual resistance caused by trapped magnetic flux

R_{res1}	in percolation model: field dependent residual surface resistance
R_{res2}	frequency independent residual resistance
R_{N}	normal conducting surface resistance
R_{S}	magnetic surface resistance, also only referred to as surface resistance
$R_{\mathrm{S}}^{\mathrm{E}}$	electrical surface resistance
R^2	coefficient of determination
RRR	residual Resistance Ratio
S	generic surface
t	time
T	temperature
T'	in percolation model: percolation temperature
T_{b}	bath temperature
T_{c}	critical temperature
U	energy
U_{f}	forward (incident) voltage
U_{r}	reflected voltage
U_{t}	transmitted voltage
v_{c}	critical velocity
v_{s}	superfluid velocity
V	(generic) volume
Z_H	complex surface impedance
α	decay constant
β	coupling constant
β_{FE}	field enhancement factor
γ	Q-slope parameter
Δ	superconducting energy gap also only referred to as energy gap
Δx	in percolation model: penetration depth of non linear surface resistance
Δy	penetration depth of residual resistance
ε_0	vacuum permittivity
ε	relative permittivity
ϵ	energy of a flux thread inside a superconductor far away from the surface
ϵ_i	relative residuals
κ	Ginsburg-Landau parameter

λ	penetration depth
λ_0	penetration depth at 0 K
λ_L	London penetration depth=penetration depth for infinite mean free path at 0 K
λ_w	wavelength
μ_0	vacuum permeability
ξ	coherence length
ξ_0	BCS coherence length
ξ_GL	Ginsburg-Landau coherence length
σ	normal state conductivity at the transition temperature T_c
σ_0	normal state conductivity at room temperature
τ	decay time
Φ	work function
Φ_0	flux quantum
φ	phase difference
ρ_s	superfluid density
ω	angular frequency $2\pi f$

List of Tables

List of Figures

Bibliography

[1] H. Padamsee, *RF superconductivity: Science, Technology, and Applications*, Wiley, New York, NY, 2009.

[2] D. Reschke, Challenges in SRF Module Production for the European XFEL, in *Proceedings of the 15th International Workshop on RF Superconductivity, Chicago, Ill., USA*, 2011.

[3] M. Lindroos, The ESS Accelerator, in *Proceedings of the 15th International Workshop on RF Superconductivity, Chicago, Ill., USA*, 2011.

[4] M. Pasini, S. Calatroni, O. Capatina, A. D'Elia, M. Fraser, and M. Therasse, HIE-Isolde quarter wave Nb/Cu cavity, in *Proceedings of the 15th International Workshop on RF Superconductivity, Chicago, Ill., USA*, 2011.

[5] A. Yamamoto, Advances in SRF Development for ILC, in *Proceedings of the 15th International Workshop on RF Superconductivity, Chicago, Ill., USA*, 2011.

[6] O. Capatina, S. Atieh, I. A. Santillana, G. A. Izquierdo, S. Calatroni, T. Junginger, V. Parma, T. Renaglia, T. Tardy, N. V. Alonso, W. Weingarten, S. Chel, G. Devanz, and J. Plouin, Mechanical Design Considerations for β=1 Cavities, in *Proceedings of the 15th International Workshop on RF Superconductivity, Chicago, Ill., USA*, 2011.

[7] C. Poole, *Handbook of superconductivity*, Academic Press, London, 2000.

[8] J. R. Delayen, G. J. Dick, J. E. Mercereau, J. W. Noe, P. Paul, and G. D. Sprouse, *IEEE Transactions on Nuclear Science* **26**, 3664 (1979).

[9] N. R. Lobanov, D. C. Weisser, T. Kibedi, D. Anderson, A. Cooper, D. Gibson, J. Heighway, A. Muirhead, and R. Turkentine, Superconducting RF activities at ANU, in *Proccedings of the 10th Workshop on RF Superconductivity, Tsukuba, Japan*, 2001.

[10] V. Palmieri, New Materials for Superconducting Radiofrequency Cavities, in *Proceedings of the 10th Workshop on RF Superconductivity, Tsukuba, Japan*, 2001.

[11] A. Gurevich, *Applied Physics Letters* **88**, 012511 (2006).

[12] J. Emsley, *Nature's building blocks - An A-Z guide to the elements*, Oxford University Press, 2003.

[13] W. Weingarten, *Physica C* **339**, 231 (2000).

[14] J. D. Jackson, *Classical Electrodynamics*, Wiley, New York, 1998.

[15] W. Buckel and R. Kleiner, *Supraleitung*, Wiley-Vch, 2004.

[16] H. Padamsee, T. Hays, and J. Knobloch, *RF superconductivity for accelerators*, Wiley, Weinheim, 2. edition, 2008.

[17] T. Khabiboulline, C. Cooper, N. Dhanaraj, H. Edwards, M. Foley, E. Harms, D. Mitchell, A. Rowe, N. Solyak, and W.-D. Moeller, 3.9 GHz superconducting accelerating 9-cell cavity vertical test results, in *Proceedings of PAC07, Albuquerque, New Mexico, USA*.

[18] Y. Bruynseraede, D. Gorle, D. Leroy, and P. Morignot, *Physica* **54**, 137 (1971).

[19] J. Guo, S. Tantawi, C. Yoneda, and D. Martin, An X-band Testing System for Novel Superconducting RF Materials, in *Proceedings of the 15h International Workshop on RF Superconductivity, Chicago, USA*, 2011.

[20] B. Aune, R. Bandelmann, D. Bloess, B. Bonin, A. Bosotti, M. Champion, C. Crawford, G. Deppe, B. Dwersteg, D. A. Edwards, H. T. Edwards, M. Ferrario, M. Fouaidy, P.-D. Gall, A. Gamp, A. Gössel, J. Graber, D. Hubert, M. Hüning, M. Juillard, T. Junquera, H. Kaiser, G. Kreps, M. Kuchnir, R. Lange, M. Leenen, M. Liepe, L. Lilje, A. Matheisen, W.-D. Möller, A. Mosnier, H. Padamsee, C. Pagani, M. Pekeler, H.-B. Peters, O. Peters, D. Proch, K. Rehlich, D. Reschke, H. Safa, T. Schilcher, P. Schmüser, J. Sekutowicz, S. Simrock, W. Singer, M. Tigner, D. Trines, K. Twarowski, G. Weichert, J. Weisend, J. Wojtkiewicz, S. Wolff, and K. Zapfe, *Phys. Rev. ST Accel. Beams* **3**, 092001 (2000).

[21] Y. Xie and M. Liepe, TE Sample Host Cavities Development at Cornell, in *Proceedings of the 15h International Workshop on RF Superconductivity, Chicago, USA*, 2011.

[22] S. Posen, M. Liepe, and Y. Xie, Cornell SRF new materials program, in *Proceedings of the 2nd International Particle Acclerator Conference, San Sebastian, Spain*, 2011.

[23] M. Fouaidy, P. Bosland, S. Chel, M. Juillard, and M. Ribeaudeau, New Results on RF Properties of Superconducting Niobium Films Using a Thermometric System, in *Proceedings of the 8th European Particle Accelerator Conference, Paris, France*, 2002.

[24] S. Chel, M. Juillard, J. P. Charrier, M. Ribeaudeau, M. Caruette, and M. Fouaidy, Surface Resistance Measurements of Superconducting Samples with Vacuum Insulated Thermometers, in *Proceedings of the 5th European Particle Accelerator Conference, Stockholm, Sweden*, 1998.

[25] G. Martinet, S. Blivet, M. Fouaidy, and N. Hammoudi, Development of a TE011 Cavity for Thin-Films Study, in *Proceedings of the 14th International Workshop on RF Superconductivity, Berlin, Germany*, 2009.

[26] B. P. Xiao, C. E. Reece, H. L. Phillips, R. L. Geng, H. Wang, F. Marhauser, and M. J. Kelley, *Review of Scientific Instruments* **82**, 056104 (2011).

[27] B. P. Xiao, H. L. Phillips, C. E. Reece, T. Tajima, and M. J. Kelley, RF surface impedance of MgB2 thin films at 7.5 GHz, in *Proceedings of the 15th International Workshop on RF Superconductivity, Chicago, USA*, 2011.

[28] E. Brigant, E. Haebel, and E. Mahner, The Quadrupole Resonator, Design Considerations and Layout of a New Instrument for the RF Characterization of Superconducting Surface Samples, in *Proceedings of the 6th European Particle Accelerator Conference, Stockholm, Sweden*, 1998.

[29] E. Chiaveri, E. Haebel, E. Mahner, and J. M. Tessier, The Quadrupole Resonator: Construction, RF System Field Calculations and First Applications, in *Proceedings of the 6th European Particle Accelerator Conference, Stockholm, Sweden*, 1998.

[30] E. Mahner, S. Calatroni, E. Chiaveri, E. Haebel, and J. M. Tessier, *Review of Scientific Instruments* **74**, 3390 (2003).

[31] T. Junginger, W. Weingarten, and C. Welsch, RF characterization of superconducting samples, in *Proceedings of the 14th International Workshop on RF Superconductivity, Berlin, Germany*, 2009.

[32] T. Junginger, W. Weingarten, and C. Welsch, Review of RF Sample Test Equipment and Results, in *Proceedings of the 15th International Workshop on RF Superconductivity, Chicago, Ill., USA*, 2011.

[33] T. Junginger, W. Weingarten, C. Welsch, and R. Seviour, RF and surface properties of superconducting samples, in *Proceedings of the 2nd International Particle Accelerator Conference, San Sebastian, Spain*, 2011.

[34] H. Kammerlingh-Onnes, *Comm. Leiden* **140b,c and 141b** (1914).

[35] M. Tinkham, *Introduction to Superconductivity*, Dover Publications, 2004.

[36] B. Visentin, Q-Slope at high gradients: Review of experiments and theories, in *Proceedings of the 11th International Workshop on RF Superconductivity, Lübeck, Germany*, 2003.

[37] P. Bauer, Review of models of RF Surface Resistance in high gradient niobium cavities for particle accelerators revision 1, Technical Report TD-04-014, Fermilab, 2004.

[38] P. B. Wilson and H. A. Schwettman, *IEEE Transactions on Nuclear Science* **12**, 1045 (1965).

[39] H. Padamsee, *Superconductor Science and Technology* **14**, 28 (2001).

[40] R. Geng, G. Eremeev, H. Padamsee, and V. Shemelin, High gradient studies for ILC with singel-cell re-entrant shape and elliptical shape cavities made of fine-grain and large-grain niobium, in *Proceedings of PAC, Albaquerque, New Mexico, USA*, 2007.

[41] T. Yogi, G. J. Dick, and J. E. Mercereau, *Phys. Rev. Lett.* **39**, 827 (1977).

[42] D. Boussard, E. Chiaveri, E. Haebel, H. P. Kindermann, R. Losito, S. Marque, V. Rödel, and M. Stirbet, The LHC superconducting cavities, Technical Report LHC-Project-Report-301, CERN, 1999.

[43] D. Boussard and T. P. R. Linnecar, The LHC Superconducting RF System, Technical Report LHC-Project-Report-316, CERN, 1999.

[44] S. Bauer, W. Diete, B. Griep, M. Peiniger, H. Vogel, P. vom Stein, S. Calatroni, E. Chiaveri, and R. Losito, Production of Nb/Cu sputtered superconducting cavities for LHC, in *Proceedings of the 9th Workshop on RF Superconductivity, Santa Fe, New Mexico, USA*.

[45] J. Halbritter, FORTRAN Program for the computation of the surface impedance of superconductors, Technical report, KFK-Extern 3/70-6, Karlsruhe, 1970.

[46] D. Boussard, Operational experience with the LEP2 SC cavity system, in *Proceedings of the 5th European Particle Accelerator Conference*, 1996.

[47] P. Maesen, The data is available in logbooks at CERN and partly in electronic files. Error estimates are not given in there. On the 1.12.11 P. Maesen, who was responsible at this moment for these measurements gave the error estimate of 10 %.

[48] G. Ciovati, R. Geng, J. Mammosser, and J. W. Saunders, *IEEE Transactions on applied superconductivity* **21**, 1914 (2011).

[49] C. Benvenuti, S. Calatroni, P. Darriulat, M. Peck, A. M. Valente, and C. V. Hof, *Physica C* **351**, 421 (2001).

[50] C. J. Gorter and H. B. G. Casimir, *Z. techn. Physik* **15**, 539 (1934).

[51] F. London and H. London, *Proceedings of the Royal Society of London. Series A, Mathematical and physical sciences.* **149**, 866 (1935).

[52] J. Halbritter, *Zeitschrift für Physik B* **31**, 19 (1978).

[53] J. P. Turneaure, J. Halbritter, and H. A. Schwettman, *Journal of Superconductivity* **4**, 341 (1991).

[54] J. Bardeen, L. N. Cooper, and J. Schrieffer, *Phys. Rev.* **108**, 1157 (1957).

[55] D. C. Mattis and J. Bardeen, *Phys. Rev.* **111**, 412 (1958).

[56] A. Gurevich, *Physica C* **441**, 38 (2006).

[57] J. Halbritter, Residual Losses, High Electric and Magnetic RF Fields in Superconducting Cavities, in *Superconducting Materials for High Energy Colliders - Proceedings of the 38th Workshop of the INFN Eloisatron Project*, 1999.

[58] J. Vines, Y. Xie, and H. Padamsee, Systematic Trends for the Medium Field Q-Slope, in *Proceedings of the 13th International Conference on RF Superconductivity, Beijing, China*, 2007.

[59] P. Bauer, N. Solyak, G. C. nad G. Eremeev, A. Gurevich, L. Lilje, and B. Visentin, *Physica C* **441**, 51 (2006).

[60] V. Palmieri, The problem of Q-Drop in superconducting resonators revised by the analysis of fundamental concepts from RF-superconductivity theory, in *Proceedings of the 12th International Workshop on RF Superconductivity, Cornell University, Ithaca, New York, USA*, 2005.

[61] W. Weingarten, *Phys. Rev. ST Accel. Beams* **14**, 101002 (2011).

[62] C. Benvenuti, S. Calatroni, I. Campisi, P. Darriulat, M. Peck, R. Russo, and A.-M. Valente, *Physica C* **316** (1999).

[63] D. BLOESS, C. DURAND, E. MAHNER, H. NAKAI, and W. WEINGARTEN, *IEEE Transactions on applied superconductivity* **7**, 1776 (1997).

[64] W. Weingarten, A two-fluid model description of the Q-slope and Q-drop as observed in niobium superconducting accelerating cavities, Technical report, CERN-ATS-Note-2011-019 TECH, 2011.

[65] W. Weingarten, On the Field Dependent Surface Resistance observed in Superconducting Niobium Cavities, in *Proceedings of the 14th International Workshop on RF Superconductivity, Berlin, Germany*, 2009.

[66] A. B. Pippard, *Proceedings of the Royal Society of London. Series A, Mathematical and Physical Sciences* **216**, 547 (1953).

[67] J. Halbritter, *Journal of Applied Physics* **97**, 083904 (2005).

[68] J. Halbritter, *Journal of the Less-Common Metals* **139**, 133 (1988).

[69] J. Halbritter, P. Kneisel, V. Palmieri, and M. Pekeler, *IEEE Transactions on Applied Superconductivity* **11**, 1864 (2001).

[70] J. Halbritter, High field Q Drop in superconducting GHz cavities, in *Proceedings of the 14th International Workshop on RF Superconductivity, Berlin, Germany*, 2009.

[71] G. Ciovati, *Physica C* **441**, 44 (2006).

[72] G. Ciovati and P. Kneisel, *Phys. Rev. ST Accel. Beams* **9**, 042001 (2006).

[73] H. Safa, High-field behaviour of scrf cavities, in *Proceedings of the 10th Workshop on RF Superconductivity, Tsukuba, Japan*, 2001.

[74] H. J. Halama, *Particle Accelerators* **2**, 335 (1971).

[75] J. Halbritter, On RF residual losses in superconducting cavities, in *Proceedings of the second SRF Workshop, Geneva, Switzerland*, 1984.

[76] P. Kneisel, G. Muller, and C. Reece, *IEEE Transactions on Magnetics* **23**, 1417 (1987).

[77] C. Vallet, M. Bolоré, B. Bonin, J. P. Charrier, B. Daillant, J. Gratadour, F. Koechlin, and H. Safa, Flux Trapping in Superconducting Cavities, in *Proceedings of the third European Particle Accelerator Conference, Berlin, Germany*, 1992.

[78] S. Aull, O. Kugeler, and J. Knobloch, Study of trapped magnetic flux in superconducting niobium samples, in *Proceedings of the 15th International Workshop on RF Superconductivity, Chicago, Ill., USA*, 2011.

[79] B. Bonin and R. Roeth, *Particle Accelerators* **40**, 59 (1992).

[80] J. Knobloch, *AIP Conference Proceedings* **671**, 133 (2003).

[81] V. L. Pokrovskii, *The Great Soviet Encyclopedia*, The Gale Group, 3. edition, 1979.

[82] C. Bean and J. Livingston, *Phys. Rev. Lett.* **12**, 14 (1965).

[83] A. A. Abrikosov, *Journal of Physics and Chemistry of Solids* **2**, 199 (1957).

[84] P. de Gennes, *Superconductivity of metals and alloys*, Addison-Wesley Publishing Company, fourth printing, 1992.

[85] P. G. de Gennes, *Solid State Communications* **3**, 127 (1965).

[86] V. Ginsburg and L. Landau, *Zh. Eksp. Teor. Fiz.* **20**, 1064 (1950), English Translation in: L. D. Landau, Collected papers (Oxford: Pergamon Press, 1965) p. 546.

[87] J. Matricon and D. Saint-James, *Physics Letters A* **24** (1967).

[88] M. K. Transtrum, G. Catelani, and J. P. Sethna, *Phys. Rev. B* **83** (2011).

[89] G. Eilenberger, *Zeitschrift für Physik* **214**, 195 (1968).

[90] G. Catelani and J. P. Sethna, *Phys. Rev. B* **78**, 224509 (2008).

[91] T. Hays and H. Padamsee, Measuring the RF Critical Field of Pb, Nb, and Nb3Sn, in *Proceedings of the 1997 Workshop on RF Superconductivity, Abano Terme (Padova), Italy*, 1997.

[92] R. Flippen, *Physics Letters* **17**, 193 (1965).

[93] A. Romanenko, *Surface Characterization of NB cavity sections - Understanding the high field Q-Slope*, PhD thesis, Cornell University, 2009.

[94] K. Saito, Critical Field Limitation of the Niobium Superconducting RF Cavity, in *Proceedings of the 10th International Conference on RF Superconductivity, Tsukuba, Japan*, 2001.

[95] K. Saito, Theoretical Critical field in RF Application, in *Proceedings of the 11th International Conference on RF Superconductivity, Hamburg, Germany*, 2003.

[96] D. R. Lide, editor, *CRC Handbook of Chemistry and Physics, 86th Edition*, Taylor and Francis, Boca Raton, FL, 2005.

[97] W. Weingarten, Superconducting cavities, in *Proceedings of the Joint US-CERN-Japan International School on Frontiers of Accelerator Technology, Hayama/Tsukuba, Japan*, 1996.

[98] H. Padamsee, D. Proch, P. Kneisel, and J. Mioduszewski, *IEEE Transactions on Magnetics* **17**, 947 (1981).

[99] G. Eremeev, R. Geng, and A. Palczewski, Probing the fundamental limit of niobium in high radiofrequency fields by dual mode excitation in superconducting radiofrequency cavities, in *Proceedings of the 15th International Workshop on RF Superconductivity, Chicago, Ill., USA*, 2011.

[100] E. Brigant and E. Haebel, Numerical simulations in the design of a quadripular resonator, Technical Note, EDMS 1178982.

[101] H. H. Meinke, F. W. Gundlach, K. Lange, and K. H. Loecherer, *Taschenbuch der Hochfrequenztechnik; 4. Aufl.*, Springer, Berlin, 1986.

[102] Release Version 2011.07 - Nov 30 - 2011; Computer Simulation Technology (CST), Homepage, www.cst.com, accessed: 5.1.12.

[103] Release Version 12.0.0: Ansoft Inc., HFSS, Homepage www.hfss.com, accessed: 5.1.12.

[104] LabView v. 8.6; www.ni.com/labview/, accessed 5.3.2012.

[105] M. Dzenus, K. Iversen, M. Peiniger, and D. Kiehlmann, *Conference Record of the IEEE Particle Accelerator Conference* **4**, 2390 (1991).

[106] C. Reece, J. Benesch, M. Drury, C. Hovater, J. Mammosser, T. Powers, and J. Preble, Performance experience with the CEBAF SRF cavities, in *Proceedings of the 1995 Particle Accelerator Conference*.

[107] Z. A. Conway, D. L. Hartill, H. S. Padamsee, and E. N. Smith, Oscillating superleak transducers for quench detection in superconducting ILC cavities cooled with HE-II, in *Proceedings of LINAC, Victoria, BC, Canada*, 2008.

[108] K. Liao, C. Balle, J. Bremer, T. Junginger, W. Vollenberg, and W. Weingarten, Second sound measurements for SPL cavity diagnostics, in *Proceedings of the 15th International Workshop on RF Superconductivity, Chicago, Ill., USA*, 2011.

[109] K. Liao, Diagnostics Tests and Studie for SPL cavities, First Open Collaboration Meeting on Superconducting Linacs for High Power Proton Beams (SLHiPP-1).

[110] S. A. Dyer, *Survey of Instrumentation and Measurement*, Wiley-IEEE Press, first edition, 2001.

[111] J. Delayen, *Phase and Amplitude Stabilization of Superconducting Resonators*, PhD thesis, California Institute of Technology, Pasadena, California, 1978.

[112] W. Hoefle and D. Valuch, Private Communication: Discussion about possibilities for a different RF feedback system for the Quadrupole Resonator; 11.11.11.

[113] V. Palmieri, F. Stivanello, S. Stark, C. Roncolato, and M. Valentino, Besides the standard niobium bath chemical polishing, in *Proceedings of the 10th Workshop on RF Superconductivity, Tsukuba, Japan*, 2001.

[114] S. Forel, Private Communication.

[115] J.-P. Birabeau and J. Guerin, Patent No 88 09820, Institut National de la Propriete Industrielle, 1993.

[116] L. Landau and E. Lifshitz, *Course of Theoretical Physics Volume 1, Mechanics*, Pergamon Press„ 1976.

[117] J. Müller, *Zeitschrift Hochfrequenztechnik und Elektroakkustik* **54**, 157 (1939).

[118] L. C. Maier and J. C. Slater, *Journal of Applied Physics* **23**, 68 (1952).

[119] C. J. Gorter and H. Casimir, *Physica* **1**, 306 (1934).

[120] T. Junginger and N. Schwerg, Q-Factor of the Quadrupole Resonator with Niobium Sample, Technical Note, EDMS 1153270, 2011.

[121] G. Ciovati, Private communication; The programme v. 1.1was received from the author by email on the 8.3.2009. The newest version modified by B. Xiao is 2.0. It uses the same routines, but allows to fit measurements of penetration depth and surface resistance to one set of parameters.

[122] G. Ciovati, PhD thesis, Old Dominion University, 2005.

[123] K. Levenberg, *Quart. Appl. Math* **2**, 164 (1944).

[124] D. Marquardt, *SIAM J. Appl. Math* **11**, 431 (1963).

[125] W. H. Press, S. A. Teukolsky, W. T. Vetterling, and B. P. Flannery, *Numerical Recipes in C*, Cambridge University Press, 2002.

[126] H. Safa, *Influence of the RRR of Niobium on the RF properties of superconducting cavities in Advances in Cryogenic Engineering, Volume 43*, Birkhäuser, 1998.

[127] A. Phillip and J. Halbritter, *IEEE Transactions on Magnetics* **19**, 999 (1983).

[128] W. Schwarz and J. Halbritter, *Journal of Applied Physics* **48**, 4618 (1977).

[129] MATLAB v.7.8.0.347 www.mathworks.com/, accessed: 5.1.12.

[130] G. Ciovati, G. Myneni, F. Stevie, P. Maheshwari, and D. Griffis, *Phys. Rev. ST Accel. Beams* **13**, 022002 (2010).

[131] H. A. Leupold and H. A. Boorse, *Phys. Rev.* **134**, 1322 (1964).

[132] J. F. D. Silva, E. Burgemeister, and Z. Dokoupil, *Physica* **41**, 409 (1969).

[133] F. J. Anscombe and J. W. Tukey, *Technometrics* **5**, 141 (1963).

[134] C. Benvenuti, P. Bernard, D. Bloess, G. Cavallari, E. Chiaveri, N. Circelli, W. Erdt, E. Haebel, H. Lengeler, P. Uarchand, R. Stierlin, J. Tuckmantel, W. Weingarten, and H. Piel, RF-Superconductivity at CERN, in *Proceedings of the second SRF Workshop Geneva, Switzerland*, 1984.

[135] H. Padamsee, J. Kirchgessner, D. Moffat, R. Noer, D. Rubin, J. Sears, and Q. S. Shu, New Results on RF and DC Field Emission, in *Proceedings of the Fourth Workshop on RF Superconductivity, KEK, Tsukuba, Japan*, 1990.

[136] J. Graber, C. Crawford, J. Kirchgessner, H. Padamsee, D. Rubin, and P. Schmueser, *Nuclear Instruments and Methods in Physics Research Section A: Accelerators, Spectrometers, Detectors and Associated Equipment* **350**, 572 (1994).

[137] J. Halbritter, Private Communication.

[138] A. D'Elia and M. Pasini, Design and characterisation of the power coupler line for HIE-Isolde high-beta cavity, in *Proceedings of the 14th International Workshop on RF Superconductivity, Berlin, Germany*, 2009.

[139] G. Lanza, S. Calatroni, L. M. A. Ferreira, A. Gustafsson, M. Pasini, and P. Trilhe, The HIE-Isolde Superconducting Cavities: Surface Treatment and Niobium Thin Film Coating, in *Proceedings of the 14th International Workshop on RF Superconductivity, Berlin, Germany*, 2009.

[140] A. D'Elia, P. Maesen, I. Mondino, M. Therasse, and W. Venturini, HIE Isolde Q2_6 Measurement Report, Technical Note, EDMS 1203515, 2012.

[141] V. Palmieri, A. Porcellato, R. Preciso, V. Ruzinov, S. Stark, L. Badan, and I. Kulik, *Cryogenics* **34**, 773 (1994).

[142] A. D'Elia, The value of the electric geometry factor has been calculated using Ansoft HFSS, Private communication 26.1.12.

[143] N. R. A. Valles and M. U. Liepe, Exploring the maximum superheating magnetic fields of niobium, in *Proceedings of the 14th International Conference on RF Superconductivity, Berlin, Germany*, 2009.

[144] N. R. A. Valles and M. U. Liepe, Temperature dependence of the superheating field in niobium, arXiv:1002.3182v1, 2010.

[145] Manufacturer website: www.veho-uk.com/, accessed: 5.1.12.

[146] L. van Loyen, D. Elefant, V. Palmieri, W. Venturini, and J. Halbritter, Topography and electrical properties of sputtered niobium films, in *Proceedings of the 1997 Workshop on RF Superconductivity, Abano Terme (Padova), Italy.*

[147] Manufacturer website: www.zeiss.de; accessed: 5.1.12.

[148] J. Knobloch, R. L. Geng, M. Liepe, and H. Padamsee, High-Field Q Slope in Superconducting Cavities Due to Magnetic Field Enhancement at Grain Boundaries, in *Proceedings of the 9th Workshop on RF Superconductivity, Santa Fe, New Mexico, USA,*, 1999.

[149] P. Mix, *Introduction to nondestructive testing: a training guide*, Wiley-IEEE, 2005.

[150] Manufacturer website: www.veeco.com/, accessed: 5.1.12.

[151] R. Seviour and M. Stables, Results of Surface Characterisation and Preparation, Technical report, Dept Physics, Lancaster University, and the Cockcroft Institute, UK NF note 44.

[152] A. Romanenko, Review of high field Q-slope surface measurements, in *Proceedings of the 13th Conference on Radiofrequency Superconductivity, Beijing, China*, 2007.

[153] F. Dinelli, M. R. Castell, D. A. Ritchie, N. J. Mason, G. A. D. Briggs, and O. V. Kolosov, *Philosophical Magazine A* **80**, 2299 (2000).

[154] G. Binnig, C. F. Quate, and C. Gerber, *Phys.Rev. Lett.* **56**, 930 (1986).

[155] Manufacturer website: http://electron.mit.edu/ odie/afm/, accessed: 5.1.12.

[156] Manufacturer website: www.bruker-axs.com/atomic-force-microscopes.html ; accessed: 18.1.12.

[157] T. Chudoba, N. Schwarzer, and F. Richter, *Surface and Coatings Technology* **127**, 9 (2000).

[158] G. S. Brady, H. R. Clauser, and J. a. Vaccari, *Materials Handbook*, Mc Graw-Hill, 15th edition, 2002.

[159] K. Yamanaka, H. Ogisoa, and O. Kolosov, *Applied Physics Letters* **64**, 178 (1994).

[160] A. Briggs and O. Kolosov, *Acoustic Microscopy*, Oxford University Press, 2nd edition, 2009.

[161] Leica EM TIC020; manufacturer wbsite: http://www.leica-microsystems.com/; accessed: 18.1.12.

[162] J. Halbritter, *Applied Physics A - Solids and Surfaces* **43**, 1 (1987).

[163] M. Grundner and J. Halbritter, *Journal of Applied Physics* **51**, 397 (1980).

[164] M. Grundner and J. Halbritter, *Journal of Applied Physics* **51**, 5396 (1980).

[165] http://srdata.nist.gov/xps/; accessed 23.1.12.

[166] P. Unsworth, Supplier: VSW Company, Manchester. The instrument was designed to obtain an energy resolution of the order of 0.27eV. The X-ray source is Al K_α monochromatised with high flux output and a maximum operating power of 600W. The electron multi-detection system is comprised of a VSW HA150 hemispherical analyser used in fixed analyser transmission mode, private communication 24.01.2012.

[167] V. Kouznetsov, K. Macaka, J. M. Schneider, U. Helmersson, and I. Petrov, *Surface and Coatings Technology* **122**, 290 (1999).

[168] A. Gustaffson, S. Calatroni, W. Vollenberg, and R. Seviour, New methods for thin film deposition and first investigations of the use of high temperature superconductors for thin film cavities, in *Proceedings of the first international particle accelerator conference, Kyoto, Japan*, 2010.

[169] E. Somersalo, P. Ylä-Oijala, D. Proch, and R. Nevanlinna, Analysis of multipacting in coaxial lines, in *Proceedings of PAC*, 1995.

[170] J. Tückmantel, One point multipacting levels determined without electron tracking, in *Proceedings of the 4th Workshop on RF Superconductivity, Tsukuba, Japan*, 1989.

[171] Y. min Li, S. An, Z. Liping, Y. S. Cho, and P. Ylä-Oijala, Multipac 2.1 - Multipacting simulation package with 2D FEM field solver for a microsoft windows system, in *Proceedings of EPAC, Genoa, Italy*, 2008.

[172] Computer Simulation Technology (CST), Homepage, www.cst.com, accessed: 5.1.12.

[173] R. H. Fowler and L. Nordheim, *Proceedings of the Royal Society of London, Series A.* **119**, 173 (1928).

[174] P. Bernard, D. Bloess, W. Hartung, C. Hauviller, and W. Weingarten, Superconducting Niobium Sputter Coated Copper Cavities at 1500 MHz, in *Proceedings of the 5th Workshop on RF Superconductivity, Hamburg*, 1991.